SPACE-TIME-FREQUENCY PROCESSING FROM THE ANALYSIS OF BISTATIC SCATTERING FOR SIMPLE UNDERWATER TARGETS

A Thesis
Presented to
The Academic Faculty

by

Shaun D. Anderson

In Partial Fulfillment
of the Requirements for the Degree
Doctor of Philosophy in the
George W. Woodruff School of Mechanical Engineering

Georgia Institute of Technology
December 2012

SPACE-TIME-FREQUENCY PROCESSING FROM THE ANALYSIS OF BISTATIC SCATTERING FOR SIMPLE UNDERWATER TARGETS

Approved by:

Karim G. Sabra, Ph.D., Advisor
George W. Woodruff School of
Mechanical Engineering
Georgia Institute of Technology

Peter H. Rogers, Ph.D.
George W. Woodruff School of
Mechanical Engineering
Georgia Institute of Technology

F. Levent Degertekin, Ph.D.
George W. Woodruff School of
Mechanical Engineering
Georgia Institute of Technology

Lora G. Weiss, Ph.D.
Georgia Tech Research Institute
Georgia Institute of Technology

Aaron D. Lanterman, Ph.D.
School of Electrical and Computer
Engineering
Georgia Institute of Technology

Date Approved: August 2012

To my mother,

Sandra K. Anderson,

In Loving Memory.

ACKNOWLEDGEMENTS

Throughout this research process, I have received help and support from several people. It is with the presentation of this thesis that I would like to express my sincere gratitude to all of them. First, I would like to thank my advisor Dr. Karim Sabra for his guidance, encouragement, and support during my time here at Georgia Tech. Without his help and guidance, none of this would have been accomplished.

I would like to thank my committee members, Dr. F. Levent Degertekin, Dr. Aaron D. Lanterman, Dr. Peter H. Rogers, and Dr. Lora G. Weiss for all of their time and effort to serve on my committee, and for the valuable insights and suggestions for this research.

I would also like to thank my friends for their company and support throughout this process: Akibi Archer, Shane Lani, and Tim Hsu, who kept me sane, were always willing to let me bounce ideas off them, and always willing to lend a helping hand. Finally, I want to express my deepest gratitude to my loved ones, their unconditional support and belief in me made this all possible. I would especially like to thank my wife, Alison, whose love, patience, and support was truly immeasurable in the final stages of the Ph.D. process.

TABLE OF CONTENTS

LIST OF TABLES

LIST OF FIGURES

SUMMARY

The development of low-frequency SONAR systems, using a network of autonomous systems in unmanned vehicles, provides a practical means for bistatic measurements (i.e. when the source and receiver are widely separated, thus allowing multiple viewpoints of a target). Furthermore, time-frequency analysis, in particular Wigner-Ville analysis, takes advantage of the evolution of the time dependent echo spectrum to differentiate a man-made target (e.g. an elastic spherical shell, or cylinder) from a natural one of the similar shape (e.g. a rock). Indeed, key energetic features of man-made objects can aid in identification and classification in the presence of clutter and noise. For example, in a fluid-loaded thin spherical shell, an energetic feature is the mid-frequency enhancement echoes (MFE) that result from antisymmetric Lamb waves propagating around the circumference of the shell, which have been shown to be an acoustic feature useful in this pursuit. This research investigates the enhancement and benefits of bistatic measurements using the Wigner-Ville analysis along with acoustic imaging methods. Additionally, the advantage of joint space-time-frequency coherent processing is investigated for optimal array processing to enhance the detection of non-stationary signals across an array. The proposed methodology is tested using both numerical simulations and experimental data for spherical shells and solid cylinders. This research was conducted as part of the Shallow Water Autonomous Mine Sensing Initiative (SWAMSI) sponsored by ONR.

CHAPTER I

INTRODUCTION

1.1 Introduction

Detecting and classifying man-made objects in shallow water is a challenging problem with high operational importance. Because of their effective propagation in water, acoustical waves have become a major tool in the detection of objects in underwater systems. Some applications include, but are not limited to, mine countermeasures (MCM), pipeline maintenance, buried waste retrieval, as well as underwater archeology [11].

Mine-countermeasure (MCM) advancement has been a priority of the military for decades. Mine technology has continued to develop alongside these counter-measures, and therefore this is a never-ending pursuit [71, 80, 44, 50, 15]. Naval mine countermeasures are performed to counter the effectiveness of underwater mines. The primary motivation for the research presented here is intended to be focused toward target detection intended for future application to the MCM problem. The MCM application will provide the overarching elements (i.e. detection using the structural acoustic regime of frequencies from bistatic data) for this research. The full solution to mine countermeasure problem will not be the goal of the research, rather the goal will be to develop methods and tools useful for simple man-made target detection under the basic MCM elements laid out in this chapter.

1.2 Motivation

The current detection of underwater targets, includes methods that consists of high frequency acoustic imaging from SONAR equipped ships or unmanned vehicles (e.g.

using the Remote Environmental Monitoring Units (REMUS)) of an area for detection [80, 71, 28]. These systems are not always capable of detection and require improvement for certain scenarios, such as, when a object is buried in the sediment, or when the area has a large amount of clutter (i.e. rocks or decoys) that make detection difficult.

During the past decade, systems consisting of multiple Autonomous Underwater Vehicles (AUV) have been developed in order to accomplish the complex mission of identifying and classifying man-made targets in the presence of other objects on the sea bottom. Furthermore, using a network of autonomous unmanned vehicles provides a practical means for bistatic measurements (i.e. when the source and receiver are widely separated). These bistatic measurements allow for multiple viewpoints of the target of interest. Such systems can potentially yield bistatic enhancement for detection and classification capabilities when compared to traditional monostatic systems [50, 61].

The Office of Naval Research (ONR) recently sponsored a research project to aid the development of a multi-Autonomous Underwater Vehicle (AUV) framework for mine-countermeasure activities, which has been designated as the Shallow Water Autonomous Mine Sensing Initiative (SWAMSI). The SWAMSI program was developed to collect at-sea data using multiple AUVs and provide a proof of concept for the improvement of concurrent detection and classification. The multistatic (source and receivers are located separately) field characteristics obtained from SWAMSI, rather than classical SONAR imaging (monostatic - source and receiver co-located), can then be used as a foundation for enhancing concurrent detection and classification. The SWAMSI main objective was the achievement of robust multi-static detection and classification of proud (lying on the ocean bottom) and buried seabed objects using cooperative networks of autonomous vehicles equipped with acoustic sources and receiving arrays.

1.3 Detection Problem

Mine technology has become increasingly more complex through the years (i.e. including complex shapes such as composite truncated cones), though there are design features that are not likely to change in the near future. Mines have to not only hold explosives, but also are required to be stable during transportation and deployment at depth in the ocean. These requirements usually lead to the use of a thin shell design, typically made from a steel alloy or polymer. The thin shell is an optimal solution to the design criteria of stability, cost, and capacity, thus this was selected to be the focus for developing a detection scheme for determining acoustic features of targets.

Extensive work has been completed on the underwater target detection in shallow water problem to improve capability. This has included development of broadband high resolution (high frequency $>$ 70 kHz) imaging systems for target detection; however, there remains a need for improvement for detection and classification of the buried objects on the ocean floor. Some proposed methods include low frequency SONAR, dual frequency SONAR (high and low frequency), and magnetic detection systems [15, 80, 43].

In the context of low-mid frequency active SONAR (structural acoustics regime $<$ 70 kHz), a key interest in target detection is the ability to identify acoustic echoes of man-made targets, such as elastic shells, from ocean reverberation due to volume scattering and ambient noise especially in the presence of multipath [50]. The analysis of acoustic scattering by elastic shells, such as spheres is a topic that has been receiving attention for the last several decades [25, 65, 91, 55]. In particular, time-frequency analysis has been shown to be a relevant tool for the acoustic detection and classification of elastic shells and propagation in dispersive media [24, 105, 102].

Additionally the use of multiple AUV's allows bistatic or multistatic data collection, but also presents challenges in operation and signal processing due to the

collection of multiple viewpoints on different systems. A monostatic configuration is a traditional approach for SONAR and imaging systems; However, additional information may be obtained using bistatic views of targets from the various AUV's where the receiver location differs from the source. The literature and tools for ***low-mid frequency bistatic processing*** of scattered data is sparse and deserves further attention. Focusing on the low-mid frequency regime allows the excitation of the structural acoustics and allows the response to propagate with lower attenuation.

The scattered field of a man-made target (e.g. an elastic shell) can be simplified and separated into a specular contribution and a structural or elastic response (e.g. due to the target's resonances) [24, 52, 73]. The specular contribution is simply the direct geometrical reflection from an object, which depends on the reflectivity and shape of the object; whereas the elastic response is dependent on both the object's structure, shape, and material properties. Therefore, the elastic response portion of the scattered field contains additional information about an object, which can be useful in detection and classification. However, this elastic response often has a lower amplitude than the specular echo and requires additional processing for detection.

One of the important issues regarding the physics of the scattering from elastic shells is the isolation and the analysis of the energetic acoustic features of the target. In target detection and classification, resonance of man-made elastic targets is a key concept that differentiates them from rocks or other clutter that may have similar shapes. In addition, it has been established that at lower frequencies, man-made targets, such as elastic shells, support the excitation and radiation of strong structural waves and resonances that create a specific acoustic signature that distinguishes them from other objects, and can be used for recognition of certain types of targets. Most of the previous work in this area has addressed the far-field monostatic scattering problem, though this research will present methods that could make full use of AUV's, which could possibly make better use of the bistatic target response.

1.4 Approach

For target detection and classification systems, development of a signal processing methods require detailed knowledge of the physical behavior of the acoustic energy insonifying an elastic object. The analysis of the target acoustic scattering response is of crucial importance to identify a set of relevant parameters that due to their direct relationship to the physical properties best represent the fundamental characteristics of a target.

This dissertation sets out to present and analyze tools for improving detection of elastic targets using low-mid frequency monostatic and bistatic data, especially in the presence of guided or elastic waves that appear in the structural acoustics regime of frequencies [86, 40, 52]. Consequently, in order to implement optimum receiver and signal processing algorithms for such bistatic SONAR systems, it is then fruitful to further understand the spatial and temporal variations of the bistatic acoustic scattering responses of elastic shells.

Furthermore, this research will focus on low-mid frequency SONAR for detection and classification as opposed to common detection techniques that use higher frequency SONAR for sea-floor imaging. Under this research, the goal will ultimately be to develop processing tools to improve the use of bistatic data to enhance detection of man-made targets. Specifically, the use of space-time-frequency methods will be implemented in order to enhance detection of the elastic contribution to the measured scattered field from an object. Time-frequency analysis allows further understanding of the time and frequency evolution of a signal in the bistatic regime; similarly, the additional information available via the time-frequency analysis provides a means to combine signals coherently from a given source in an optimal fashion.

1.5 Background

This section will briefly introduce some necessary background knowledge and highlight the scope of this research. Additional background information will be presented in the subsequent chapters where it will be more relevant.

One of the first requirements of any detection system is to find a robust feature or phenomenon that is unique to the target of interest. For underwater target detection, this requires a robust acoustic scattering feature that will allow a system to distinguish between targets of interest (elastic shells in this case) and clutter. The system can then leverage signal-processing methods (i.e. array processing, acoustic imaging) to enhance the detection capabilities of an identifying feature. This section will justify the use of SONAR operating at the structural acoustic regime of frequencies to excite elastic response (e.g. guided waves circumnavigating the shell) of targets with simple canonical shapes (i.e. sphere, cylinder).

1.5.1 Frequency Selection

Traditional detection systems operate at high frequencies (i.e. when the acoustic wavelength is much smaller than the target dimensions) for high resolution acoustic imaging. However, if a target were to be buried or covered in sediment these higher frequencies do not allow sound to effectively penetrate into the ocean bottom. The use of the lower structural acoustic regime of frequencies or low to mid frequency regime, approximated in literature at f $<$ 80 ka (normalized frequency unit, where k is the wavenumber and a is the fundamental dimension of the object) has been an emerging trend for detection and classification scenarios [54, 80, 60, 50]. This trend is due to the low frequency SONAR having better ability to penetrate the ocean floor through evanescent coupling, as shown in Fig. 1.1, as well as having lower attenuation.

The critical angle for propagation at an interface can be found as $\theta_c = sin^{-1}(\rho_2 c_2/\rho_1 c_1)$ (where ρ and c are the medium density and sound speed of the water (1) and sediment

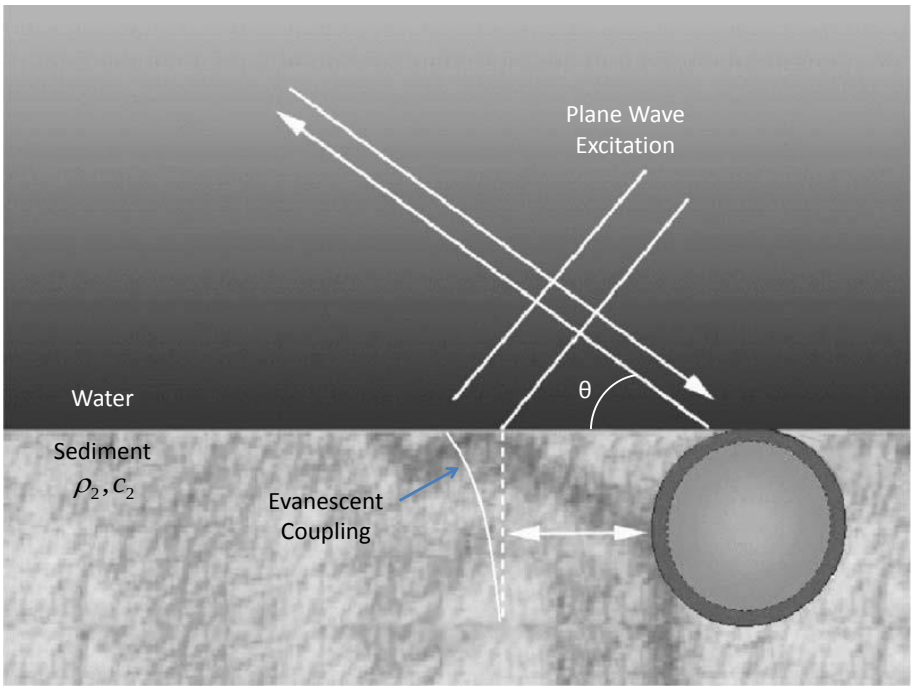

Figure 1.1: Low-frequency representation of subcritical scattering and evanescent coupling for a buried shell. Image adapted from Fig. 3 in Lucifredi et al. [52].

(2) respectively). For large standoff distances, the low frequency acoustic energy is able to penetrate the bottom for subcritical scattering angles, which is necessary to detect a buried object at a reasonable standoff distance. The acoustic penetration into the ocean bottom typically requires a powerful and directional source to accomplish this subcritical insonification of the sediment [76, 52, 43].

Furthermore, previous literature has shown the detection performance for buried objects increases when angles and frequencies below the shallow water environment critical angle are used in the presence of a rippled seabed [76]. Low-mid frequency systems additionally allow for greater standoff distance for sound propagation in shallow water due to attenuation and environmental propagation effects, which can be beneficial for large coverage areas, since the SONAR system would not be required to be directly on top of an object for detection. In this low frequency regime, one can excite guided waves which couple to the elastic structure of man-made objects and radiate into the surrounding medium. As previously mentioned, these guided waves

are of particular interest as they are typically apparent only in man-made objects and can be used for detection and classification as will be further discussed in Chapter II.

1.5.2 Bistatic Detection

The acoustic scattered field from a target is a function of the structure, shape, and material as well as other propagation and environmental factors [58]. For reliable detection and classification, a robust and unique acoustic target feature should be used (in some cases this may be the specular reflection). In particular to bistatic detection, these features should also exist when measured in a bistatic source-receiver configuration. These robust features can be used by classifier software, which is used to determine the identity of a specific target [101].

Recent studies have demonstrated the benefit of bistatic measurements for target detection applications [50, 61]. These bistatic measurements allow for collection of multiple viewpoints of the target, which can potentially enhance the detection and classification capabilities of SONAR systems when compared to traditional monostatic systems. These recent studies have primarily been presented as a method to collect additional specular viewpoints from around a target [61, 50].

One approach for target detection is to use the monostatic ($\theta = 180^{\circ}$) specular echo and diffuse bottom scattering, which can be processed to form an acoustic image. These images can be processed to locate targets shaped like mines, or those casting an acoustic shadow that is expected of a mine shaped object. A pitfall of this type of processing is that the image relies on the specular reflections from a target, and diffuse scattering from the bottom to return in the direction of the source. Certain stealthy objects, such as mines have considered this and reduced the amount of specular scattering that occurs with acoustic coatings and shapes such as truncated cones or cylinders (see depiction of specular reflection in Fig. 1.2) [71]. One difference of this dissertation research will be to make use of bistatic data to enhance the imaging of

the elastic response from a spherical shell. Another proposed improvement would be to use a larger portion of the scattered field beyond the monostatic view by placing a receiver in the bistatic field, which would allow the strongest scattered sound within the bistatic regime to be collected [50, 7]. This could be accomplished by having an AUV circle an object of interest to collect all source-receiver aspects of the target.

Detection of even simple objects, such as a cylinder, can be improved by the bistatic measurement of the scattered field. The shape and response from a cylinder by monostatic detection schemes alone are not able to collect the entire shape of the object effectively since only the edges of the cylinder are able to scatter energy in the monostatic direction ($\theta_s = \theta_r$ labeled on Fig. 1.2). The monostatic response from a cylinder additionally does not allow for a complete image of the object to be formed without further processing of multiple monostatic viewpoints. However, bistatic data from the cylinder could allow for more information about the shape of the object from the specular reflections collected along bistatic receiver positions as depicted in Fig. 1.2.

Current detection processes could be improved using the specular portion of the scattered field to determine the shape of the object based on the shape of the monostatic or bistatic scattering amplitude of a target. The collection of data from circular paths of the source and receiver at different angles θ_s and θ_r respectively could allow for the amplitude of the direct scattered field and scattered field radiation pattern to be obtained [100]. The pattern of the specular echo from a target may not be unique enough to allow identification of similarly shaped targets. The elastic contribution of a target will have a different angular dependence than the specular reflection simply due to the physical mechanisms of the guided wave and radiation of energy from a target as will be discussed in Chapter III. This method is complicated by the frequency dependence of the scattered field pattern. Moreover, a directional receiver can be scanned across different angles where the target reflection is expected to be

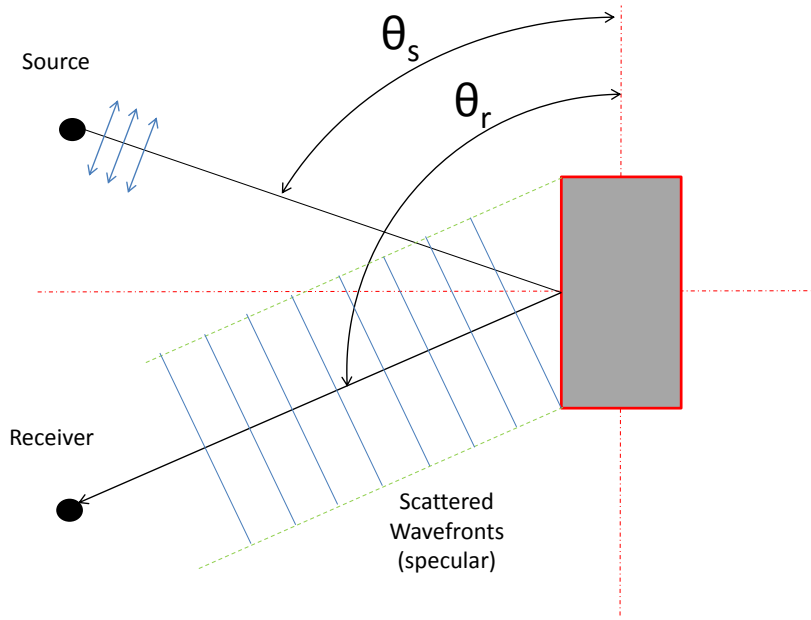

Figure 1.2: Schematic of bistatic specular scattering from a cylinder. This figure depicts a plane wave source angle (θ_s) resulting in the scattered field which primarily reflects at an angle (here as the receiver angle (θ_r)), located away from the source location.

highest, which typically requires the use of a bistatic system as the monostatic system will not necessarily have the highest return [75, 52].

1.5.3 Simple Elastic Targets

Another approach to this bistatic detection problem is to use the elastic response of the scattered field from an object, which will also be a contribution of this research. Effective use of the elastic response of the scattered field requires the scattering behavior to be well understood in order to coherently combine and process various viewpoints of a target. For this purpose, an in depth study of the elastic behavior in a bistatic configuration from a simple elastic target is beneficial.

Scattering of an acoustic plane wave from an elastic spherical shell has been considered a standard problem, for which analytical solutions have been extensively studied

both theoretically and experimentally [55, 62, 85, 90]. These standard problems are important for the evaluation of approximate numerical models and can contribute to the understanding of the physics and behavior of acoustic interaction with the elastic target. This canonical target shape was selected as the basis for developing the methods presented in this dissertation as its acoustic scattered field and echo generation mechanism is well understood.

The main motivation of previous studies was to develop a precise description of the mechanisms of echo formation, in order to accurately describe the physical features of acoustic scattering. In particular, a separate and unique goal of this dissertation is to identify low-mid frequency acoustic features unique to elastic shells (i.e. man-made objects) and how these acoustic features change with a particular source-target-receiver geometry in order to ultimately use these features for classification purposes.

Understanding of the acoustic response can be simplified by separating the scattered field of an elastic object into two types of waves, the specular and guided waves, which have distinctly different behavior (i.e. rigid body and elastic response). In the low to mid frequency acoustic regime (< 80 ka), a fluid-loaded thin spherical shell produces the specular or direct reflection similar to any acoustically reflective object of comparable shape, as well as, guided waves or Lamb waves circumnavigating the shell, as shown schematically in Fig. 1.3. The canonical model presented here, assumes a plane-wave broadband pulse is incident from the left on a thin spherical shell immersed in water. The ray diagram, shown in Fig. 1.3, of the simplified scattered field is displayed for the specular reflection (dash dot line), and surface guided waves (dashed line) circumnavigating the shell. The surface guided wave couples into the shell's wall at angle α, measured from the normal direction to the shell's wall, and radiates out towards a receiver, located at a distance r and azimuth angle θ, at the same angle α. For simplicity, only the counter-clockwise path around the shell is illustrated in Fig. 1.3, but note that similar clockwise paths also propagate around

the shell. The guided waves excited in the scattered field are a result of the elastic material and thin shell structure of the sphere. These waves are robust, but often are of a low amplitude when measured away from the backscatter region.

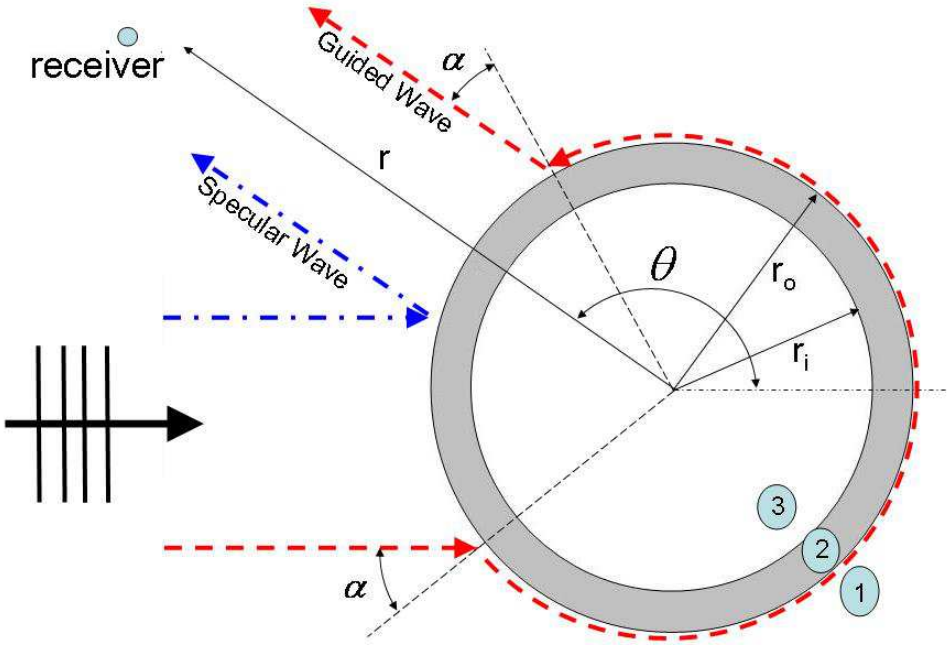

Figure 1.3: Schematic and ray diagram for the simplified acoustic scattering problem under consideration. Depicting a simplified ray path for the specular and guided waves.

Consequently, bistatic detection of these guided waves would need to be enhanced, for instance by combining the signals measured on an array of receivers using array beamforming techniques. But, the design of an optimal beamformer for detection applications should then be determined by the specific time-frequency coherence of the bistatic echoes in order to allow optimal coherent addition of these echoes across a bistatic aperture [89]. The main goal of Chapter III is to investigate theoretically and numerically the bistatic variations of the MFE for a fluid-loaded, thin spherical shell and propose a method for processing data with the behavior.

1.5.4 Acoustic Imaging

Synthetic aperture SONAR (SAS) imaging is one acoustic imaging method used in detection applications [61, 43, 58, 27]. The principle of SAS is to combine successive pings coherently along known positions in order to increase length of the array without requiring a physically larger array. SAS has the potential to produce high resolution images down to millimeter resolution from hundreds of meters away in the ocean and thus is a suitable technique for imaging of the ocean bottom for detection applications. SAS has a very close resemblance with synthetic aperture RADAR (SAR). While SAS technology is maturing fast, it is still relatively new compared to SAR and has key differences in implementation due to the fundamental differences in frequencies and propagation speed.

SAS operated at high frequency is a proven method of detecting objects, and is a current technology used by the Navy for shallow water target detection; however, it may result in false alarms, due to the lack of ability to classify targets from clutter of similar shape such as rocks or decoys[84, 28]. One example of the limitation is shown in Fig. 1.4b, in which there is a sphere and a mine-like object side-by-side in the high frequency (120-180 kHz) SAS image. From this picture and information alone, it is difficult to distinguish a rock from a mine of comparable geometry. These objects cast an acoustic shadow behind them due to the object blocking the acoustic wave from scattering off the ocean bottom directly behind them (see Fig. 1.4a). The shadows cast by the objects can be extremely useful in the detection and classification allowing the system to better determine an object's shape and height. However, if a target is buried, an acoustic shadow no longer exists, and this shadow classification method becomes obsolete for the purposes of detection. Additionally, the elastic waves excited from low-frequency SONAR can fill this shadow region and sometimes may appear as secondary targets behind a target true location in an image.

Typical acoustic imaging uses the specular reflection and diffuse bottom scattering

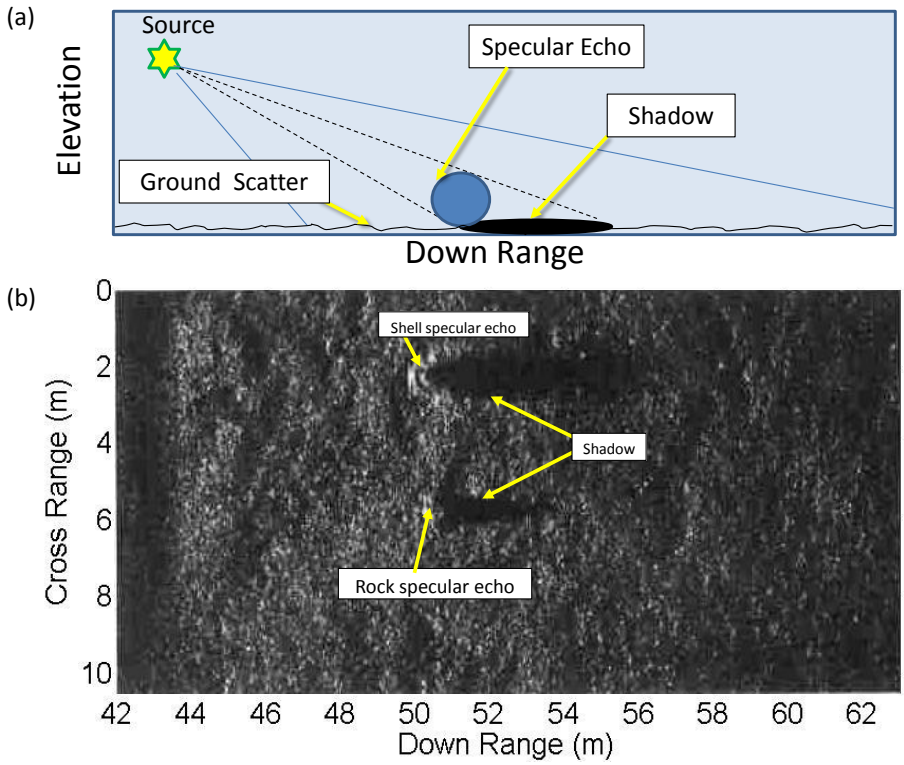

Figure 1.4: Schematic (a) and Example (b) of acoustic imaging, where the image is formed from ground scatter, specular echo from a target, and an acoustic shadow. The example here is of a High frequency SAS system of a 1 m spherical shell, and a mine like object. The acoustic data was taken on a fixed rail SONAR platform using a signal of the frequency band 120-180 kHz. Image reproduced from Sutton et al. [84].

from an array in order to form an image of the ocean bottom [60]. This imaging process will be presented in detail in Chapter IV. One complication to imaging occurs with the presence of the elastic contribution from a target, due to the delayed arrival and coupling with the target structure. The elastic response can skew the image of the target or appear as a separate target using standard SAS methods. It is possible to isolate the specular reflection to eliminate this effect; however, the information of the elastic portion of the scattered field will then be lost. As mentioned previously the elastic contribution could add information in the SAS image and may be used to help discriminate between a man-made object and a simple rock (with no characteristic elastic return).

This research will propose a method to modify the SAS processing for leveraging these elastic contributions for imaging and detection. This phenomenon will be presented and discussed in detail in Chapter V.

1.6 Research Objectives and Overview

The objective of this research is to improve and propose methods available for the detection and classification of a man-made target by means of time-frequency analysis and bistatic enhancement. The goal of the tools developed in this dissertation can be expressed in two words: "detection" and "classification." The proposed methodology was tested by means of numerical simulations and experimental data (conducted in the pond at the Naval Surface Warfare Center in Panama City, Florida). The complete solution to the overarching MCM buried object detection and classification reaches well beyond the scope of this research, and therefore the contributions of the research may be broken down into four main objectives:

1. Investigate and show bistatic variations in time-frequency representation of the acoustic response from elastic spherical shell.

2. Implement an acoustic imaging algorithm that simply takes into account the delayed elastic echoes compared to the specular echo for elastic shells.

3. Apply the proposed methodology to an experimental data set collected in a controlled environment: the pond at Naval Surface Warfare Center Panama City (NSWCPC).

4. Develop Coherent Space-Time-Frequency array processing method to enhance detection of non-stationary signals.

1.7 Organization

The dissertation has been separated into six chapters based on the various research objectives. Chapter II reviews the numerical modeling techniques and the behavior and description of the scattered field of the spherical elastic shell. Additionally this chapter introduces methods used for the analysis and presents results from a parameter study of the spherical shell to highlight the important elastic feature useful for classification. Chapter III goes on to introduce and discuss the bistatic behavior of the elastic target response, and the time-frequency beamforming approach to adjust for the behavior. Chapter IV takes the approach to apply back-propagation methods and a SAS imaging algorithm to the simple targets, and presents the limitations. Then a modification to the SAS method is proposed for handling the elastic contributions in the structural acoustics regime. The SAS algorithms are then applied to the NSWC-PC pond experiment for spherical shell and solid cylinder targets. Chapter V introduces some noise reduction techniques of non-stationary signals across an array and proposes a new Space-Time-Frequency approach to reduce noise for such a problem. Chapter VI concludes the dissertation with a summary of the work and contributions as well as suggested future work.

CHAPTER II

ACOUSTIC SCATTERING FROM SPHERICAL SHELLS: MODELING AND ANALYSIS METHODS

2.1 Motivation and Background

One of the goals of this research is to gain knowledge of the complexities and challenges associated with detecting targets in a shallow water environment. Once these challenges are understood and defined, the subsequent chapters will propose and investigate methods to enhance the detection capability of the targets. The process taken in this endeavor is first to understand the scattered field from a man-made object of interest, and study robust features that may be useful for detection as well as classification. This includes implementing and utilizing a MatLab code developed by Manell E. Zakharia's research group using the canonical model of a spherical shell in order to determine a strategy for acoustic detection. Even in seemingly simple axisymmetric objects, the detection process is full of caveats, which quickly make the problem complex. This chapter presents the tools used for modeling and analyzing a spherical shell, studies in depth the mid-frequency energetic feature of a spherical shell. The purpose of this chapter is to introduce, review, and investigate previous work dealing with acoustic waves scattered by an elastic spherical shell. This review will lay the groundwork for the methods and serve to study the mechanisms for detection of these waves.

The problem of sound scattering by an air-filled elastic spherical shell was first considered by Junger [45], who used the theory of thin shells to describe shell motion as a rigid body scatter plus the "radiation scattering" found from the forced vibrations on a plane wave excitation. Later, it was demonstrated that this theory did not

completely describe the flexural vibrations of a shell [47]. A full solution of the problem for scattering by a fluid loaded shell was proposed by Goodman and Stern [31] and based on the exact theory of elasticity and matched boundary conditions. Goodman and Stern's work placed a fluid filled shell in an ideal fluid, and simplified the model to approximate several special cases. This dissertation uses the generalized results presented by Goodman and Stern [31], which are true not only for thin shells but also for an elastic spherical layer of arbitrary thickness.

This chapter is divided into four remaining sections. Section 2.2 presents the theoretical model used for computing the acoustic scattering from spherical shell. This section will then present a discussion of the low-mid frequency response from the spherical shell. Section 2.3 will present the time-frequency methods and discuss the Wigner-Ville distribution used to analyze the elastic scattering of the target. Section 2.4 then reviews and investigates the robust nature of the elastic response from the spherical shell with a parameter study to fully explore the proposed energetic feature for possible detection and classification. The final section contains a summary and discussion of the elastic spherical shell target response of interest for this research.

2.2 Scattering from an Elastic Spherical Shell: Theory and Numerical Modeling in Free Space

The canonical model presented here, assumes a plane-wave broadband pulse is incident from the left on a thin spherical shell immersed in water. The ray diagram, shown in Fig. 1.3, of the simplified scattered field is displayed for the specular reflection, and surface guided waves circumnavigating the shell.

The basic physical principles that are involved in the formulation of the scattered field from a spherical shell are similar to those found when investigating a fluid loaded plate. In such an instance, there are a combination of flexural and compressional waves formed, which can be separated into antisymmetric and symmetric modes. The zero order antisymmetric mode (A_0) and symmetric mode (S_0) exist over the entire

frequency range and typically carry more energy than higher order modes. These two types of modes in a plate are depicted in Fig. 2.1. Where the figure indicates the in plane and out of plane motion of the symmetric and antisymmetric waves, as well as in the thickness view, the nomenclature of the wave types becomes evident. The solutions for these modes are well understood and the vibration behavior of a flat plate can be calculated using the Rayleigh-Lamb equations [2].

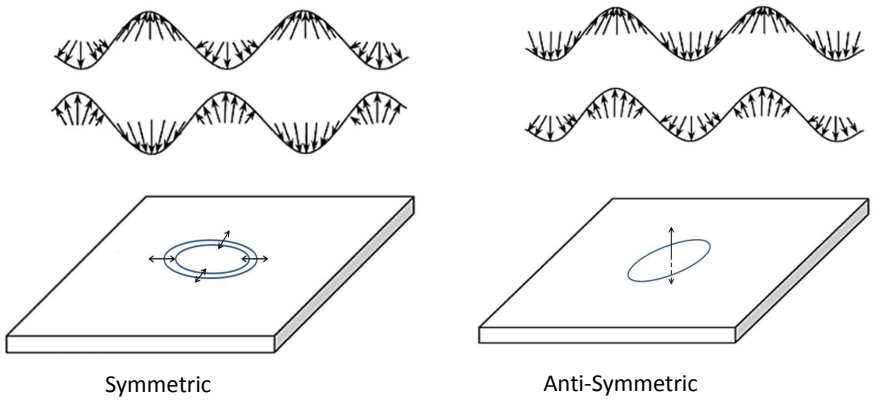

Figure 2.1: Illustration of the Symmetric and Anti-symmetric wave modes that occur in a fluid loaded plate. The plate compression and expansion at each surface is shown by arrows.

In particular, the interaction of the flexural and compressional waves can create a phenomenon called a leaky Lamb mode, which radiates energy from the plate into the surrounding fluid medium. This mode is of particular interest for target detection purposes, due to the energy being 'leaked' into the outer fluid medium. Additionally this physical behavior can now be extended to a thin shell in which the plate is simply wrapped into a curved surface. Thus the behavior is no longer the true definition of

a Lamb mode (since it is no longer occurring on an infinite flat plate), and is why the literature sometimes refers to these waves as Lamb-type modes.

Consequently, from the formation of these waves, a key energetic feature of spherical shells is the mid-frequency enhancement (MFE) echo - also called the coincidence pattern - that is created by the combination of first antisymmetric Lamb waves (A_0) propagating clockwise and counterclockwise around the shell.

This MFE yields energetic acoustic echoes radiating in the surrounding fluid and thus provides a unique acoustic signature of fluid loaded spherical shells, as previously demonstrated theoretically and experimentally [55, 85, 106]. For instance, the frequency band over which the MFE occurs is indicative of the shell material, and the temporal spacing between successive circumnavigating Lamb waves allows an estimate of the radius of the spherical shell [87] as well as the shell material properties [53, 103]. Previous time-frequency analysis of the MFE has focused on source-receiver configurations close to monostatic where the MFE is most energetic [46, 48, 53]. But the MFE persists for bistatic configurations and thus still carries information about the physical features of the elastic shell. However, a practical challenge is that the amplitude of the bistatic MFE is significantly reduced when compared to monostatic measurements, which render its detection more difficult in the presence of high clutter or ambient noise levels.

The mid-frequency enhancement is an energetic acoustic feature common to thin spherical shells created by strong coupling of the first anti-symmetric modal wave with the outer fluid. This energetic feature has been shown to be a useful acoustic feature for classification and detection of a spherical shell. Elastic contributions to the scattered field from a target can provide additional information about the structure, size, and material of the object. These elastic contributions can thus be used for detection and classification of underwater targets [73, 85, 86, 51]. The scattered field from the MFE in the bistatic configuration will be addressed in Chapter III.

2.2.1 Theory

The scattered field of a thin fluid-loaded elastic spherical shell is computed in the MatLab code using the classical theoretical formulation of Goodman and Stern [31] as described hereafter. Assuming that an incident harmonic plane wave with amplitude P_0 and frequency ω impinges on a shell in a homogeneous free space medium with sound speed c_0, the harmonic scattered field, $P(r, \theta, t)$, recorded at a receiver distance r and azimuthal angle θ, may be decomposed into a modal expansion. The inclination angle (orthogonal to the azimuth) of the sphere is taken to be equal to zero because it is not of particular concern in this study due to the azimuthal symmetry of the sphere excited by a plane wave. Thus, the response calculations presented may be applied for any selected inclination angle. The general equations and process for this modal expansion will be reviewed here to set a basic understanding for the research to follow. This work summarizes the formula of the Goodman and Stern paper for a spherical shell in free space [31].

In this approach, the displacement $\boldsymbol{u}$ is first expressed in terms of a scalar potential $\boldsymbol{\phi}$ and the vector potential $\boldsymbol{\psi}$: $\boldsymbol{u} = \nabla\phi + \boldsymbol{\nabla} \times \boldsymbol{\psi}$ [2]. Additionally the use of the linearized Euler equation will allow the acoustic pressure to be determined from the velocity via the displacement.

Using the decomposition of the displacement into scalar and vector quantities allows the equation of motion to be easily satisfied by two separate wave equations as follows.

$$(\frac{1}{C_L^2})(\frac{\partial^2\phi}{\partial t^2}) = \nabla^2\phi \tag{1}$$

$$(\frac{1}{C_T^2})(\frac{\partial^2\psi}{\partial t^2}) = -\boldsymbol{\nabla} \times \boldsymbol{\nabla} \times \psi \tag{2}$$

Where $C_L = [(\lambda + 2\mu)/\rho]^{(1/2)}$ and $C_T = (\mu/\rho)^{(1/2)}$ are the longitudinal and transverse wave speeds, respectively, given in terms of density ρ and Lamé's constants λ and μ. The problem can then be broken down further for each medium of interest numbered as shown in Fig. 1.3. To simplify the representation the index, i will indicate each of the three mediums. Now taking the wave-numbers, k to be the angular frequency divided by the respective wave speed results in Eq. (3) and Eq. (4).

$$k_{i,L}^2 \equiv \frac{\omega^2 \rho_i}{\lambda_i + 2\mu_i} \tag{3}$$

$$k_{i,T}^2 \equiv \omega^2 \frac{\rho_i}{\mu_i} \tag{4}$$

Then each equation can be expressed in terms spherical coordinates and assume a harmonic time dependence of $e^{-j\omega t}$. Taking the time derivative, and substituting the wave-numbers results in Eq. (5) and Eq. (6) for the potential functions.

$$(\nabla^2 + k_{i,L}^2)\phi_i = 0 \tag{5}$$

$$\frac{1}{r^2}\frac{\partial}{\partial r}\left(r^2 \frac{\partial \Psi_i}{\partial r}\right) + \frac{1}{r^2}\frac{\partial}{\partial \theta}\left[\frac{1}{\sin\theta}\frac{\partial}{\partial \theta}\sin\theta \Psi_i\right] = -k_{i,T}^2 \Psi_i \tag{6}$$

The modal form of the solutions, Ψ_i and ϕ_i, for these wave equations are the spherical Bessel functions of the first kind j_l, the second kind n_l, and Legendre polynomials P_l that appear when solving partial differential equations in spherical coordinates. Where l is the mode number, and θ is the azimuthal angle on the shell, which is the only angle of consideration in the measurement due to the problem symmetry (see Fig. 1.3):

$$\phi_i = \sum_{l=0}^{\infty} P_l(\cos\theta)[A_l^i j_l(k_{i,L} r) + B_l^i n_l(k_{i,L} r)] \tag{7}$$

$$\Psi_i = \sum_{l=0}^{\infty} \frac{\partial}{\partial \theta} P_l(\cos\theta)[C_l^i j_l(k_{i,T} r) + D_l^i n_l(k_{i,T} r)] \tag{8}$$

Finally, the appropriate boundary conditions must be applied to define the coefficient constants $A_l^i, B_l^i, C_l^i, D_l^i$. The boundary conditions for this problem are matching displacements and normal stresses at the interfaces, and setting tangential stress to be zero in the fluid domain, which allows one to obtain values for these coefficients. In this study, the concern is only with the acoustic response in the outer fluid (i.e. only the pressure field). Hence, the ϕ_1 term is the only one of importance, and therefore only the A_l^1 needs to be computed. This ϕ_1 term can be written as:

$$\phi_1 = \sum_{l=0}^{\infty} P_l(\cos\theta) A_l^1 h_l(k_{1,L} r) \tag{9}$$

Where h_l is the Hankel function (Bessel function of the third kind). The scattered field of a thin fluid-loaded elastic spherical shell can then be computed using the modal expansion of scalar displacement in Eq. 9. Assuming that an incident harmonic plane wave with amplitude P_0 and frequency ω impinges on a shell then the harmonic scattered field $P(r, \theta, t)$ [recorded at a receiver located in polar coordinates at (r, θ) (see Fig. 1.3)] is decomposed into the modal expansion:

$$P(r, \theta, t) = P_0 e^{-i\omega t} \sum_{l=0}^{\infty} i^l (2l+1) A_l^1 h_l^{(1)}(kr) P_l(\cos\theta) \tag{10}$$

Therefore each modal contribution involves the Hankel function of the first kind $h_l^{(1)}(x)$, and Legendre polynomial, $P_l(x)$, and the acoustic wavenumber, $k = \omega/c_0$, in the outer medium. Furthermore, the modal coefficients A_l^1 are determined by the appropriate boundary conditions (i.e. continuity of constraints and displacements) at the interfaces separating the outer (1), shell (2), and inner (3) mediums as numbered in Fig. 1.3. The calculations for the modal coefficients, and a modified version of the MatLab code developed by Manell E. Zakharia's research group can be found in Appendix A and Appendix D. Table 1 lists the selected physical properties for

the numerical simulations which are representative for the elastic shells and surrounding fluid media with no attenuation for a 1.06 m diameter hollow steel shell (thickness=26.5 mm) immersed in water. These physical parameters were selected to be identical to those used by Zhang et al. [106] in order to ease the subsequent analysis and validation of the MFE mechanism. Numerical simulations for a finite number of modes were calculated in the frequency band [100 Hz-90 kHz] and time-series were generated using Fourier synthesis of the harmonic solution given by Eq. (10). Experimental validation of this code and results are presented in Chapter IV, using data collected at the instrumented pond at the Naval Surface Warfare center Panama City Division.

Table 1: Shell Model Parameter Details

Parameter	Shell	Outside	Inside
Material	304 Stainless Steel	Water	Air
Density (ρ)	7570 kg/m^3	1000 kg/m^3	1.29 kg/m^3
Longitudinal Wave Speed (C_L)	5675 m/s	1470 m/s	331 m/s
Transverse Wave Speed (C_T)	3141 m/s	0 m/s	0 m/s

In particular, the modal sum was truncated arbitrarily at a mode index of $l = 100$ based on convergence tests, where the amplitude's contribution of the higher-order modes ($l > 100$) were found not to significantly contribute to the amplitude of the synthesized broadband time-series. Though the numerical simulation was run up to 90 kHz or 200 ka, the convergence criterion for the number of modes was conducted when analyzing the MFE in the lower frequency band 100 Hz-45 kHz. A Hann windowing function was used as a bandpass frequency filter. This bandpass filter limits the energy for the simulation to $<$ 101.9 ka, so the higher frequency content does not significantly affect the frequency region around the MFE. In this frequency band of 100 Hz-45 kHz, a 99.96% correlation coefficient was obtained between the Fourier synthesized waveform using l=800 and l=100 modes. This convergence of the

100 mode inclusion is shown in Fig. 2.2, where below 45 kHz the numerical results have no difference. Additionally the frequency filter is overlaid on top of the frequency response. Hence 100 modes were used for subsequent simulations. Fig. 2.2 shows the result of the simulations which reveal the instabilities at higher frequency and shows that the region of filtered data matches closely in the frequency region of interest 100 Hz-45 kHz.

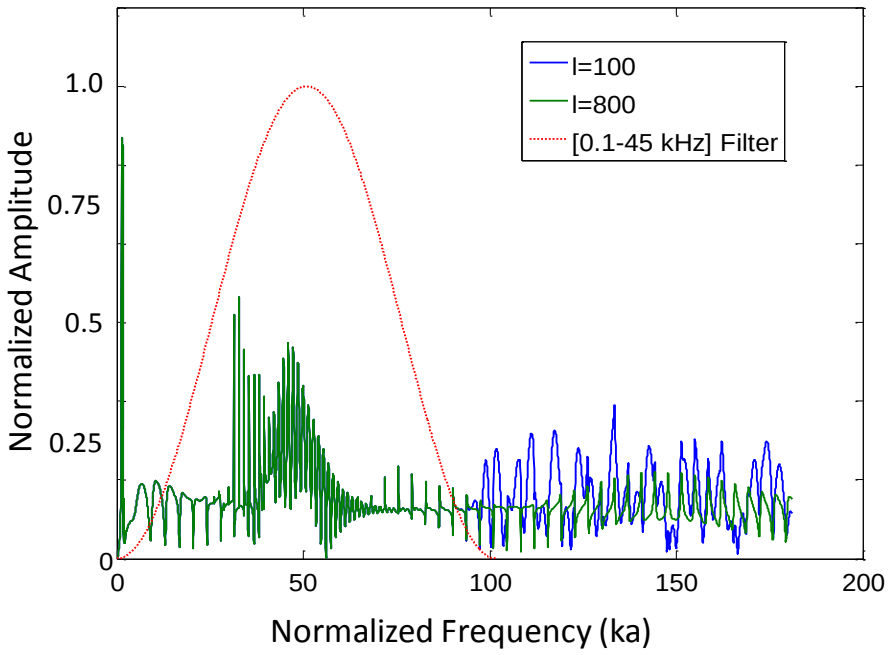

Figure 2.2: Frequency representation of backscatter response from a spherical shell, with overlaid filter and higher mode simulation for comparison and mode convergence test.

2.2.2 Time Domain Analysis of the Scattered Field

Using a partial wave series (see Eq. (10)) formulation to model spherical shell response provides a means for analysis of time-domain far-field scattering pressure. Fig. 2.3 displays the predicted monostatic response of the elastic shell for a receiver located

at an azimuth $\theta = 180°$ and distance r = 10 m using the acoustic model described in the previous section (see Fig. 1.3 and Eq. (10)) and the physical parameters listed in Table 1. The model simulates a Gaussian pulse exciting the sphere in the frequency range of 1 Hz - 50 kHz. A series of narrowband energetic arrivals are clearly visible following the first broadband specular arrival labeled (a) on Fig. 2.3. The following weak arrival, labeled (b) corresponds to the first symmetric mode of the shell S_0. This S_0 arrival will not be the focus of this research due to the presence of the more energetic feature of the MFE for the selected incident pulse shape. The lowest antisymmetric A_0 waves contains two types of propagating waves, classically referred to as A_{0+} and A_{0-} depending whether their energetic contribution is mainly localized within the elastic shell (i.e. shell-borne) or within the surrounding fluid at the shell's surface (i.e. fluid-borne) [55]. These two A_0 waves have different dispersion behavior and bifurcation occurs as a result of this localization of energy [73]. A similar type of wave (i.e. fluid borne waves) exist for a rigid body for the behavior of the A_{0+} below the coincidence frequency; However, these types of waves are purely geometrically diffracted waves and do not contain information about the material. Additionally these waves have fairly strong attenuation, which makes detection difficult[18]. The next energetic arrival, labeled (c), and the ensuing weaker replicas correspond to the lowest antisymmetric mode, A_{0-}, circumnavigating the shell. This first energetic return is characteristic of the MFE occurring due to the A_{0-} mode propagating around the shell after one revolution, see Fig. 1.3 [85, 55]. The increased energy is a result of the interference of the clockwise and counter-clockwise propagation paths for the A_{0-} mode. The quantitative ray model reveals that the amplitude of this pattern results from an optimal balance between the radiation damping parameter, the phase velocity, and the coupling coefficient, which only occurs within a narrow frequency band near the coincidence frequency f_c (giving raise to the MFE phenomenon) [55]. This quantitative ray model approach will be discussed in detail in Chapter III.

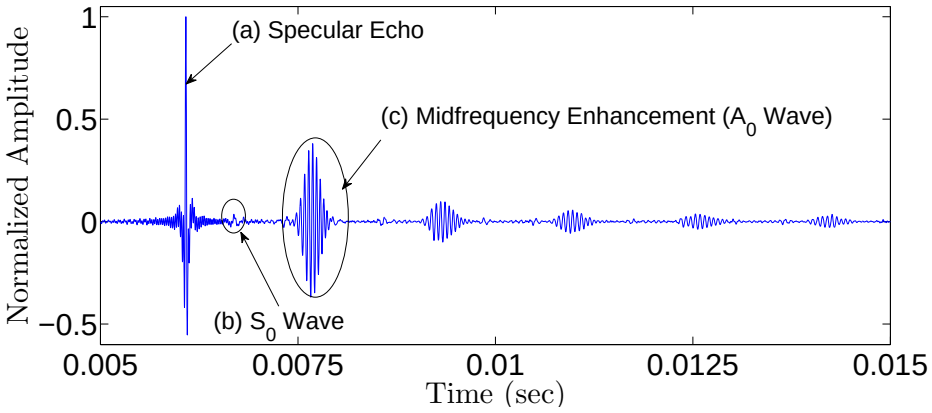

Figure 2.3: Impulse response of the spherical shell in the backscatter direction $\theta = 180°$ (computed from Eq. (10)) using the physical parameters listed in Table 1. The time series is filtered in the frequency band [100 Hz-45 kHz], thus low frequency oscillations are not present. The displayed values were normalized by the maximum value of the specular echo. The three arrows indicate the specular echo, labeled (a), and the echoes of the circumnavigating surface guide waves associated with the first symmetric modes, S_0, labeled (b) and first antisymmetric mode, A_{0^-}, labeled (c), which corresponds to the MFE. Subsequent arrivals correspond to surface guide waves undergoing multiple revolutions around the spherical shell.

Previous studies for monostatic configurations have shown that the frequency content and repetition rate of these A_0 arrivals contain important information about the shell radius and thickness and physical properties such as the compressional and shear wave velocities in the shell as determined from successive arrival times (see Fig. 2.3) [53, 87, 51, 103]. Recently the MFE was studied in a paper by Li [51] for classification purposes in which it was shown that the repetition and frequency of the MFE could be used to estimate the radius and thickness of a shell. Note that the amplitude of the subsequent MFE arrivals are proportionally reduced by the cumulated radiation damping effects after multiple revolutions around the shell. Hence these later arrivals are likely to be even more difficult to detect in the presence of high ambient noise or clutter levels. Consequently, the first and most energetic Lamb-wave echo is the most attractive feature for target's detection or classification purposes.

The examination of the mid-frequency enhancement feature has been extensively studied in articles covering a variety of spherical and cylindrical shells [46, 48, 53, 55, 62, 85, 90, 106]. Both theoretical and experimental analyses of fluid loaded shells were reported. Many papers on this topic can be traced back to the closed form solution model presented by Goodman and Stern. The canonical form of this solution and extensive literature published for a spherical shell makes this shape an obvious choice for theoretical analysis of the MFE using time frequency analysis [31]. Further work was done by Felsen [22] and Ho [38], in which exact and approximate formulations of fully three-dimensional model of the scattered field from a spherical shell surface were presented. Additionally, papers written by Talmant, Zhang, and Marston [55, 85, 106] covered a variety of experiments and ray modeling techniques to better understand the MFE phenomenon with respect to differing types of excitation. These ray techniques will be addressed further in Chapter III, to aid in understanding the bistatic behavior.

Though these articles investigate the formation mechanism of the MFE, none expand on the MFE features measured in a bistatic setup. Instead, previous literature primarily focused on the backscatter (monostatic) direction, which is the most energetic direction for this feature due to the symmetry of the sphere and coherent addition of clockwise and counter-clockwise circumnavigating waves. The bistatic behavior is mentioned briefly in papers by Marston, Sun, and Zhang [55, 56, 82, 106], but no attention is given to the time-frequency content of the MFE. One of the contributions of this research is to quantify the dependence of the time-frequency shifts of the MFE on the bistatic receiver angles and explain the observed time-frequency shifts using a previously derived quantitative ray theory for spherical shell's scattering [107].

2.3 Methods and Mathematical Tools for the Analysis of Scattering of Elastic Targets

2.3.1 Time-Frequency Analysis: Smooth Pseudo Wigner-Ville Transform

As mentioned in the introductory chapter, the main goal of this research is to propose and develop tools to aid in the detection and classification of elastic targets. The approach taken by this research involves the ability to analyze the evolution of frequency content over time. Time-frequency representations have clearly been shown in literature to be useful when analyzing non-stationary signals, which is of use for analyzing the elastic echoes from a spherical shell as will be discussed in the next chapter [80, 24, 14, 16]. Indeed, time-frequency analysis has been shown to be a relevant tool for analyzing the acoustic echoes of elastic shells for MCM purposes [24, 62, 104, 105, 102, 53]. The most general Cohen class of time-frequency analysis in which all time-frequency representations are obtained is defined as follows [16]:

$$CC(t,\omega) = \frac{1}{4\pi^2}\int_{-\infty}^{+\infty}\int_{-\infty}^{+\infty}\int_{-\infty}^{+\infty} s(u+\frac{\tau}{2})s^*(u-\frac{\tau}{2})\phi(\theta,\tau)e^{-j\theta t - j\tau\omega + j\theta u}dud\tau d\theta \quad (11)$$

where t is time, ω is the angular frequency, θ, u are substitution parameters representing frequency and time respectively. $\phi(\theta,\tau)$ is defined as the two dimensional kernel function in which the type and properties of the time-frequency distribution can be defined. The functions $s(u+\frac{\tau}{2})s^*(u-\frac{\tau}{2})$ are the local autocorrelation of the analyzed signal. The traditional and well known Spectrogram can be obtained using a kernel defined as $\int h(u+\frac{\tau}{2})h^*(u-\frac{\tau}{2})e^{-j\theta u}du$. Time-frequency analysis carried out using the Short Time Fourier Transform (STFT), or spectrogram (squared STFT), can be considered a linear method of estimating instantaneous frequency. But the time-frequency resolution of the STFT method is inherently limited by the time-frequency uncertainty principle [78]: higher temporal resolution requires using narrower time-window, which reduces in turn the achievable frequency resolution and vice-versa.

One potential improvement towards higher resolution in both time and frequency is to utilize the higher-order Cohen class of a quadratic time-frequency transform such as the Wigner-Ville transform [16] in which the kernel is defined as $\phi(\theta, \tau) = 1$. This distribution was first introduced by Wigner in the context of quantum mechanics [96], and later independently developed by Ville who applied the same transformation to signal processing and spectral analysis [92]. This kernel results in the Wigner-Ville distribution defined as follows:

$$WV(t, \omega) = \frac{1}{2\pi} \int_{-\infty}^{+\infty} s(t + \frac{\tau}{2}) s^*(t - \frac{\tau}{2}) e^{-j\tau\omega} d\tau \tag{12}$$

Although, the Wigner-Ville transform can provide an optimal localization of broadband and transient signals in the time-frequency plane, it is not readily used in practice as it generates interference patterns between multiple components of the signal, which can complicate the analysis of the results.

Instead, for practical applications, it has been shown that a variant of the Wigner-Ville transform, such as the Smoothed Pseudo Wigner-Ville transformation (SPWV) [16], can be used to smooth these inherent interferences patterns with independent time and frequency smoothing windows. Thus, the SPWV transform can ease the physical identification of multi-component signals in the time-frequency plane while maintaining good instantaneous frequency estimates. More specifically, the kernel for the SPWV distribution is defined by separable kernel functions for time and frequency smoothing windows $h(\tau)$ and $g(u - t)$. The SPWV can then be defined as:

$$SPWV(t, \omega) = \int_{-\infty}^{+\infty} h(\tau) \int_{-\infty}^{+\infty} g(u - t) s(u + \frac{\tau}{2}) s^*(u - \frac{\tau}{2}) \, \mathrm{d}\boldsymbol{u} e^{-j\omega\tau} \, \mathrm{d}\boldsymbol{\tau} \tag{13}$$

where the functions h and g are used to smooth, independently in the time-domain and frequency domain. Hence, contrary to the STFT, the SPWV transform allows one to set the temporal smoothing resolution independently from the frequency

smoothing resolution by selecting appropriately the smoothing functions h and g (e.g. using Hann windows of various lengths) [16]. The result is a better time-frequency localization then STFT without the complications of interference patterns inherent to standard Wigner-Ville transform (see Fig. 2.4). One practical use of the Wigner-Ville transform is the possibility to yield estimates of the group velocity of each specific echo component [104, 105].

However in practice, the optimal time and frequency resolution of the SPWV is limited by the re-apparition of the interference patterns between signal components if the smoothing effect is reduced significantly. Even with the higher order representation, there remains the time and frequency uncertainty limitation when selecting these windows, and higher resolution can lead to artifacts and aliasing of the time-frequency representation. Even with sacrificing resolution to suppress the interference patterns, the SPWV still outperforms the STFT to estimate instantaneous frequency as shown in Fig. 2.4. Here a superposition of two linear chirps is shown for three different time-frequency representations to show the improvement with the SPWV.

A study, which can be found in Appendix B, was conducted to determine the appropriate smoothing windows to suppress the interference patterns and maintain resolution for the MFE. Results of the selected smoothing windows are then applied to the modeled sphere response (see Fig. 2.5), and give a clear picture of the backscattered time-frequency behavior from the spherical shell. Showing the filtered broadband signal arriving first, followed by the more narrowband MFE (at a center frequency of about 20 kHz at 7.1 ms arrival time) and its first circumnavigating replica.

From this representation the center time (t_c) and center frequency (f_c) of the MFE can be measured as the maximum point within this time-frequency atom, labeled in Fig. 2.5.

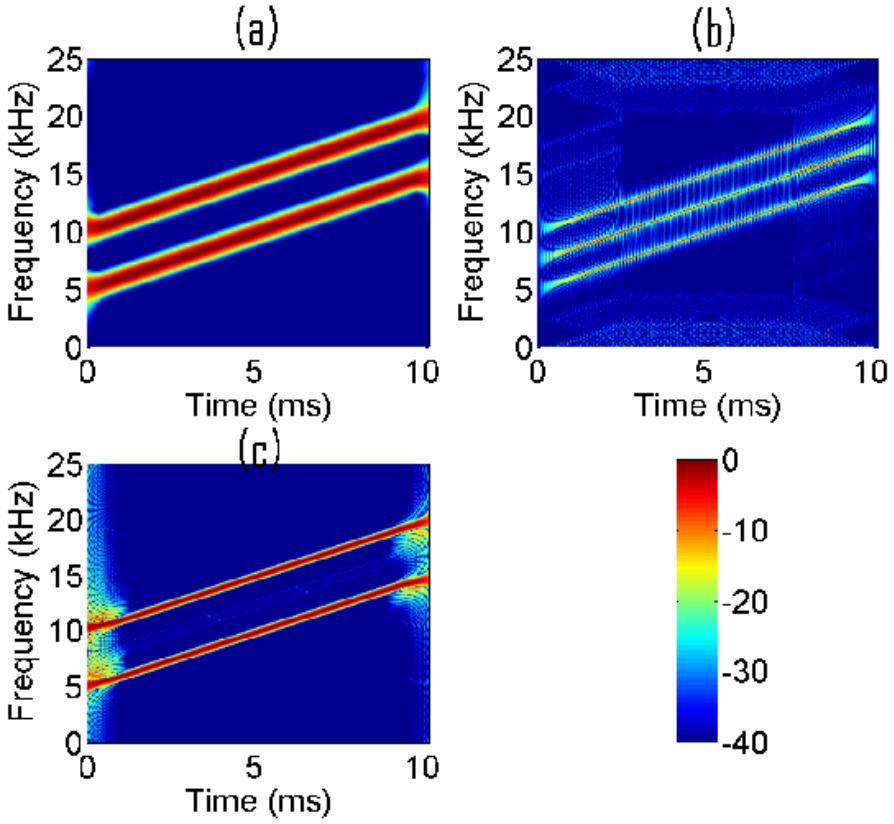

Figure 2.4: Time frequency representations of a signal composed of two linear chirps spanning, respectively, the frequency bands 5-15 kHz and 15-25 kHz: (a) Short Time Fourier Transform, (b) Wigner-Ville distribution showing interference patterns between two signals, and (c) smoothed pseudo Wigner-Ville distribution.

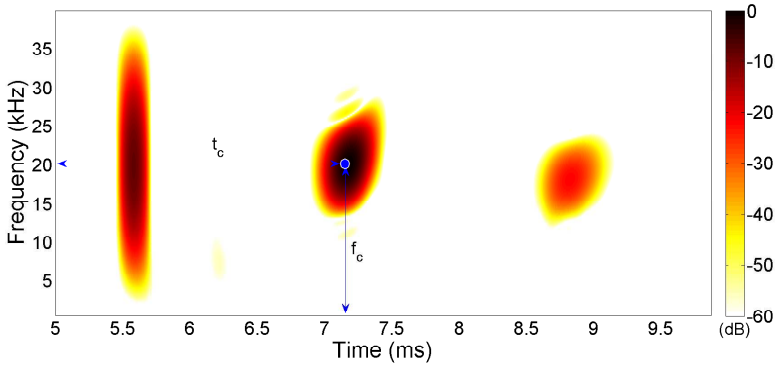

Figure 2.5: SPWV representation of shell response with appropriate smoothing window size based on empirical study. The Hann windows used for smoothing were a time window of 0.2ms (205 points) in length and a frequency smoothing window of 192 Hz (171 points).

2.3.2 Propagation Modeling

Acoustic propagation in the shallow water ocean environment is governed by the wave equation. Standard acoustic techniques enlist the use of the Green's function (fundamental solution to a linear differential equation) to account for the propagation between a source and receiver. The Green's function can be calculated to include the environmental boundary conditions and thus can be thought of as an environmental transfer function. For a majority of the work presented, the free space Green's function, Eq. (14), will be used to reduce the complexity of analysis of the problem. Where r is the distance from source to receiver, t is the time, and c_0 is the sound speed.

$$G(r,t) = \frac{1}{4\pi r}\delta(t - \frac{r}{c_0}) \tag{14}$$

The free-space Green's function is not applicable in the presence of inhomogeneities. Therefore, it cannot be used to model the propagation of acoustic waves in inhomogeneous media; a more complicated Green's function is required.

An analytic form of the Green's function is difficult to obtain for an inhomogeneous medium except for the most trivial cases, e.g., a simple waveguide. Thus, numerical methods and/or simplifying assumptions must be made to obtain a first order solution to gain valuable insight to the behavior of the scattered field near an interface. For comparison to experimental data, where the target is laying on reflective sediment, an acoustic is modeled. This gives a slightly more inclusive Green's function, which is needed to account for the multipath or bottom reflections. As this method is not used in the simulations, but only to confirm experimental arrival times due to multipath (Chap. IV), the details of this type of modeling is discussed further in Appendix C. The full propagation modeling and environmental effects of the MCM problem is complex and requires additional study for both modeling and processing techniques. Further work on this aspect of MCM research can be found in current literature, and

will be left for suggested future work [52, 97].

2.4 Spherical Shell Scattering: Parameter Study

As previously mentioned, in order for an acoustic feature to be useful for detection or classification, the feature needs to be robust to various parameter changes and or environmental conditions. The uniqueness of the high amplitude of the MFE gives immediate interest to using this as a feature to detect man-made objects and be able to distinguish them from natural clutter that occurs on the ocean floor. Fig. 2.5 indicates the center time, t_c, and the center frequency, f_c, of the MFE to be measured for distinct identification useful for classification purposes. Previous literature has mentioned and given results for a few materials of the shell and shown that different types of guided waves exist with a plastic filler and fiberglass shell[88]. However, no complete study or compilation of results exists to show how the Mid Frequency Enhancement changes with various materials parameters, or if it still exists under a variety of conditions.

This section will present various studies that were conducted in order to determine the robust behavior of the MFE with changes of the following parameters: shell thicknesses, shell materials, shell size, surrounding medium, and the inner (filler) material. The baseline shell parameters are for an air-filled steel shell surrounded by water with a thickness ratio of 0.975 and a diameter of 1.06 m, using values listed in Table 1. Each individual parameter study indicates the perturbation from this baseline shell, while holding the remaining values constant. The first parameter to account for variation to manufacturing fluctuations and different types of shell designs is the thickness of the shell to determine the effect on the specular reflection as well as the MFE. The MFE is presented in literature to only exist in thin shell designs. As stated previously the guided wave phenomenon can still exist for thicker shells or even solid elastic objects, though the physics for a guided wave in these cases differs

from the Lamb type waves that create the MFE to Rayleigh type waves in these cases.

2.4.1 Specular

Additionally to verify the shell model as well as determine expected response from a shell given different filler materials, it is important to look at the reflected amplitudes of the specular reflection from low-mid frequency acoustic excitation. This was done by two approaches: the first being measurement from the shell model introduced in Section 2.2, and the other being an implementation of a theoretical reflection coefficient for a three medium interface. The first method is taken from the synthesized time series from the shell model to determine the amplitude for two different filler materials at various shell thicknesses to verify the reflection was due to the shell outer medium interface, and not the reflection from the internal medium.

The three medium infinite plane problem is a standard problem that has been solved [49]. For the case of the shell the first medium (1) is the water outer medium, the second medium (2) is the shell material, and the third medium (3) is the filler material. Applying this method to estimate reflection amplitude from the thin spherical shell is an approximation, and only being used to verify that the calculated values of the specular reflection are reasonable. Furthermore, to obtain an estimate of the broadband reflection and to compare the modeled reflected amplitude, we can average the reflection coefficient over the frequency range of interest.

$$R = \frac{(1 - r_1/r_3)cos(k_2L) + j(r_2/r_3 - r_1/r_2)sin(k_2L)}{(1 + r_1/r_3)cos(k_2L) + j(r_2/r_3 + r_1/r_2)sin(k_2L)} \tag{15}$$

where r_n (medium=1,2,3) is the acoustic impedance of the medium (i.e. $\rho_n c_n$), k is the wave number, and L is the thickness of medium 2 [49]. This equation assumes a narrow bandwidth for calculating the reflection coefficient.

Fig. 2.6 displays the results of the two methods for estimating the specular reflection from an excitation of a broadband plane wave. This study allows additional

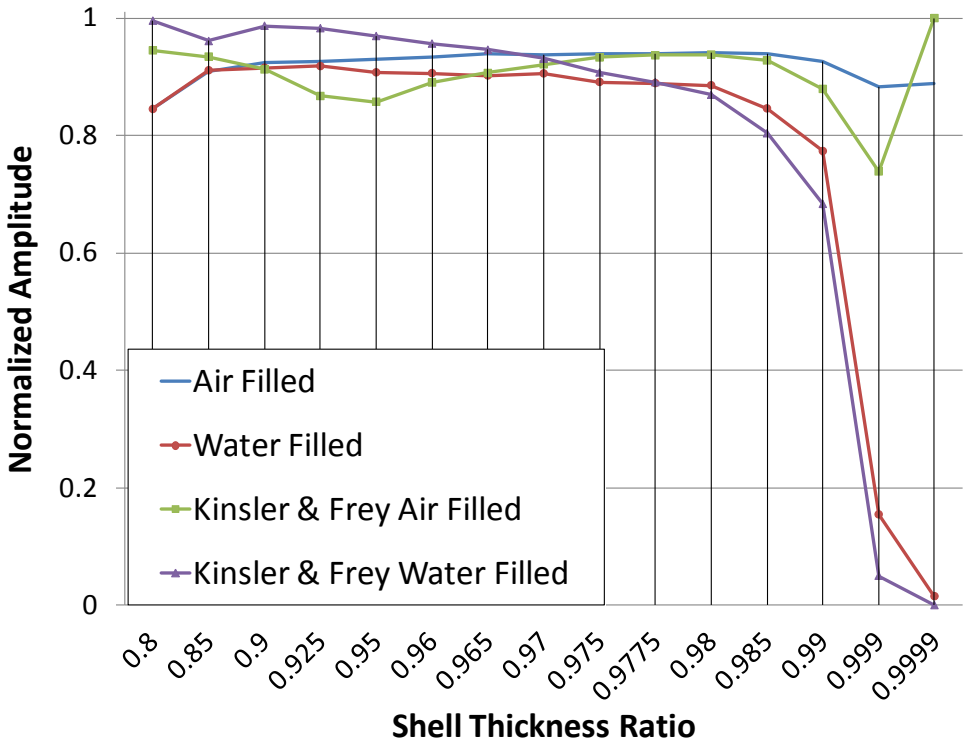

Figure 2.6: Specular Amplitude Reflection from Shell for Low to mid-frequency pulse.

validation of the numerical model that shows for very thin shells (Thickness ratio $>$ .99) the reflected wave amplitude results in an acoustically transparent shell when filled with a matched inner medium (specular reflection drops to 0).

2.4.2 Shell Thickness

Variations in design require the MFE to be robust and exist for different thicknesses and material selections. Fig. 2.7 depicts that the MFE amplitude has a peak at a thickness ratio of 0.9775. The amplitude decreases at lower ratios (thicker) due to the decrease of the lamb-wave formation, whereas the dip in the higher ratio (thinner) occurs because the shell becomes acoustically transparent at the thinner ratios.

Moreover, the shell thickness has an impact on the apparent center frequency of the MFE. Table 2 shows that between a 0.85 to 0.99 thickness ratio, there is

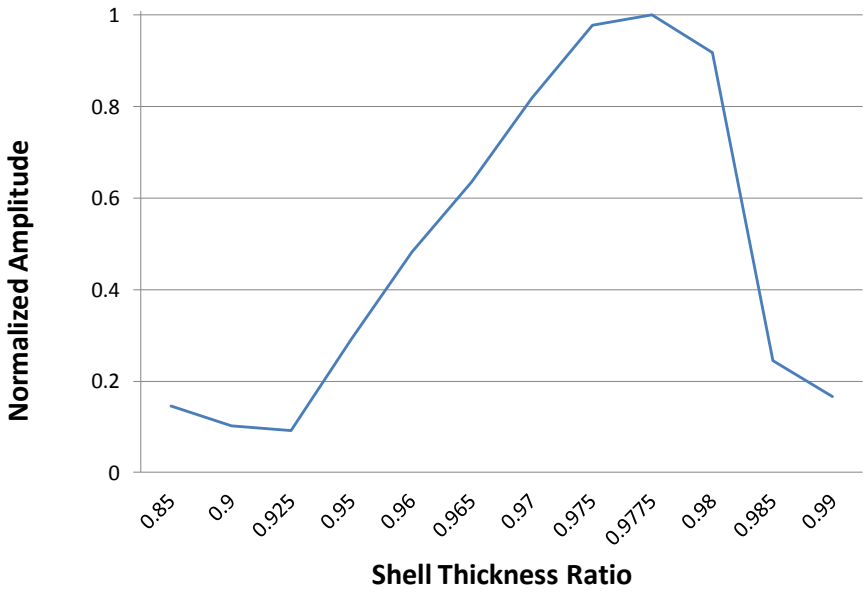

Figure 2.7: MFE Amplitude versus Shell Thickness

approximately significant change in the apparent center frequency of the MFE. This change in frequency helps to show that the apparent frequency is a result of the dispersion relationship and radiation damping of the antisymmetric waves in the shell, which vary with a change in shell thickness. It is important to note that the thicker results in a lower MFE frequency which merges with other features of thicker shells [29].

Table 2: MFE frequency for shell thickness

Shell Thickness (ratio)	Center Frequency (Hz)
0.85	3900
0.925	5600
0.95	10100
0.975	22500
0.98	28100
0.99	56000

2.4.3 Shell Material

The next parameter in this study for the spherical shell keeps the shell thickness constant at 0.975 and changes the shell material to various structural materials with a range of wave speeds and densities. For each of the different materials, the MFE exists and the difference in acoustic impedance effects appears to shift the center frequency of the MFE. The non-metallic materials for the shell have a lower sound speed and densities which have a significant impact on the frequency of the MFE. It is important to note a limitation of the model assuming homogeneous material properties, which is not true of the composite materials (e.g. fiberglass, carbon fiber) listed in the table, further study is necessary to determine the effects of the inhomogeneities and the anisotropic propagation effects inherent in these materials. An approximate relationship between the material and MFE was found by Gaunaurd et al. [29] to rely on several factors including the MFE center frequency f_{MFE}, sound speed of outer medium c_w, and thickness of the shell h and is given by:

$$f_{MFE} = \frac{\gamma c_w}{2\pi h} \tag{16}$$

The γ coefficient is a material constant that is calculated from the complex form function and ranges from values $0.8 < \gamma < 2.4$. This relationship has been shown to be useful for the classification of simple shells by predetermining the γ parameter for a shell then estimating the thickness based on the recorded frequency of the MFE [1].

Additionally the bandwidth and amplitude can be impacted by the difference in shell material. As Fig. 2.8 shows for the two different shell materials the specular remains constant and the arrival time, center frequency, and amplitude vary. The amplitudes of the MFE for the fiberglass and acrylic shell materials result in -7.7 dB and -10.1 dB with respect to the specular, whereas the steel shell had an MFE amplitude of -1.1 dB. This may make these guided waves more difficult to detect in the presence of noise, and may require further processing to detect the signal.

Table 3: Shell material for parameter study

Material	Compression Velocity (m/s)	Shear Velocity (m/s)	Density (kg/m^3)	Center Frequency (Hz)
Steel	5960	3235	7850	19700
Steel Alloy	5554	3021	6217	22500
Titanium	6070	3125	4540	22000
Aluminum	6420	3040	2710	25100
Magnesium	5770	3050	1740	29900
Brass	4700	2110	8575	33000
Fiberglass	3500	1720	1875	32800
Acrylic	2718	1283	1180	21000
Carbon Fiber	2970	1956	1800	43800
Subsonic Material	1300	1100	1180	40240

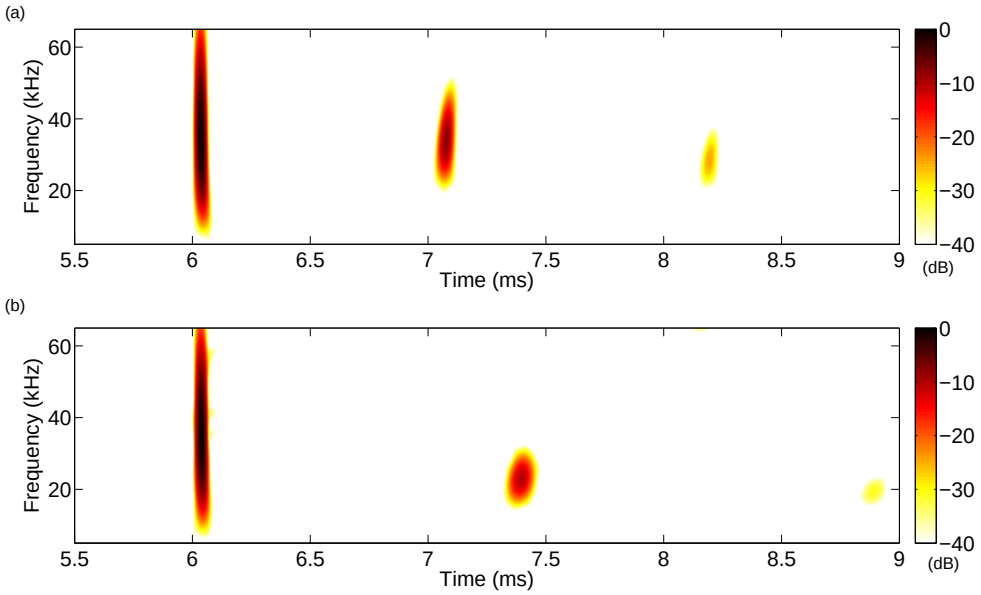

Figure 2.8: Time-Frequency representations for spherical shell surrounded by water and filled with air, and different shell materials of (a) Fiberglass and (b) Acrylic. Material parameters are listed in Table 3.

2.4.4 Shell Size

Results of running different shell sizes indicated the center frequency scales with respect to ka and arrival time depends on the path length of the guided waves. The

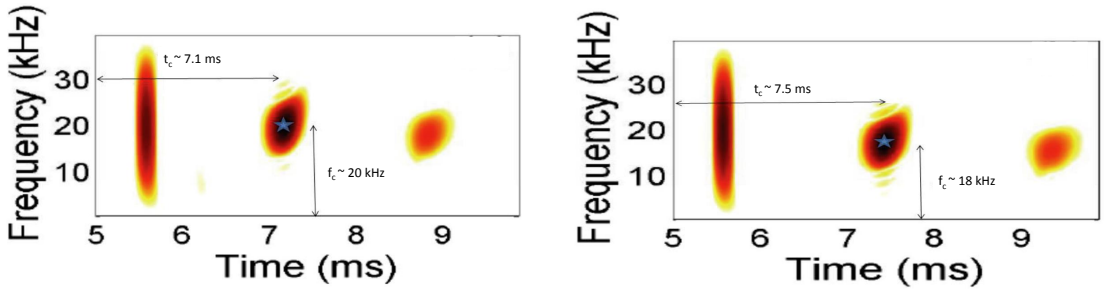

(a) (b)

Figure 2.9: Comparison figure depicting the difference in arrival time and frequency between two shells of size (a) a = 0.53 m and (b) a = 0.60 m.

shell size changes reveal a delay in time of arrival of the MFE, and subsequent repetitions are based on path length of the waves circumnavigating the shell. This is to say that for a bigger shell, the path length, and thus arrival time of the MFE increases. Additionally the amplitude decreases due to the increased path length and radiation damping. Fig. 2.9 is the time-frequency result of two spherical shells, to illustrate the time and center frequency change with an increase of shell size.

2.4.5 Outer Medium Effects

Table 4: Outer Medium Effect (Properties from [33])

Material	Compression Velocity (m/s)	Density (kg/m^3)	Center Frequency (Hz)
Water	1470	1000	20000
Clay	1517	1480	20100
Silt	1615	1740	20600
Sand	1759	1962	21100

The scope of the detection problem outlined as the motivation provides that the objects are able to be detected when buried in sediment, and therefore the study includes the effect on the MFE for different outer mediums (results are shown in Table 4). The results indicated that the outer medium influences both the amplitude and center frequency of the MFE. Incidentally, the ability of the outer medium to

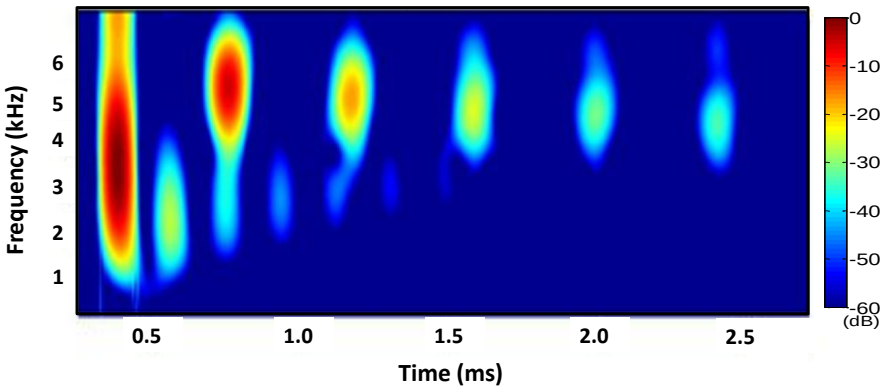

Figure 2.10: SPWV representation of a stainless steel shell surrounded by outer medium of sand in free space.

transfer shear waves increases the coupling of the first symmetric S_0 mode, which now radiates more strongly (shown in Fig. 2.10).

2.4.6 Inner Medium Effects

Table 5: Filler Material Properties

Material	Compression Velocity (m/s)	Density (kg/m^3)
Air	331	1.29
Water	1470	1000
Oil	1460	942
Plastic	2480	2176

For additional robustness and potential classification of a given target the parameter study included different filler materials, shown in Table 5. Because the MFE is a result of waves in the shell materials the A_0 modes still exist with various materials filling the shell. The air-filled shell maintains the clearest signature for identifying the MFE due to the lack of sound coupling with the inner material, and thus there is little to no sound reflecting internally within the spherical shell. Due to model limitations, the plastic filler was modeled as a high speed dense fluid with no shear wave speed, and therefore is probably missing some of the scattering structure. Two ways

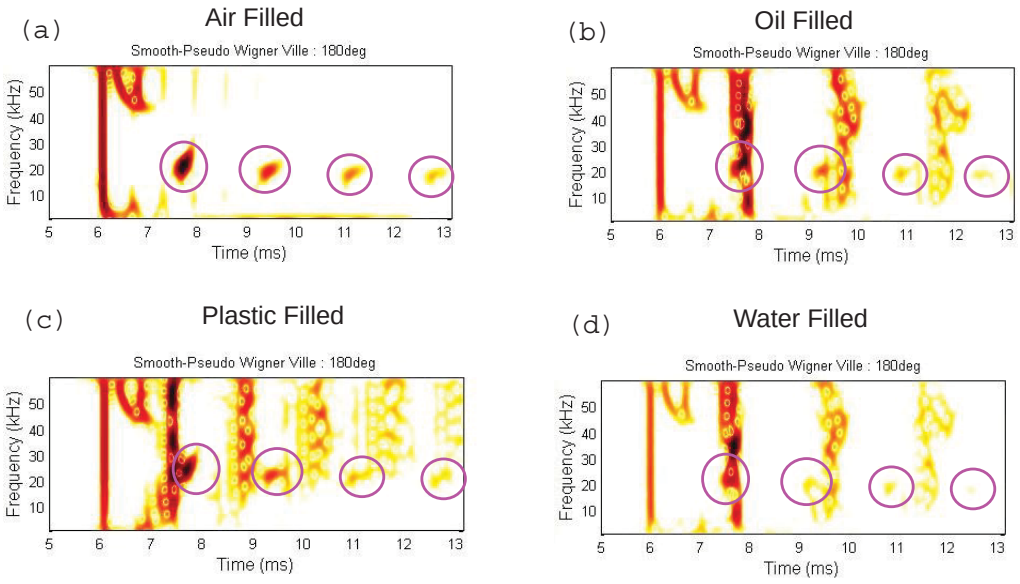

Figure 2.11: SPWV time frequency representation of backscatter response for various filler material. Spherical Shell filler materials, where the expected MFE arrival and replicas are indicated for each test case. (a) Air filled (b) Oil Filled (c) Plastic Filled (d) Water Filled.

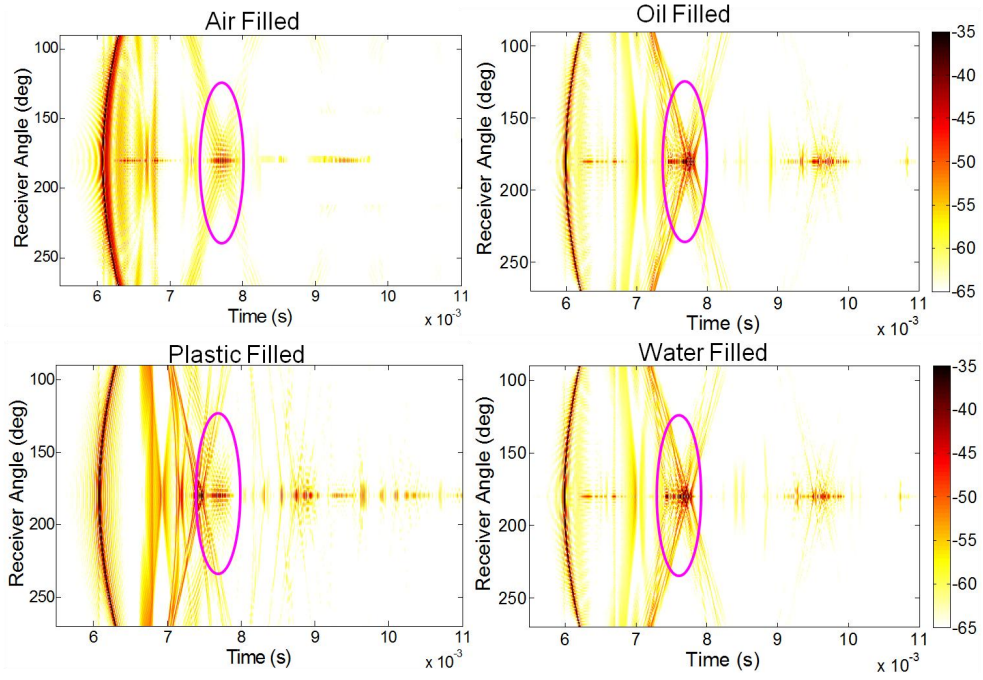

Figure 2.12: Bistatic Sinograms of Spherical Shell filler materials, where the expected MFE Energy is indicated for each test case. (a) Air filled (b) Oil Filled (c) Plastic Filled (d) Water Filled.

in which the existence of the MFE was analyzed in the shell are the time-frequency domain and the energy plotted over various receiver angles. For the air filled shell, these representations are seen in top left panel Fig. 2.11 and Fig. 2.12.

A look at the time frequency representations of the different filler materials allows a closer examination of robustness of the MFE. The MFE and its replicas are highlighted. The propagation of sound through the filler material, and internal reflections create some complications, with interference between the MFE and internal specular bounces. As expected the frequency and repetition rate do not change for the different filler materials. A broadband signal, expected to be the reflection off the back wall of the sphere obscures the MFE for the materials with higher acoustic impedance. Even with these complications, it is evident the MFE is present and can be used for detection. Although the MFE appears buried in the signal due to presence of internal reflections, the use of a time frequency filter method as presented by Cheveret et al. could be implemented to isolate the MFE from the recorded signal. Fig. 2.13a displays the results of a applying a time-frequency filter created from the air-filled response (Fig. 2.11a) to isolate the MFE from the internal reflections for the water-filled case (Fig. 2.11d). This filter results in an MFE amplitude of -0.8 dB with respect to the specular amplitude. Fig. 2.13b displays this same filter applied to a thicker shell (ratio = 0.9), which does not have the same expected MFE frequency, and shows that there is much lower energy (-18.1 dB) present at the MFE time-frequency filter location. Thus, this feature and method could be used to classify a target in the presence of a noisy environment, or internal reflections[14].

An additional method to verify the MFE presence and reduce the effect of the internal reflections for detection is to look at the scattered field with bistatic receivers, which would allow varying separation in time of the features. Fig. 2.12 reveals that the X-pattern of the antisymmetric wave from a bistatic sinogram which is easy to identify and shows the existence of the MFE. This X-pattern is caused by the

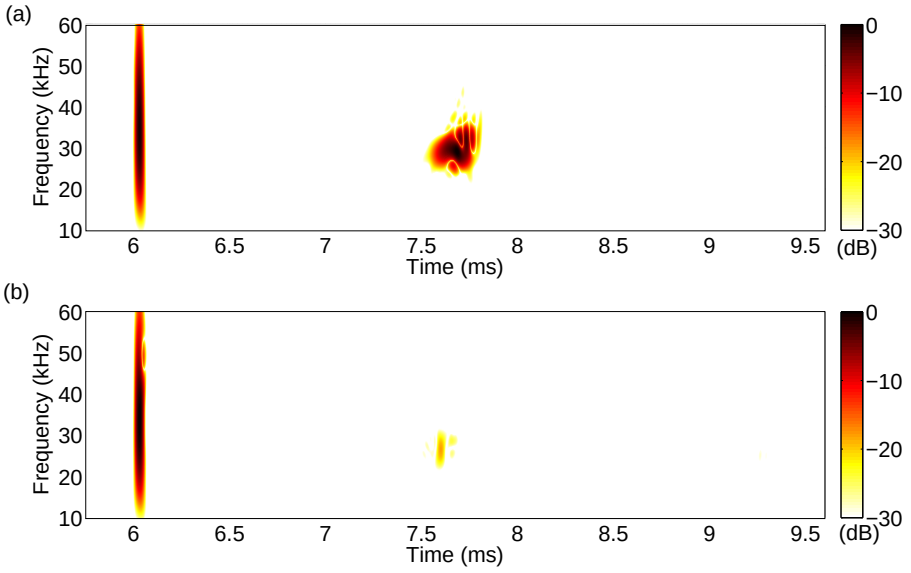

Figure 2.13: SPWV time frequency representation of time-frequency filtered backscatter response for water filled shell applied to two thickness ratios (a) 0.975 and (b) 0.9.

separation of the clockwise and counter clockwise waves (further discussion will be presented in Chapter III).

2.4.7 Parameter Study Summary

The time-frequency analysis in the backscatter region for the various parameters in this study revealed the MFE to be robust to numerous design parameters, and each providing a shift in time or frequency that can be useful for classification. The frequency typically was shifted down when the stiffness of a shell was decreased (by material, size, thickness etc). The results are summarized below:

Specular Specular return remains present except for extremely thin ($> 0.999\%$) for the broadband low frequency excitation.

Thickness There is an increased amplitude of the MFE for thickness ranges between $97 - 98\%$, and the center frequency is decreased as thickness decreases (i.e. less stiff).

Shell Material Each material has a variation in the center frequency that is dependent on the material, since the MFE is dependent on the dispersion behavior which is material dependent. Additionally the bandwidth and amplitude can be impacted by the shell material.

Shell Size A shift in time and frequency occurs for a change in shell size, where the bigger the diameter results in a later arrival and lower frequency.

Outer Medium The outer medium shifts the center frequency and enhances the coupling of the lowest symmetric wave.

Filler Material Inner filler complicates the wave field due to internal reflections and coupling, but the MFE remains present.

2.5 Discussion and Summary

This chapter built on the fundamental knowledge of acoustics to present the methods employed in the research. The theory and numerical model for a spherical shell was presented, and the scattered field was discussed. The basis for numerical tools in this analysis of the scattered field was covered and applied to the monostatic receiver position to familiarize the reader with previous work. Then, the results of a problem parameter study were covered in detail to present the trends and response of the MFE to various design changes. This extensive parameter study contributes to previous literature and confirms trends expected to be useful for classification purposes. The following chapter will extend the knowledge and work previously completed in the literature to highlight and fill a gap in the documented knowledge of the scattered field from a spherical target.

CHAPTER III

BISTATIC ACOUSTIC SCATTERING AND PROCESSING

This chapter[1] extends the knowledge and methods presented in Chapter II to cover the analysis of the bistatic scattering from an elastic sphere. Previous work with time-frequency analysis of the MFE have focused on source-receiver configuration close to monostatic where the MFE is most energetic, when source and receiver are closely spaced with respect to the shell [46, 48, 53]. This work contributes the new knowledge of the time-frequency analysis of the variations of the MFE in the bistatic configuration.

The MFE persists for bistatic configurations and thus still carries information about the physical features of the elastic shell (e.g. see Fig. 3.1). However, a practical challenge is that the amplitude of the bistatic MFE is significantly reduced when compared to monostatic measurements, which render its detection more difficult in the presence of high clutter or ambient noise levels. Consequently, bistatic detection of the MFE would need to be enhanced, for instance, by combining the signals measured on an array of receivers using array beamforming techniques [52]. The design of an optimal beamformer for detection applications should then be determined by the specific time-frequency coherence of the bistatic MFE echoes, in order to allow for an optimal coherent addition of these echoes across a bistatic aperture [89].

The main goal and contribution of the research in this chapter is to investigate theoretically and numerically the bistatic variations of the MFE for a fluid-loaded and

[1]Part of this work is published in The Journal of the Acoustical Society of Acoustics "Time-frequency analysis of the bistatic acoustic scattering from a spherical elastic shell" [5].

thin spherical shell. Additionally, the research will quantify the dependence of time-frequency shift of the MFE on the bistatic receiver angles and explain the observed shifts using a previously derived quantitative ray theory for spherical shell scattering. The time-frequency analysis of the most energetic bistatic echo, associated with the circumnavigating antisymmetric Lamb waves, is performed using the Wigner-Ville transform because it can provide an unbiased group velocity estimation that in turn can be used for characterizing a shell's physical properties [103, 105, 102].

This chapter will present the work of time-frequency analysis extended into the bistatic domain for elastic contributions to the scattered field. The chapter is divided into six sections. Section 3.1 presents the bistatic scattering from a spherical shell. Section 3.2 investigates the bistatic evolution of the MFE arrival in the time and frequency domains. Section 3.3 develops the quantitative ray interpretation to explain the observed time-frequency shifts of the bistatic MFE arrival. Based on the previous findings, section 3.4 extends the interpretation and behavior to Rayleigh waves propagating around a solid elastic cylinder. Section 3.5 presents a generalized time-frequency beamformer formulation to coherently process MFE echoes recorded along a bistatic sensor array. Finally, the findings and contributions are summarized.

3.1 Bistatic Scattering from Spherical Shell

One method of investigating behavior of the bistatic data is to track the time evolution of acoustic energy across a bistatic receiver array. This method has ties to RADAR and medical imaging. Fig. 3.1 displays the evolution of the envelope of the simulated bistatic responses of the elastic shell, computed using Eq. (10) and the model parameters listed in Table 1, for a full 360° revolution of the receiver angle θ. The receiver was kept a constant distance, $r = 10$ m, from the sphere's centroid. It is important to note that the values displayed for $\theta = 180°$ correspond to the envelope of the monostatic time-series shown in Fig. 2.3. The first wavefront visible on this

time-angle representation, with nearly constant amplitude over all receiver angles, corresponds to the specular reflection of the shell. The two branches of the following "X-shaped" pattern between 6.5 ms$\leq t \leq$ 8.5 ms, labeled "c" and "cc" on Fig. 3.1, corresponds respectively to the interference of the circumnavigating components of the A_{0^-} waves or MFE propagating in the clockwise and counter-clockwise directions. This difference in arrival times between the clockwise and counter-clockwise interference patterns can be simply explained from a geometric ray analysis, as presented in the next section (see Fig. 3.3). Furthermore, as expected, these clockwise and counter-clockwise interference patterns intersect in the monostatic direction $\theta = 180°$, as they both have the same path length around the shell before reaching the receiver. Consequently, the MFE pattern is most energetic in the monostatic configuration where all the wave components interfere constructively.

As shown quantitatively on Fig. 3.1, the energetic MFE pattern begins to split into two branches as the receiver moves away from the monostatic configuration ($\theta = 180°$), and the MFE amplitude rapidly decays [48]. Consequently, for practical MCM applications in noisy environments, bistatic measurements of the MFE would likely need to be combined coherently, using array processing, in order to enhance the bistatic detection of the MFE pattern. However, a coherent combination of these bistatic A_{0^-} wave echoes, using standard time-delay beamforming by compensating for their relative time shift, would not be optimal if the frequency content of the MFE varies with each bistatic receiver angle θ. To test this hypothesis, the SPWV transform, as described in Chapter II (see Eq. (13)), is used hereafter to investigate the time-frequency analysis of the bistatic MFE pattern.

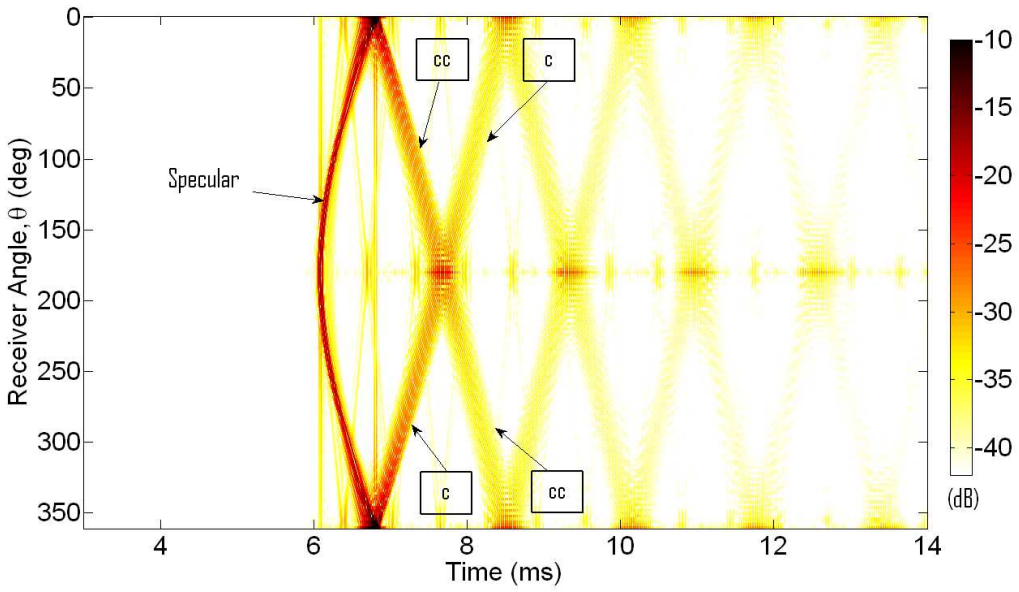

Figure 3.1: Evolution of the envelope (in logarithmic scale) of the bistatic impulse response of the spherical shell (computed with Eq. (10) using the model parameters listed in Table 1) vs. bistatic angle, θ. The amplitudes were normalized with respect to the maximum values of the scattered field in the monostatic (or backscatter) direction $\theta = 180°$. The first curved arrival corresponds to the specular echo. The two branches of the subsequent X-shaped pattern correspond respectively to the counter-clockwise ("cc" symbol) and clockwise ("c" symbol) propagating components of the A_0 mode. Note that the arrival-times of these two components differ for bistatic receivers (see Fig. 3.3), except for the monostatic direction $\theta = 180°$ where their path around the spherical shell become symmetric with equal lengths.

3.2 Time-Frequency Analysis of the Bistatic Evolution of Spherical Shell's Scattered Field

Fig. 3.2 depicts the SPWV of the time-series computed for three different bistatic angles spaced apart by 45° ($\theta = 180°, 135°, 90°$). The selected smoothing functions for the SPWV analysis were Hann windows yielding respectively a time and frequency resolution of 1.5 μs and 200 Hz (see Eq. (2)). As predicted, the SPWV associated with angles $\theta = 135°$ and $\theta = 90°$ illustrates the splitting of the energetic main MFE pattern's arrival (as shown for $\theta = 180°$, see Fig. 3.2a) into two weaker distinct arrivals with the left (resp. right) pattern corresponding to counter-clockwise (resp. clockwise) interference pattern, as labeled on Fig. 3.2b-c. Less intuitively,

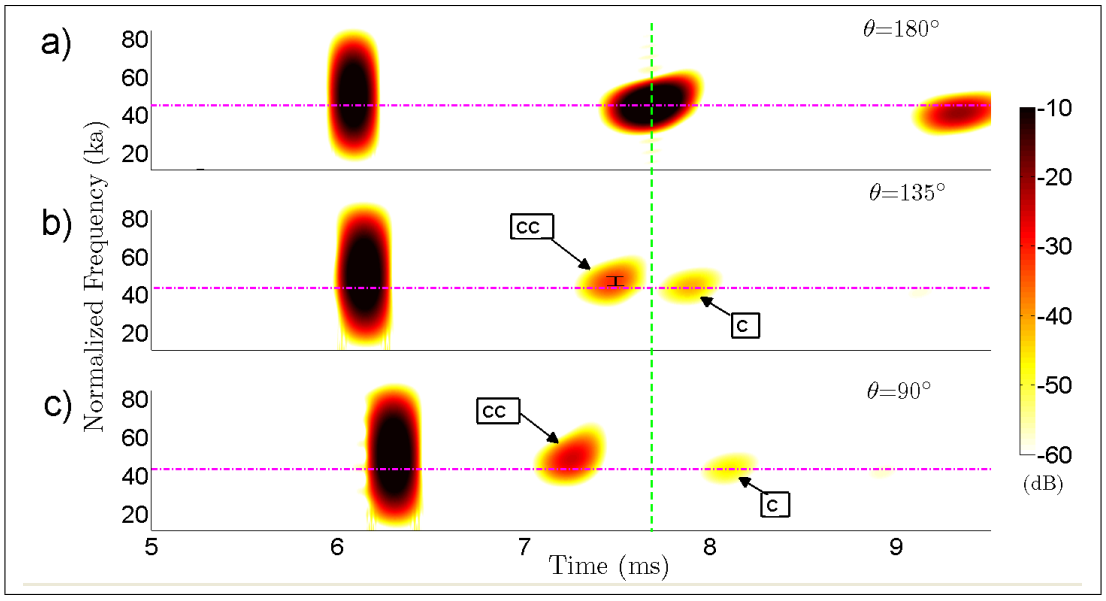

Figure 3.2: Smoothed Pseudo-Wigner Ville representation (in logarithmic scale) of the impulse response of the spherical shell for three representative receiver's azimuth angles (a) monostatic direction $\theta = 180°$, or bistatic directions (b) $\theta = 135°$ and (c) $\theta = 90°$. The energetic MFE echo due to the interference of the clockwise and counterclockwise propagating A_{0^-} wave in the monostatic direction is visible at time $t = 7.66$ ms (dashed vertical line) and a normalized frequency $ka = 46$ (dashed horizontal line). The bistatic configurations illustrate the progressive splitting of the MFE echo into two distinct clockwise and counterclockwise arrivals (see Fig. 3.1), as well as their relative time-frequency shift with respect to the monostatic echo. For each angle, the magnitude was normalized by the maximum displayed value.

this time-frequency analysis also reveals that the counter-clockwise (resp. clockwise) MFE pattern exhibits an upward (resp. downward) frequency shift of $+1.8$ ka (or -1.1 ka) for $\theta = 135°$ when compared to the monostatic MFE pattern. A physical interpretation of this time-frequency shift will be presented in the next section using a quantitative ray analysis for spherical shell's scattering [106]. Furthermore, as discussed later in Section 3.5, a generalized time-frequency beamformer can be developed to compensate for the observed time-frequency shifts of the bistatic MFE as revealed by the SPWV analysis. Similar time-frequency beamformers have previously been developed for compensating wideband Doppler effects when tracking a moving source [94].

3.3 Physical Interpretation of the Time-Frequency Evolution of the Bistatic MFE Pattern from Quantitative Ray Theory

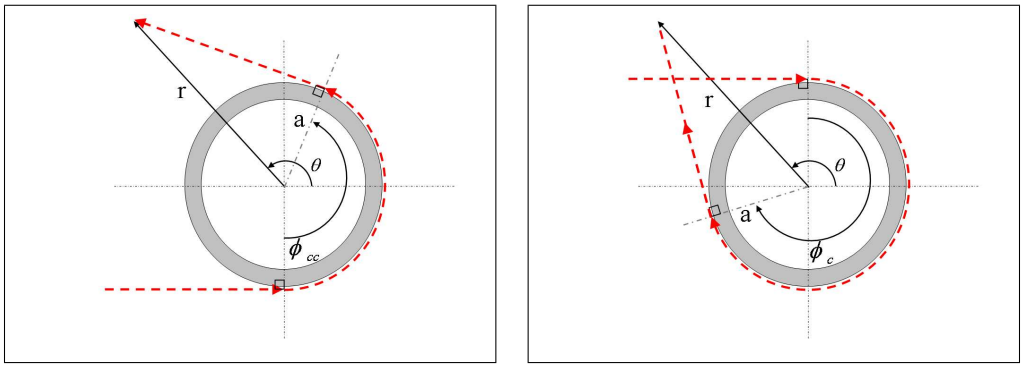

(a) (b)

Figure 3.3: Bistatic ray diagrams for the subsonic A_{0^-} wave in the vicinity of the coincidence frequency for (a) the counter-clockwise or (b) the clockwise propagating components. Note the difference in arc path angles ϕ_{cc} and ϕ_c for respectively the counter-clockwise or clockwise components (see Eq. (20-21)) and that $\alpha = \frac{\pi}{2}$ for the subsonic A_{0^-} wave. The bistatic receiver is located at a distance r and azimuth angle θ.

3.3.1 Overview of the Quantitative Ray Theory for a Spherical Shell

Extensive literature has been published on the quantitative ray theory for scattered fields from elastic targets of various shapes [55, 97]. This work created ray approximations of the work completed in the 1970's which developed work fully describe and model the scattered field from spherical and cylindrical shells by means of the resonant scattering theory and exact partial-wave series [18, 19, 25, 90]. Consequently, only a terse summary of the quantitative ray theory applied to spherical shells is presented hereafter.

The Resonance Scattering Theory can be used to calculate and identify the target resonances and their relation to the geometrical and material properties of the elastic object. Some previous work has presented a target recognition scheme based on the analysis of the resonance response from the elastic objects [25]. Theoretical analysis

and tank experiments focusing on the scattering from elastic shells were conducted throughout the 1980's and early 90's by various authors such as Kargl and Marston [48, 55]. These studies presented modeling of the backscattering from elastic spherical shells in terms of Lamb wave returns, axial reverberations, and glory effects, often using a generalization of the theory of geometric diffraction to elastic objects in water [25, 65, 91, 55]. Their work investigated the plane wave scattering from elastic spheres and cylinders in terms of infinite partial-wave series and introduced the Sommerfeld-Watson transformation to this application, which led to Ray theory approximations.

Ray theory approximations provide a high-frequency approximation to the Helmholtz equation. This high frequency approximation holds for the smooth geometry transitions and coupling that occurs near the MFE frequencies [55]. It is an intuitive approach originally attributed to Euclid that predates a mathematical formulation. Applying the Fermat principle to the ray method essentially states a path exists that has the minimum travel time from a source to receiver, which can include the guided waves as seen in Chapter II. The approximate ray analysis provides a physical basis for an intuitive interpretation of the different echoes and their paths including the specular and A_0 waves, which are visible on the simulated bistatic time-series (e.g. see Fig. 2.3 and Fig. 3.1). In particular, this geometric approach associates an individual ray component with each of the various specular and guided surface wave components within the shell, as shown qualitatively on Fig. 1.3. This simple ray theory has been shown to be quantitatively accurate [55, 97] and only needs a slight correction in the forward scatter direction (i.e. $\theta \approx 0^\circ$) to account for forward diffraction effects around the shell. The arrival time of each ray component can be computed from a geometric calculation of its path length around the shell and within the surrounding medium. Furthermore, the quantitative ray analysis presented hereafter will be focused on the most energetic MFE, which correspond to the interference of the A_0–wave components as discussed in Chapter II. In particular, based on the matched

boundary conditions at the interface between the shell's wall and the surrounding medium, the angle of incidence α_i with respect to the normal of the shell's surface, as shown on Fig. 1.3, for a ray associated with either of the A_0 wave components, A_{0^-} and A_{0^+}, is determined by

$$\sin(\alpha(f_c)) = \frac{C_0}{C_{phase}(f_c)} \tag{17}$$

where f_c is the frequency of the harmonic excitation, C_0 is the sound speed of the surrounding fluid, and $C_{phase}(f_c)$ is the frequency-dependent phase velocity of the A_{0^+} or A_{0^-} wave components (see Fig. 3.4a). Note that this angle, α, is also the launch angle of the ray radiating out from the shell (see Fig. 1.3). Based on the selected parameters for the elastic shell (see Table 1) it can be noted that the phase velocities of the A_{0^-} and A_{0^+} components come close to the value of the sound velocity of the surrounding fluid $C_0 = 1500\ m/s$ (see Fig. 1.3), in the vicinity of the coincidence frequency (i.e. where the MFE occurs), i.e. $ka \approx 46$. Additionally the group velocity curves of the A_{0^-} and A_{0^+} components intersect at the coincidence frequency (as shown in Fig. 3.4b), which indicates an efficient energy coupling and, thus, strong constructive interference of the A_0 components as reported earlier [106].

Previous developments of the quantitative ray theory can be used to predict the amplitude variations of the A_{0^-} and A_{0^+} components in the vicinity of the MFE [106]. Assuming that an incident harmonic plane wave with amplitude P_0 and frequency ω impinges on a shell in a homogeneous free space medium with sound speed C_0, the harmonic scattered field, $P(r, \phi, t)$, recorded at a range r is expressed as a superposition of the various ray components.

$$P(r, \phi, t) = \frac{P_0}{r} e^{i(kr - wt)} \sum_{l}^{\infty} f_{l,m}(\phi) \tag{18}$$

Where the angle (ϕ) parameterizes the angle of the arc path of each l^{th} ray component (see Fig. 3.3), each having a complex amplitude $f_{l,m}(\phi)$ (commonly referred to as the form-function). The second index $m = 0, 1, 2...$ denotes the number of full

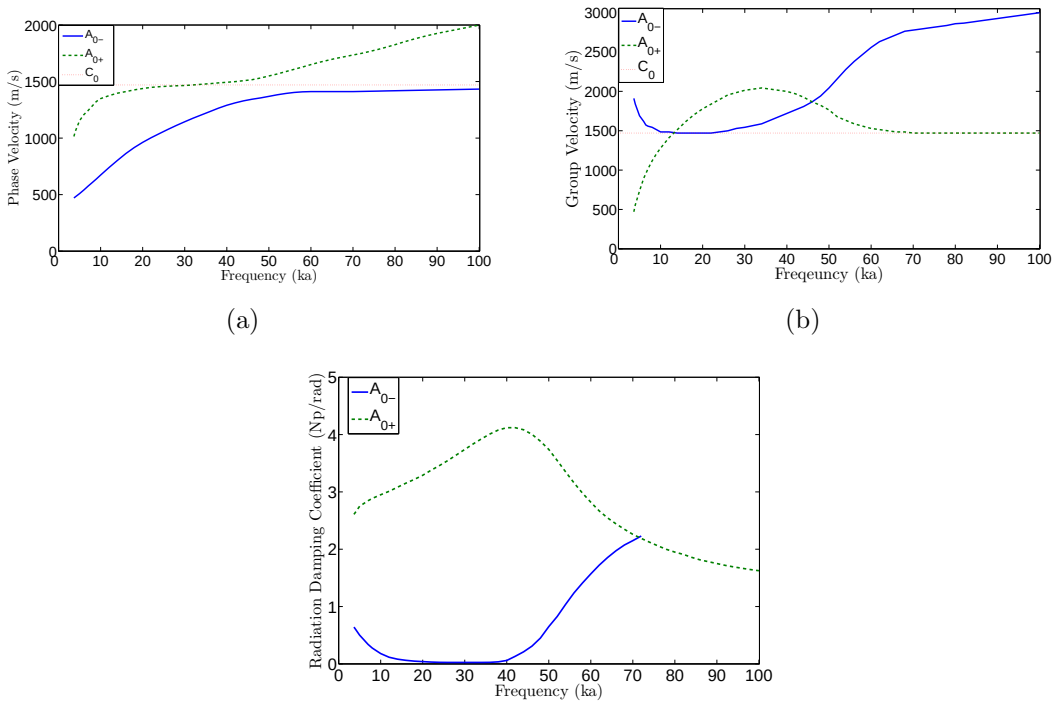

Figure 3.4: Evolution of (a) Phase velocities, (b) Group velocities, and (c) Radiation damping coefficients vs. normalized frequency ka for the antisymmetric guided wave modes A_{0+} (dashed line) and A_{0-} (solid line)-adapted from Fig. B1 in Zhang et al [106]

.

circumnavigations of the individual ray components around the spherical shell. In particular, the form function associated with the antisymmetric A_0 Lamb waves (i.e. either the A_{0+} or A_{0-} components) can be approximated by [106]

$$f_{l,m}(\phi) = B_l e^{i\eta_l} \beta_l e^{(-\phi\beta_l - 2\pi m\beta_l)} \tag{19}$$

where B_l is a complex constant whose exact expression differs for the A_{0+} or A_{0-} component, η_l is a propagation related phase shift parameter, and β_l (Np/rad) is the radiation damping parameter for the considered A_0 component. Physically speaking, the parameter η_l determines the arrival time of the A_{0+} or A_{0-} waves, and the parameter β_l quantifies the amount of energy radiated by these waves into the surrounding fluid while circumnavigating the spherical shell. Fig. 3.4c displays the frequency

dependence of the radiation damping modal coefficients for the A_{0+} or A_{0-} waves computed using the shell's physical parameters listed in Table 1 (the curves were adapted from a previous study by Zhang et al. for a spherical shell with identical physical parameters [106].) In the vicinity of the coincidence frequency (i.e. $ka \approx 46$) the radiation damping parameter of the A_{0-} wave is significantly lower than the radiation damping parameter of the A_{0+} wave. Consequently, this indicates that the A_{0-} wave is radiating out most of the energy associated with the MFE. Therefore, the theoretical variations of the form function $f_{l,m=0}$, predicted from Eq. (19) and the geometric path length of the ray associated with the A_{0-} wave will be used hereafter to quantify the observed time-frequency shift of the bistatic MFE arrival as observed previously (see Fig. 3.2).

3.3.2 Ray Interpretation of the Observed Time-Frequency Shift of the Bistatic MFE Arrival

In the vicinity of the MFE, the phase velocity of the A_{0-} becomes close to the value of the sound velocity of the surrounding fluid C_0 (see Fig. 3.4a). Consequently, the angle of incidence becomes $\alpha \approx \pi/2$ based on Eq. (17), which simplifies the computation of the path length of the A_{0-} wave propagating around the shell (see Fig. 3.3). For a bistatic receiver, the arc path angles ϕ_c and ϕ_{cc} of respectively the clockwise (see Fig. 3.3a) and the counter-clockwise (see Fig. 3.3b) propagating A_{0-} waves differ such that:

$$\phi_{cc}(\theta) = \frac{\pi}{2} + \theta - cos^{-1}\left(\frac{a}{r}\right) \tag{20}$$

$$\phi_{c}(\theta) = \frac{5\pi}{2} - \theta - cos^{-1}\left(\frac{a}{r}\right) \tag{21}$$

where θ is the bistatic receiver angle, a is the shell radius, and r is the distance between the sphere's centroid and the receiver distance. Note that $\phi_c = \phi_{cc}$ only when $\theta = \pi$ (i.e. for a monostatic configuration)

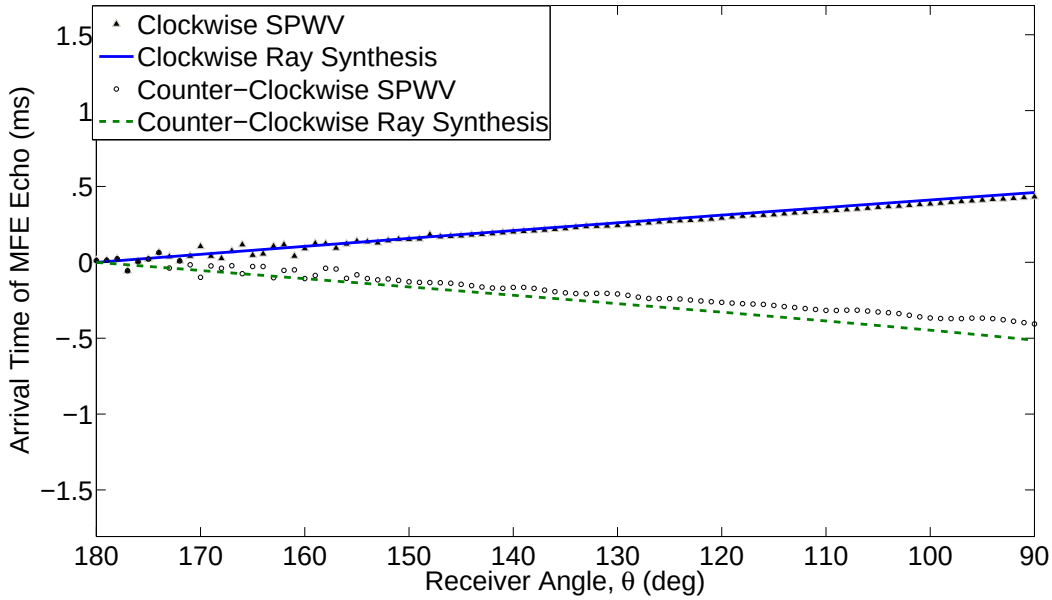

Figure 3.5: Variations of the arrival time of the MFE echo vs. bistatic receiver angle θ (see geometry in Fig. 3.3) with respect to the monostatic arrival time of the MFE (i.e. $\theta = 180°$). The triangle and circle symbols indicate the measured arrival times for, respectively, the clockwise and counter-clockwise A_{0^-} waves, as measured using the local maxima in the time-frequency plane of the smoothed pseudo Wigner-Ville representation of the bistatic scattered field (see Fig. 3.2). For comparison, the solid and dashed lines correspond to the arrival-times predicted from the ray synthesis for the same clockwise and counter-clockwise A_{0^-} waves.

Overall, the difference in path length between the clockwise and the counter-clockwise propagating A_{0^-} waves determines the apparent time-frequency shift of the bistatic MFE arrival as measured by the SPWV analysis (see Fig. 3.2). More specifically, the local maximum of the SPWV amplitude in the time-frequency plane indicates the arrival time of the propagating energy of the A_{0^-} wave packet, and is thus determined by the value of the group velocity, $C_{group}(ka = 46)$ of the A_{0^-} wave in the vicinity of the coincidence frequency (ka=46 see Fig. 3.4b) [101]. Hence for a bistatic angle θ the variations of the arrival-time for the clockwise and the counter-clockwise propagating A_{0^-} waves (with respect to the arrival times in the monostatic

configuration i.e. $\theta = \pi$) can be simply predicted from the ray analysis using the following expressions $[(\pi - \theta)a]/[C_{group}(ka = 46)]$ and $-[(\pi - \theta)a]/[C_{group}(ka = 46)]$ (for $90° \leq \theta \leq 180°$). Fig. 3.5 shows a good agreement between these linear predictions of the time-shift of the MFE arrival from the ray analysis (plain and dashed lines) and the measured values from the SPWV analysis (dotted lines) for bistatic angles varying between $90° \leq \theta \leq 180°$. The slight discrepancy visible around 90° between the measured and predicted arrival times for the counter-clockwise wave (dashed line) likely result from error in arrival-time picking from the SPWV due to interferences occurring between the S_0 arrival and the A_{0^-} arrival.

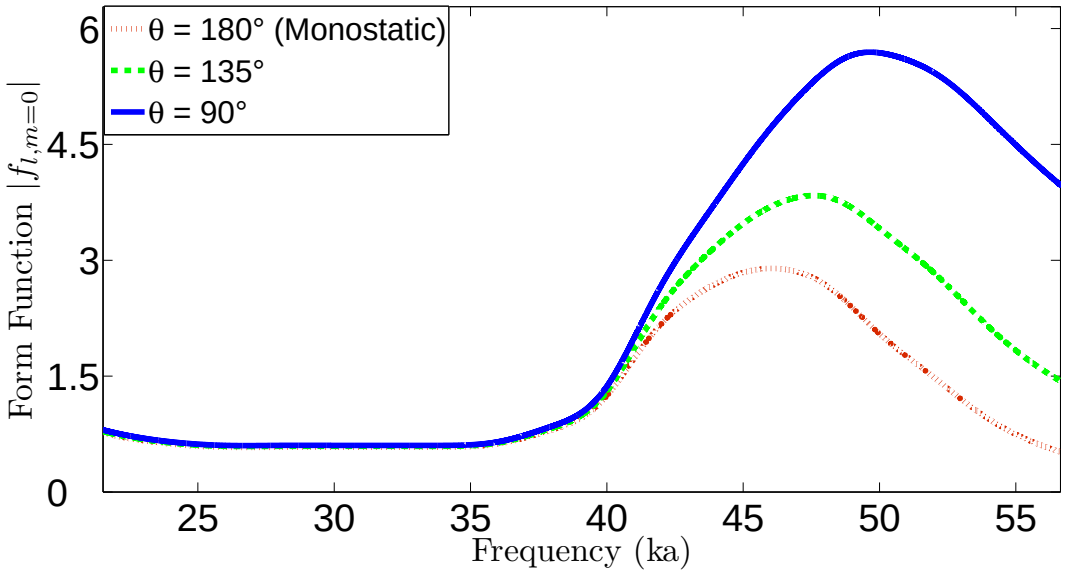

Figure 3.6: Ray models of the amplitudes of the earliest counter-clockwise A_{0^-} wave arrival (based on the form function, $f_{l,m}$ given by Eq. (19) for $m = 0$) in the vicinity of the coincidence frequency for same three bistatic receiver angles θ shown in Fig. 3.2. Note the maximum of the amplitude's enhancement in the mid-frequency region progressively increases from $ka \approx 46$ at $\theta = 180°$ to $ka \approx 49$ at $\theta = 90°$.

The quantitative ray analysis can also be used to predict the apparent frequency shift of the bistatic MFE arrival (see Fig. 3.2). More specifically, as the bistatic angle θ varies away from π, the arc path angles ϕ_c and ϕ_{cc} (see Eq. (20-21)) of

respectively the clockwise and the counter-clockwise propagating A_{0^-} waves vary as stated earlier (see Fig. 3.3). Consequently, for a given bistatic angle θ , the MFE occurs at the normalized frequency ka, which maximizes the form function associated with the ray corresponding to the first A_{0^-} arrival, i.e. $|f_{l=A_{0^-},m=0}(\phi)| = |B_l\beta_l(ka)e^{(-\phi(\theta)\beta_l(ka))}|$, for $\phi = \phi_{cc}$ or $\phi = \phi_c$ (see Eq. (20-21)). Hence the frequency dependence of the radiation damping parameter $\beta_l(ka)$ (see Fig. 3.4c) ultimately determines the apparent frequency shift of the bistatic MFE arrival. As an illustration of this phenomenon, Fig. 3.6 displays the evolution of magnitude of the form function $|f_{l=A_{0^-},m=0}(\phi)|$ for the counter-clockwise propagating A_{0^-} wave for the same three bistatic angles ($\theta = 180°, 135°, 90°$) used for the SPWV calculations shown in Fig. 3.2.

As the bistatic angle θ decreases from $\theta = 180°$ to $\theta = 90°$, it can be observed that the maximum of the form function shifts upward towards higher normalized frequency values from $ka = 46$ to $ka = 49$ (i.e. in the vicinity of the coincidence frequency) for the counter-clockwise propagating A_{0^-} wave. A similar analysis can be conducted to quantify the downward frequency shift of the clockwise propagating A_{0^-} wave. Overall, Fig. 3.7 shows a good agreement between the bistatic frequency shifts predicted by this quantitative ray analysis and the frequency-shifts values measured from the SPWV analysis (dot symbols) of the computer time-series. Furthermore, the spread of the frequency-shift measurements falls within the measurement error of the SPWV analysis, which is determined by the frequency resolution of the smoothing kernel indicated by the vertical error bar displayed on Fig. 3.7. This measurement error can potentially be mitigated by reducing the frequency smoothing of the SPWV. However doing so could increase the interference pattern artifacts of the Wigner-Ville analysis, which would in turn bias the estimation of the SPWV maxima in the time-frequency plane [16].

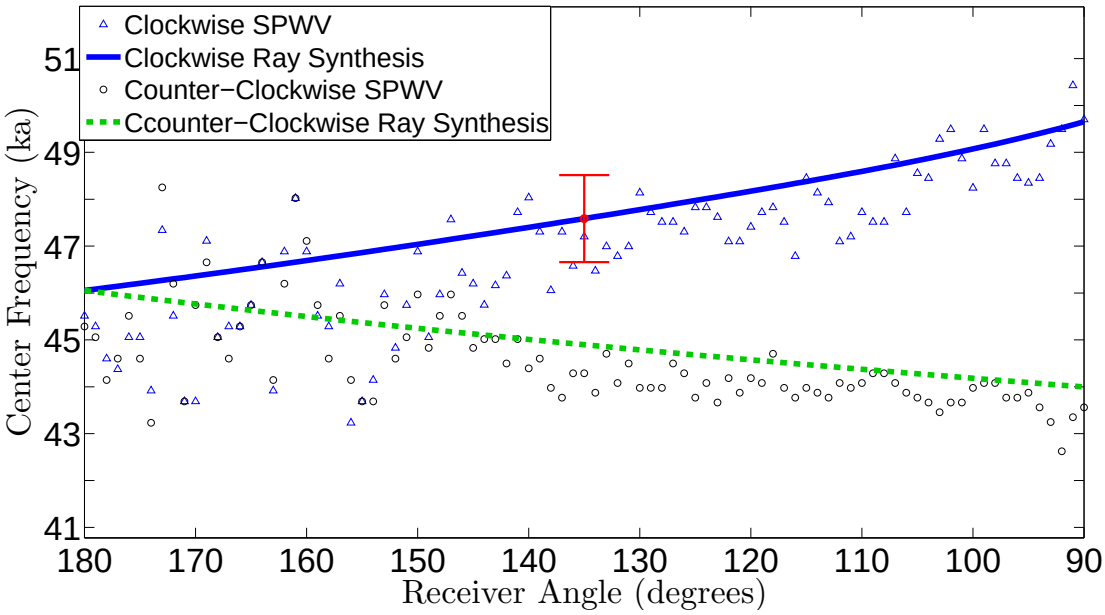

Figure 3.7: Variations of the normalized center frequency of the MFE echo or coincidence frequency vs. bistatic receiver angle θ (see geometry in Fig. 3.3) with respect to the monostatic arrival time of the MFE (i.e. $\theta = 180°$). The triangle and circle symbols indicate the center frequencies for respectively the clockwise and counter-clockwise A_0 arrival as measured from the local maxima in the time-frequency plane of the smoothed pseudo Wigner-Ville (SPWV) representation of the bistatic scattered field (see Fig. 3.3). The vertical error bar depicts the measurement resolution along the frequency axis on the SPWV representation, which accounts for most of the spread in the measured values. For comparison, the solid and dashed lines correspond to the center frequency of MFE echo predicted from the theoretical ray amplitude variations as shown on Fig. 3.6.

3.4 Bistatic Behavior for Finite Solid Elastic Cylinder

After presenting the quantitative ray theory based on the form function for a sphere, it is fruitful to note in this section the similarities and differences in behavior of the scattered field from the more complex target of a solid cylinder. Due to the single axis axisymmetry of a finite cylinder, the bistatic literature and analysis is much more in depth due to the obvious changes in bistatic detection [7, 26, 97, 57]. It has been shown bistatic views offer an improvement in detection of a simple cylinder with various viewpoints from the the specular response alone [62]. Due to the angle of reflection equaling the angle on incidence, the off-axis monostatic response from a

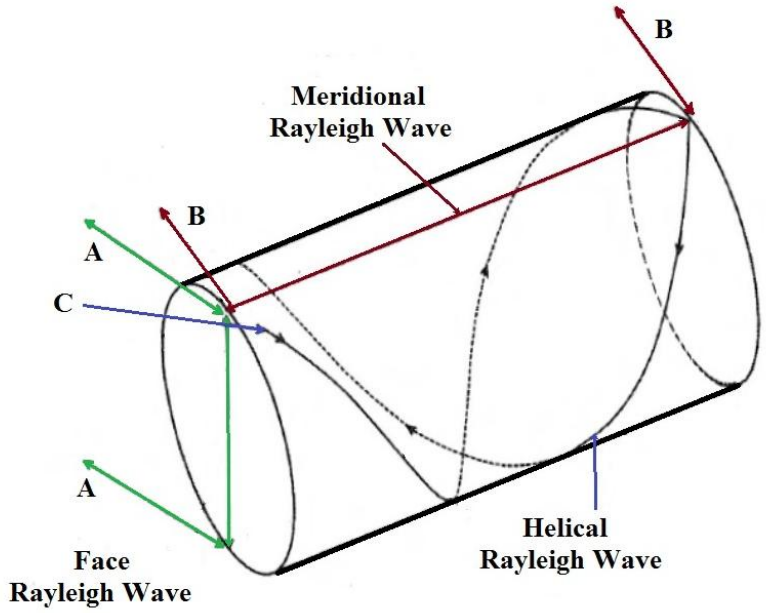

Figure 3.8: Sketch of the three types of Rayleigh wave coupling with a solid elastic cylinder: (A) the face crossing waves, (B) the meridional wave, and (C) helical wave wrapping around the cylinder. Note this wave will propagate around the circumference of the cylinder when the impinging wave is broadside.

cylinder results in scattering only from its edges (only broadside and end on source-receiver configurations return a significant specular echo). Therefore, the acoustic scattering pattern from the specular reflection able to be measured from a cylinder is limited broadside monostatic configurations unless a bistatic receiver is used as shown in Fig. 1.2.

Additional complexity is found when investigating the elastic response of the cylinder, due to the single axis of symmetry. However, for this shape a comparison to the results found in literature reveals the waves on the cylinder can be represented by a form function similar structure to the form function of the spherical shell (Eq. (19)) that causes the unique time-frequency behavior [7, 26, 97, 57]. For the solid cylinder however, the MFE does not exist rather other types of surface guided waves exist. These surface waves do not have the same behavior as the Lamb waves responsible

for the MFE, but they do offer a similar benefit to the classification based on the behavior and existence of such guided waves. From this similarity, the same analysis presented for the sphere can be applied to the cylinder, in future research. For the case of a solid elastic cylinder, the energetic waves guided around the object are Rayleigh waves and similar time-frequency techniques and detection tools developed in this research will apply. To briefly introduce the paths of these Rayleigh waves, we can look at the geometry of the cylinder and how these couple with the cylinder. These types are described in the literature as meridional, helical, and face crossing. Fig. 3.8 presents a schematic of how these rays propagate around the cylinder in three dimensions. Each wave only couples to an excitation wave when the wave incidents on the cylinder at a coupling angle (θ_r) [7]. This coupling angle limits the directions the guided waves can be excited and detected, and as such, the behavior is similar to glint angles from flat surfaces on targets. Similar to the excitation of the A_0 Lamb waves on the sphere, this coupling angle is determined by the ratio of the outer medium sound speed (c_0) to the phase speed (c_{ph}) of the wave (i.e. $\theta_r = sin^{-1}(\frac{c_0}{c_{ph}})$).

The geometry and guided wave mechanisms makes off axis numerical methods complex, and from the findings of the spherical shell, the behavior of these waves could be approximated using ray paths and the cylinder form function [57]. The broadside return can be computed from the Goodman and Stern Formulation by assuming an infinite cylinder. This research will leave the matter for suggested future work to develop a more complete model to account for expected frequency shifts at any given source and receiver combination for the cylinder. And the limited nature of the excitation of these waves will be a source of difficulty in using these waves for detection, as will be presented in chapter IV.

3.5 Application to Time-Frequency Beamforming

The time vs. angle representation displayed in Fig. 3.1 shows that the MFE persists for bistatic source-receiver configurations and, thus, still carries information about the physical features of the elastic shell. However, the bistatic amplitude of the A_0 wave arrival is significantly reduced compared to the monostatic configuration. Therefore, bistatic detection of the MFE would need to be enhanced for practical implementations, by coherently combining the signals measured on an array of receivers using beamforming techniques [89]. To do so, it is necessary to use a generalized time-frequency beamformer to account for the time-frequency shifts occurring between the various bistatic MFE echoes recorded on an array of sensors surrounding the spherical shell. This generalized time-frequency beamformer can be implemented using a similar formalism developed for compensating wideband Doppler effects when tracking a fast moving acoustic source based on companded or time-scaled replica of the Doppler-free source signal [94]. The term "companded" is a portmanteau of *comp*ressed and ex*panded*. It is assumed hereafter that the bistatic A_{0^-} arrival recorded at a bistatic angle θ_j is centered at time t_j and frequency f_j in the time-frequency plane. Additionally, the scattered time-domain signal recorded by the j^{th} receiver located at a bistatic angle θ_j is noted $P_j(t)$ $(j = 1..N)$. A generalized time-frequency beamformer $B(t; N)$ can then be defined by combining companded versions of the N receiver signals $P_j(t)$ such that:

$$B(t; N) = \sum_{j=0}^{N} P_j(\gamma_j(t + \tau_j)) \tag{22}$$

where the parameter $\tau_j = t_j - t_1$ is selected to compensate the apparent bistatic time-shift (e.g. see Fig. 3.5) of the A_{0^-} wave, defined here with respect to the bistatic arrival time of the A_{0^-} wave recorded on the first receiver. Similarly, the companding (or time-scaling) parameter $\gamma_j = 1 + (f_j - f_1)/f_1$ is selected to compensate for the

apparent bistatic frequency-shift the A_{0-} wave (e.g. see Fig. 3.7). The values of the parameters τ_j and γ_j can be estimated based on predictions from the quantitative ray analysis (as described in Section 3.3) or by directly measuring the time-frequency shifts of the bistatic A_{0-} arrival from SPWV analysis (as described in Section 3.2), the latter being the selected approach hereafter. It can be noted that when $\gamma_j = 1$ (i.e. in the absence of frequency-shift), the expression of the generalized time-frequency beamformer shown in Eq. (22) reduces to the expression of the conventional time-delay beamformer [89, 94].

This study focuses on the first MFE arrival since it is the most energetic echo. The subsequent counter-clockwise mid-frequency enhancement wave packets that occur later are much weaker (see Fig. 3.1) and thus likely more difficult to measure in practice.

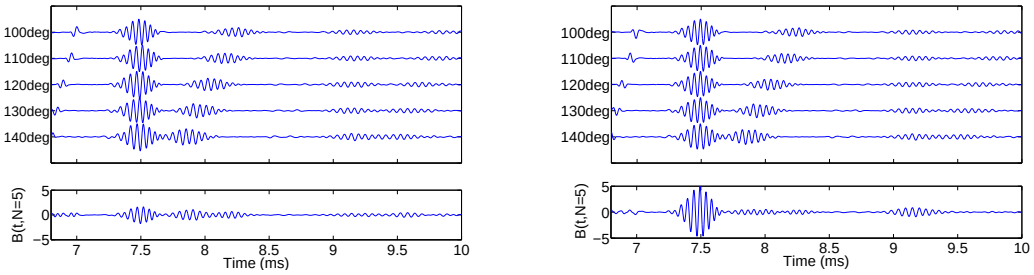

Figure 3.9: (a) Upper Panel: Stacked representation of the time-aligned arrivals of counter-clockwise propagating A_{0-} waves (see Fig. 3.1) recorded at five different bistatic angles. The relative bistatic time-shifts, with respect to first bistatic angle $\theta_1 = 100°$, were obtained from the SPWV analysis (see Fig. 3.5). Lower Panel: Coherent addition of the five time-shifted waveforms using a conventional time-delay beamformer (computed by when setting the companding parameter as $\gamma_j = 1$ see Eq. (22)). (b) Upper Panel: same as (a), but each waveform was also companded to account for the apparent frequency shift of the bistatic counter-clockwise propagating A_{0-} arrival-with respect to the first bistatic angle $\theta = 100°$- based on the measured frequency-shifts values from the SPWV analysis (see Fig. 3.7). Lower Panel: Coherent addition of the five time-frequency shifted waveforms using a generalized time-frequency beamformer (see Eq. (22)). Note that each bistatic waveform, in both upper panels, was normalized to its maximum value, such that one would expect a maximum beamformer output of 5 when an optimal coherent addition of these waveforms is achieved.

As an illustration of the proposed array beamforming methodology, the upper panel of Fig. 3.9a displays the A_{0^-} arrivals recorded by five bistatic sensors uniformly distributed in azimuth around the spherical shell between $100^\circ \leq \theta \leq 140^\circ$. The analysis window was limited to the first A_{0^-} echo. These A_{0^-} arrivals were simply time-aligned with respect to the counter-clockwise MFE arrival for the first receiver (j=1, $\theta_1 = 100^\circ$). It can be noted that the shape of the waveforms remain slightly different due to the bistatic frequency-shift of the A_{0^-} wave. Additionally, the maximum amplitude of each receiver signal $P_j(t)$ was normalized to unity, to account for the bistatic amplitude variations of the A_{0^-} arrival (see Fig. 3.1) so that each receiver had an equal contribution to the beamforming summation in Eq. (22). These five time-aligned and normalized waveforms were then simply summed to generate the output of the conventional time-delay beamformer (i.e. using Eq. (22) with N=5 and $\gamma_j = 1$), as shown on the lower panel of Fig. 3.9a. The maximum of this conventional time-delay beamformer signal is only 1.63 (i.e. < 5), which indicates that the five received signals were not coherently added in an optimal fashion. On the other hand, the upper panel in Fig. 3.9b displays the A_{0^-} arrival for the same five receivers, but after applying both time shift and frequency shift corrections to each waveform based on the measured values from respectively Fig. 3.5 and Fig. 3.7 for the counter-clockwise A_{0^-} echo. The lower panel of Fig. 3.9b shows that the maximum of the generalized time-frequency beamformer, computed using Eq. (22), is equal to 4.98 and thus close to the optimal value of 5. Hence this value indicates that the five received signals were indeed coherently added in an near optimal fashion using the generalized time-frequency beamformer (see Eq. (22)).

The influence of the receiver array aperture or the number N of bistatic receivers on the performance of the generalized time-frequency beamformer (see Eq. (22)) is investigated next. Fig. 3.10 displays the layout of the bistatic receivers around the

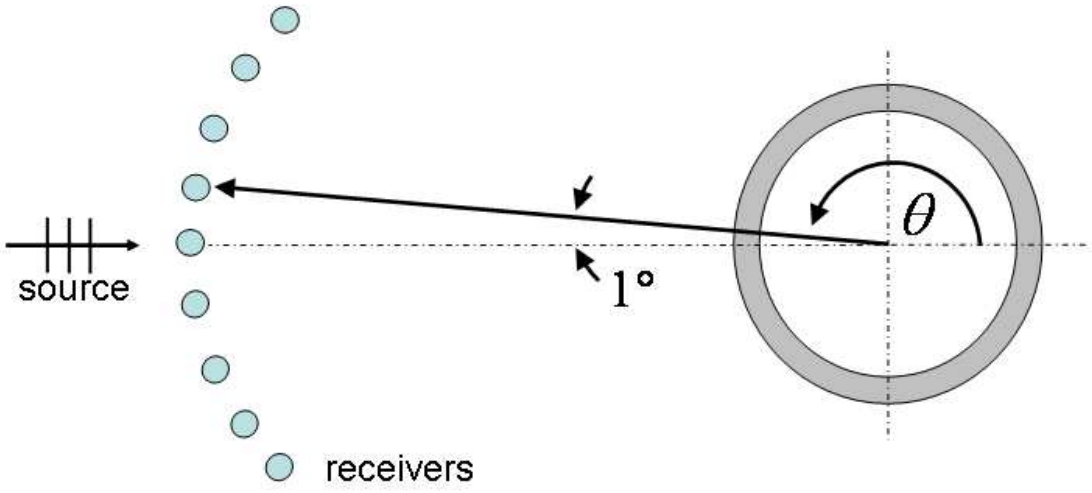

Figure 3.10: Schematic of the bistatic receivers layout around the spherical shell used for the numerical simulations (see Fig. 3.11). Each receiver array is centered on the monostatic direction-$\theta = 180°$-and is composed of an odd number N of receivers, which are uniformly spaced in azimuth 1° apart.

spherical shell, which are centered on the monostatic direction $\theta = 180°$. These receivers are uniformly spaced in azimuth 1° apart, which implies a relative shift of the center frequency of the counter-clockwise A_{0^-} echo of approximately 250 Hz between two consecutive receivers based on the results displayed in Fig. 3.7. Fig. 3.11 displays the variations of the maximum value of the generalized time-frequency beamformer $B(t; N)$ (dot symbols) for an increasing number of receivers N (i.e. corresponding to an increasing azimuthal aperture of the receiver array). Similarly, to the results shown in Fig. 3.9b, each counter-clockwise A_{0^-} arrival was also companded to account for the apparent frequency shift between bistatic receivers. As expected, the maximum value of the generalized time-frequency beamformer $B(t; N)$ linearly increases with the number of receivers (up to $N = 19$ here), thus indicating that all

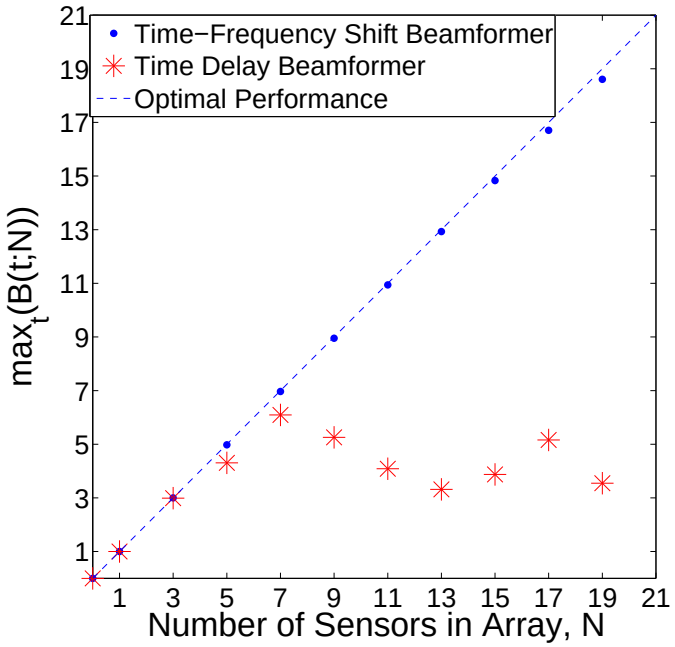

Figure 3.11: Evolution of the maximum value of the array beamformer $B(t;N)$ (see Eq. (22)) for an increasing number of receiver N (equivalent here to an increasing angular aperture of the receiver array see Fig. (3.10)). Asterisk and dot symbols mark, respectively, the values obtained by the conventional time-delay beamformer formulation when the companding (or time-scaling) parameter is set to $\gamma_j = 1$ or the generalized time-frequency beamformer formulation. The linear dependency of the number of N of receiver (dashed line) is also added for comparison and corresponds to the optimal achievable value of the array beamformer output $B(t;N)$ when the arrivals of counter-clockwise propagating A_{0^-} waves recorded by the N receivers add in phase coherently.

counter-clockwise A_{0^-} arrivals were indeed coherently processed across the array aperture. For comparison the maximum value of the conventional time-delay beamformer (star symbols) are also displayed on Fig. 3.11. It can be observed that those values start to significantly deviate from the optimal linear increase beyond $N = 5$ receivers. These numerical results thus confirm that conventional time-delay beamformer would not be an optimal way to coherently process MFE arrivals recorded across a bistatic aperture.

Practical implementation of this type of processing may be limited, as the method

requires prior knowledge of the time-frequency behavior for a given target. An alternate approach would be to use a library of models for searching for a time-frequency behavior and to maximize the output of the beamformer, and thus when a maximum is found the corresponding model could be used to classify the target. Additionally, it is important to consider the approach here uses a circular aperture as opposed to the traditional linear aperture, which would require compensation for spreading and attenuation losses along an array to maintain maximum array output.

3.6 Discussion and Summary

The bistatic acoustic scattering of a fluid-loaded spherical elastic shell was investigated both numerically, using a partial wave series expansion, and theoretically using a quantitative ray analysis. This study focused on the most energetic bistatic echoes also referred to as mid-frequency enhancement echoes, or MFE, which are associated with the circumnavigating first antisymmetric guided wave (primarily its A_{0^-} modal component). In particular, the time-frequency analysis of the MFE was conducted using the Smooth Pseudo Wigner-Ville transform.

Overall, the results of this study demonstrated that time-frequency variations of the bistatic echoes associated with the structural response of elastic spherical shell can be predicted. Additionally, due to the apparent bistatic time-frequency shifts of these MFE echoes, optimal coherent processing of those weak MFE echoes cannot be achieved by conventional array processing techniques simply relying on variants of the time-delay beamformer algorithm. In particular, these results imply that conventional Synthetic Aperture SONAR (SAS) algorithms may not yield optimal imaging results for the detection and classification of the MFE echoes of spherical elastic shells insonified by low-frequency bistatic SONAR systems. Similar conclusions may be applicable to elastic shells with other canonical shapes supporting propagating guided waves (such as finite cylinders). Further joint theoretical and numerical analysis, as

well as experiments, are required to further understand the mechanisms of bistatic echo formation for elastic shells and the time-frequency coherence of structure-borne acoustic echoes. Such studies should provide valuable insights to guide the design of optimal receiver architecture for low-frequency bistatic SONAR systems (e.g. using distributed sensor networks) and SAS imaging algorithms.

The following three contributions can be drawn from this chapter:

1. The bistatic MFE echoes were found to exhibit a time-shift and frequency-shift, as well as a decrease in amplitude, with respect to the monostatic receiver configuration. This behavior is a relevant finding and has not been previously published.

2. A simple quantitative ray theory can be used to understand and predict these observed time-frequency shifts of the MFE arrival. The shifts primarily result from the combined effect of 1) the bistatic variations of the path length around the spherical shell of the clockwise or counter-clockwise circumnavigating A_{0-} waves, and 2) the frequency dependence of the radiation damping parameter for the A_{0-} wave.

3. A generalized time-frequency beamformer can be used for coherent processing the bistatic MFE echoes recorded along a distributed receiver array around the spherical shell. Using companded replica of the bistatic MFE echoes to account for a known time-frequency shift of the MFE arrival between receivers. This beamformer can be used in combination with the qualitative ray model to create a library of time-frequency behavior for classification.

CHAPTER IV

ACOUSTIC IMAGING OF SIMPLE ELASTIC TARGETS: SPHERICAL SHELL AND SOLID CYLINDER

4.1 Motivation

The development of robust methodologies allowing for the concurrent detection, classification, and localization of underwater targets is a challenging problem with high operational importance for mine countermeasure activities (MCM). To this end, acoustical imaging offers an attractive approach, especially when visibility is limited, a large standoff distance is required, or if the target is buried in the bottom sediments [83, 60]. A straightforward approach for acoustical imaging of specular echoes from rigid targets consists of beamforming (or back-propagating) the acoustic backscatter signals recorded on a receiver array back to a selected imaging plane by assuming free-space propagation in a stationary and homogeneous medium [72]. This approach is commonly used in underwater SONAR systems and medical ultrasound scanners. This beamforming-based technique has been applied to image large targets (with respect to the characteristic acoustic wavelength of the imaging system) using the so-called "distributed bright-spot model" [4] which consists of assuming that the target echo results from a number of range-distributed point scatterers along the actual target's contour. The spatial resolution of this imaging technique primarily increases with the selected frequency band and the aperture of the receiver array [8]. For instance, high-frequency (f∼MHz) SONAR systems using a large synthetic aperture created by towing a single receiver- commonly referred to as Synthetic Aperture

[0]Part of this work was submitted July 2012 for publication in IEEE Journal of Oceanic Engineering.

SONAR (SAS) processing [32]-can potentially provide photography-like images of the seafloor with up to millimetric resolution. However, these conventional high-frequency SONAR systems cannot image buried targets (due to the limited penetration of the high-frequency acoustic energy into the sediments [41]), nor produce significantly different acoustic images of a man-made elastic shell (i.e. potentially containing hazardous explosives) from a solid object (e.g. mine decoy) of similar outer shapes (see Section 1.5.4).

To address these limitations of high-frequency SONAR systems, low-frequency (f∼kHz) SONAR systems have been developed to enhance the detection of buried targets as well as the recognition of mine-like elastic targets by exciting their structural responses (or resonance signatures) [50, 67, 52]. In this "structural acoustic regime" of frequencies, the target's elastic response includes both specular echoes as well as structural echoes, such as guided waves circumnavigating a thin shell [73]. This elastic response has been suggested as a basis for target classification through acoustic "finger printing" using time-frequency analysis or acoustic color representation [97, 50]. In parallel, previous studies have attempted to image these elastic echoes (also referred to as structural echoes) using the aforementioned free-space back-propagation algorithm (such as SAS processing), [52, 97, 58] although this algorithm was originally designed for imaging specular echoes of rigid targets based on the so-called "distributed bright-spot"' model. However, due to their specific generation mechanisms, the elastic echoes of the elastic target can have a complex radiation pattern, causing the corresponding backscatter wavefronts to have different time-delay laws and frequency content than the backscatter wavefronts associated with specular echoes[48]. Thus, when compared to the specular echoes, these elastic echoes typically appear defocused away from the actual target's location on acoustic images generated using the same standard free-space back-propagation algorithm. This apparent defocusing on conventional acoustic images occurs as a single time-delay law-based on point scatter's radiation only- is

applied for each pixel of the selected imaging plane. This defocusing is especially detrimental for target recognition purposes when one attempts to image the spatial origin of weak elastic echoes (compared to usually more energetic specular echoes) in the presence of ambient noise, reverberation, and clutter.

As an alternative to these standard acoustical imaging techniques, the acoustic holography technique has been suggested as a means for analyzing and visualizing structural echoes from elastic targets [7]. However, its implementation is not straightforward for a receiver array with complex geometry such as a two-dimensional synthetic aperture array with non-uniform spacing produced by imperfect positioning of the moving sensor platform. One potential improvement for acoustical imaging of elastic targets would be to include in the back-propagation algorithms a more accurate model of the target's elastic response, as obtained from quantitative ray theory [55] or the generalized target description model [4, 23], to account for the specific features of structural echoes. This would allow enhancement of the refocusing for both the specular and structural echoes to their actual spatial origin akin to time-reversal experiments in the presence of elastic targets [68]. However this potential improvement would add significant computational complexity to the back-propagation algorithm as it would become target-dependent, thus requiring in practice a search over the various parameters of a (large) database of known target models (e.g. target's dimensions, shell thickness etc...) when attempting to image unknown targets. Indeed, this potentially enhanced imaging resolution obtained at the cost of increased computational complexity is akin to what one encounters when using matched-field processing algorithms [41] instead of simple time-delay free-space beamforming for acoustic source localization.

The main objective of this chapter is to demonstrate that the same simple free-space beamforming algorithm can actually be used to image the full evolution of the spatio-temporal refocusing of both specular and elastic echoes by varying the

time-delay law applied to each pixel of the selected imaging plane. This implementation has the advantage of using the same simple free-space beamforming algorithm used to generate conventional acoustic images. Furthermore, it allows to partially account for the delayed arrivals of elastic echoes with respect to specular echoes in order to enhance the refocusing of these elastic echoes onto the actual target's location. in practice, this enhanced focusing ultimately may produce acoustic images with higher signal-to-noise ratio for target detection purposes. The proposed approach is illustrated using time-domain free-space back-propagation as it allows for arbitrary receiver configuration (e.g. randomly spaced array) without requiring data interpolation necessary for other implementations of the standard back-propagation algorithms relying on frequency-wavenumber transforms [32, 37, 36]. Furthermore, this approach is especially efficient when a large angular aperture of the receiver array, for instance surrounding the target of interest as used by circular SAS systems [60, 27, 61]. Imaging results are presented for canonical elastic targets (thin spherical shell and rigid cylinder) whose acoustic responses are well characterized in the previous literature [97, 5] using both numerical simulations and experimental data. The influence of the receiver aperture and radiation pattern of the target echoes on the imaging resolution is also discussed.

This chapter is divided into five sections. The following section reviews and formulates the free-space beamforming method used in acoustic imaging. Section 4.3 formulates the modified free-space beamforming algorithm in the time-domain for imaging elastic targets. The proposed imaging approach is illustrated based on numerical simulations of the monostatic and bistatic response of a thin spherical shell in the structural acoustic regime of frequencies. Section 4.4 presents experimental results using the low-frequency elastic response of the same thin spherical steel shell as well as a solid aluminum cylinder both laying proud on a sandy bottom. Finally, Section 5.7 summarizes the findings and contributions from this imaging study.

4.2 Acoustic Imaging Fundamentals

This section is designed to give a brief overview of acoustic imaging principles and in particular Synthetic Aperture SONAR (SAS). This section assumes the reader is familiar with SONAR and acoustic propagation but not necessarily conventional acoustic imaging techniques. A review of SONAR imaging by means of the back-propagation method will be described by an overview of the signal processing method.

The main difference between traditional array processing and synthetic aperture is the construction of the data set from either a physical array or a series of successive recordings at various positions to create a synthetic array along the path of travel. To construct a synthetic aperture data set, it is required that the environment being observed does not change between successive positions. This assumption allows the data to be processed as if it were collected at the same instance as if on a single physical array. Advantages of the SAS data collection allow arbitrary array configurations and greater resolution capabilities with a limited physical array size. There are however some drawbacks to this approach, as it does require data to be collected and processed after the required positions are recorded (i.e. cannot process the image without sufficient aperture data). Furthermore, the arbitrary array configuration can require data interpolation for computationally efficient imaging techniques that require equal spacing of data, and this requires accurate positioning for each location measured. The remainder of this section is applicable to image processing from physical or synthetic arrays, therefore no distinction between the two will be made unless necessary.

Traditionally SONAR uses broadband frequency modulated pulses, sometimes referred to as pings or chirps. Virtually all SAS systems, use broadband transmitted signals where the signal bandwidth is determined by the required resolution. This broadband pulse can then be pulse compressed via Matched Filtering (which, simply put, is the cross-correlation of the received signal with the source signal). The image

plane can be described along two perpendicular axes, down range and cross range, where the latter is parallel with the array path (see Fig. 4.1). This image plane can then be separated into pixels with the size determined by the resolution limits of the system parameters.

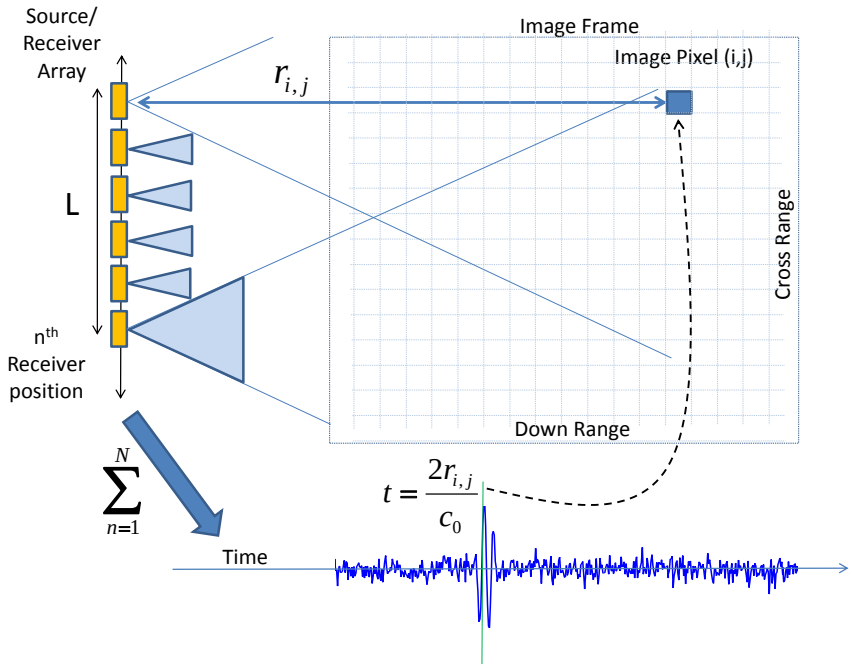

Figure 4.1: Schematic of Line Array Setup and Process for Imaging.

The cross range resolution of a SONAR system is dependent on the ratio between the acoustic wavelength (sound speed divided by frequency , $\lambda = \frac{c_0}{f}$), and the length of the array, L. These parameters determine the array beam width and in turn determine cross-range resolution. Therefore, λ/L reveals that a longer array or higher frequency will increase the cross range resolution. However; higher frequency systems limit the achievable propagation down range due to increased absorption, and do not allow for bottom penetration. Therefore the SAS approach allows the length to be extended indefinitely by collecting data from several consecutive pings to form a longer array. The theoretical cross-range resolution in SAS is half the length between each element in the receive array, at all ranges based on beam width. A practical limitation of

SAS occurs due to source/receiver directivity, which limits the sound propagation to limited angles shown as the cones emitting from the array schematic in Fig. 4.1. The direction dependent sensitivity of the source or receivers can be taken into account. This amplitude factor can also be used to control the side lobe suppression versus the angular resolution [89]. The down range resolution is independent of range and determined by the compressed pulse width (in time) which is directly related to the bandwidth of the signal. Therefore the pulse width and down range resolution can be determine from $c_0/2BW$ where BW is the bandwidth in Hz.

A simple schematic to aid the description of the imaging method is shown in Fig. 4.1. The N-element array depicted on the left records signals at each nth receiver position. From here the signals are match filtered (pulse compressed). Then beamforming is applied to focus the array output for a given pixel (i, j). Beamforming is well covered in the literature [42, 13, 66]. The simplest and most intuitive type of beamforming is equally weighted time-domain beamforming by back-projection. This is done by back propagating the received signal via each pixel. Back propagation is also known as Delay-And-Sum beamforming ([41], [42] pg. 117-119). Formally, back-propagation is straightforward and can be applied by summing the time delayed signal across the array explicitly given by the equation:

$$B_{i,j}(t) = \sum_{1}^{N} s_n(t - \frac{2r^n_{i,j}}{c_0}) \tag{23}$$

where c_0 is the sound-speed of the surrounding medium and $r^n_{i,j}$ is the distance between the n^{th} receiver and the center of the imaging pixel (i, j). By convention, for the case of a point target, the refocused acoustic amplitude recorded by the N receiver elements is concentrated on the pixel's location at a delay $t = \frac{2r_{i,j}}{c_0}$. The expected arrival time accounts for the time for the pulse to travel to and from the selected pixel. Then the energy recorded around this time can be mapped to that pixel on the image. This progression is repeated for all pixels to form the acoustic image. The

method can be extended to the three dimensional case by using appropriate array configuration to capture the full field and beamforming to account for the three-dimensional propagation. When a reflective object is present the amplitude of the return is fairly high, and when there is no object the bottom typically returns the bottom scattering which appears as speckle in the imaging (see Fig. 1.4).

Practical implementation to the acoustic imaging approach requires accurate positioning of the location of the source and receiver for sharp images. The amount of positioning error is dependent on the required image quality. The sonar has to be positioned with accuracy better than a fraction of a wavelength along the entire aperture to obtain the theoretical resolution limits (at 100 kHz this is approximately 1 mm). This can become exceedingly difficult with moving AUV platforms, and requires further processing for determining micro-navigation and receiver locations. Current methods for micronavigation are based on the principle of displaced phase center antenna (DPCA) in combination with inertial navigation systems to estimate the platform motion.

Furthermore acoustic imaging is near-field processing and requires the sound velocity to be accurately estimated for a focused imaging to be formed. The sound velocity in the ocean varies with depth, and can also contain local horizontal and temporal variations[34]. One possible approach is to correct for incorrect sound velocity and positioning is use of an auto-focus technique to maximize the sharpness of any image within set ranges. If the SONAR platform is in motion as in SAS applications, the Doppler effect can cause defocussing of the ambiguity function and requires some form of Doppler compensation. Doppler tolerant pulses can be used to negate this spreading after Matched Filtering occurs [3]. These limitations for implementation described above are outweighed by the benefits of acoustic imaging results and thus it is still widely used for detection purposes.

It is of use to note that the expected arrival time can be selected at various times to

form a time evolving back propagation movie of the image plane, in order to observe the scattered field behavior as is propagates. This movie contains the entire scattered field information and can be extremely useful when analyzing the formation of echoes from an elastic target. The following section will expand on the basic imaging to introduce the method of forming this movie and propose a method to handle the elastic echoes that arrive later than this expected arrival time.

4.3 Spatio-Temporal Visualization of the Acoustic Response of an Elastic Target Using Free-Space Back-Propagation

4.3.1 Acoustic imaging using free-space back-propagation

For simplicity, the two-dimensional configuration is used in this study, as depicted in Fig. 4.2. Assuming free-space back-propagation between the target and the nth receiver element (n=1,2,..N), the backscattered waveforms recorded by each receiver, noted here $s_n(t)$ can be back-propagated toward a given pixel (i, j) of the two-dimensional imaging grid using the following beamformer formulation in Eq. (23).

Furthermore, to account for the finite temporal resolution of the SONAR system (typically limited by the frequency bandwidth of the recorded waveforms), the value of each pixel i, j on the acoustic images is set equal to the integral of the envelope (defined here as the magnitude square of the Hilbert's transform) of the beamformer output $B_{i,j}(t)$:

$$C_{i,j}(\alpha) = \int_{\alpha-\Delta}^{\alpha+\Delta} abs(Hilbert(B_{i,j}(t)))^2 dt \tag{24}$$

where the parameters 2Δ and α denote the length and center time delay of the integration window. The spatio-temporal refocusing of the backscattered waveforms (referred to hereafter as "back-propagated movie") can then be visualized by displaying successive snapshots (or frames) of the amplitude variations of the integrated

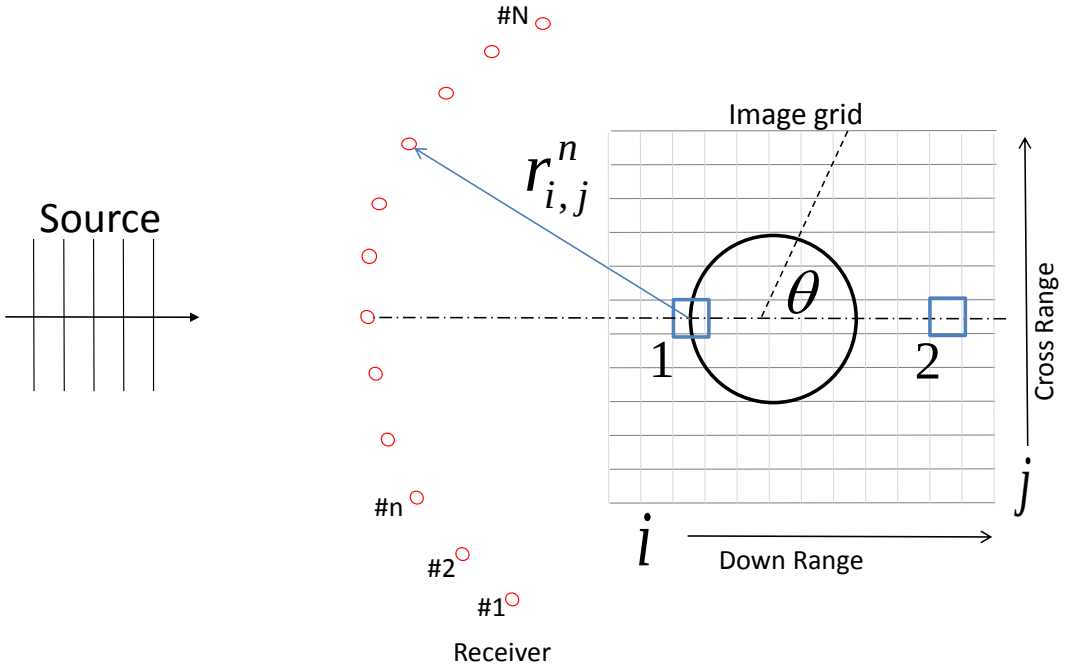

Figure 4.2: Schematic of the two-dimensional configuration for the source, receivers, and target. The azimuthal angle for the spherical shell's backscatter is indicated as $\theta = 180°$ ($\theta = 0$ for forward scattering). The distance between pixel (i,j) and the n^{th} receiver is denoted $r_{i,j}^{n}$ $(n = 1, 2, ..., N)$.

beamformer amplitudes $C_{i,j}(\alpha)$ across the imaging area by varying the center time-delay α (e.g. see Fig. 4.5 and Fig. 4.6). However, standard acoustical imaging of targets, based on the distributed bright-spot model, typically only display the values of $C_{i,j}(\alpha = 0)$ over the imaging grid, i.e. at the center time-delay $\alpha = 0$. Yet this value of $\alpha = 0$ may not be the optimal one to maximize the refocused amplitude of the backscattered waveforms, especially when considering elastic targets. This limitation is illustrated next using numerical simulations of the acoustic backscatter generated by a 1.06 m diameter thin elastic spherical shell (thickness of 13.25 mm) excited in the structural acoustic regime of frequencies (100 Hz$< f <$45 kHz). Details of the numerical simulation are given in Chapter II and the shell's parameters are listed in

Table 1.

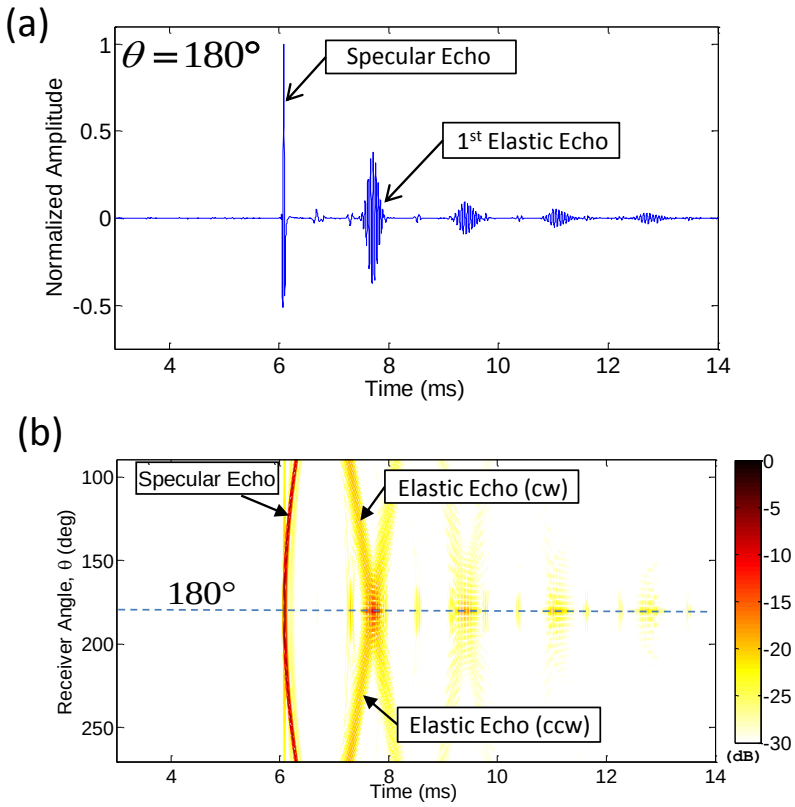

Figure 4.3: Simulated backscatter response of a thin spherical shell (filtered in the frequency band [100 Hz-45 kHz]). (a) Monostatic response ($\theta = 180°$) The first elastic echo corresponds to the antisymmetric A_0 guided wave circumnavigating the shell. (b) Variations of the shell's bistatic response vs azimuthal angle θ of the receiver (See Fig. 4.2). The specular and first elastic echoes (propagating either clockwise (cw) or counter-clockwise (ccw) around the shell are also indicated). Subsequent arrivals correspond to surface guide waves undergoing multiple revolutions around the spherical shell. All displayed values were normalized by the maximum value of the specular echo for $\theta = 180°$.

4.3.2 Acoustic imaging of the monostatic response of a thin spherical shell

Fig. 4.3a displays the simulated monostatic response (i.e. where the source and receiver's azimuth angles are equal) of the spherical shell. The scattered field in this structural acoustic regime of frequencies contains both a broadband specular echo (centered here at t=6.1 ms) followed by more narrowband elastic echoes which

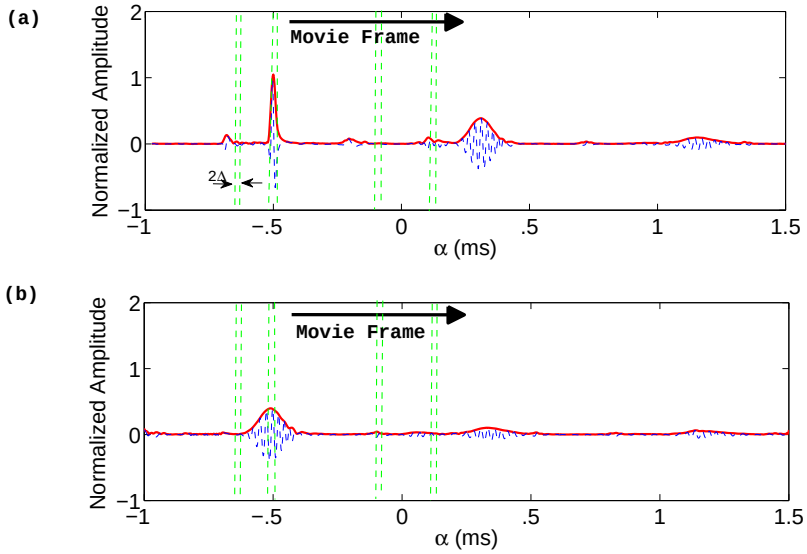

Figure 4.4: Beamformer waveform (dashed line, see Eq. (23)) and its envelope (solid line) obtained when focusing the monostatic response of the spherical shell on either (a) Pixel 1, located at the shell surface or (b) Pixel 2 located behind the shell (as marked on Fig. 4.2). The vertical lines indicate for different focus window-all of width $2\Delta = 0.07$ ms- centered respectively on delay times $\alpha = -0.3, 0, 0.8, 1.25$ ms, which correspond to four frames of the back-propagation movie shown in Fig. 4. The receivers cover a 180° circular aperture and are equally spaced 1° apart.

correspond to antisymmetric Lamb-type waves circumnavigating the shell, and subsequent revolutions of the same. The first and most energetic elastic echo (centered here at t=7.7 ms) is of primary interest for target detection and classification[48, 5]. Due to the axisymmetry of the spherical shell, $N = 180$ replicas of this monostatic response are used to mimic the received signals collected by a monostatic source-receiver SONAR system circling around the elastic shell (see Fig. 4.2) at a range of 10 m with respect to the sphere's center. The successive source-receiver's positions have an equal angular spacing of 1° and cover a 180° circular aperture (i.e. ranging from θ =90° to θ =270°). Using these N received monostatic waveforms, Fig. 4.4 displays the output of the free-space beamformer output $B_{i,j}$ (see dashed line in Fig. 4.4) and its envelope (solid line) for two selected pixels: pixel 1 is located close to the shell's surface and faces the receiver array while pixel 2 is located behind the shell's

surface opposite to the receiver array (as indicated on Fig. 4.2). The shell center is located at a cross-range of 0 m and down-range of 10 m on the imaging grid. This geometry mimics the experimental set-up used in Section III. Conventional acoustic imaging (e.g. SAS-like imaging) displays the integrated value of the beamformer envelope $C_{i,j}(\alpha)$ (using Δ= 0.035 ms here) for the time-delay α = 0 ms (see Fig. 4.5b).

As expected Fig. 4.5b shows that the specular echo is focused along the shell's wall. But the first elastic echo is not tightly focused and is imaged behind shell at down-ranges larger than 11 m-thus spreading in part over pixel 2, as revealed also by inspecting the beamformed waveforms displayed on Fig. 4.4. Fig. 4.5a-d displays the integrated beamformer output $C_{i,j}(\alpha)$ for three other time-delays α=-0.3 ms, 0.8 ms, and 1.25 ms (as marked by vertical lines on Fig. 4.4). Overall, these four successive frames of the back-propagated movie (see Fig. 4.5a-d) show the spatio-temporal refocusing (resp. diverging) of the wavefronts associated with the specular and first elastic echo onto (resp. away from) the spherical shell's center occur at different delays α. To ease comparison, the logarithmic values of $C_{i,j}(\alpha)$ displayed in each of the four frame were all normalized to the maximum value of $C_{i,j}(\alpha = 0$ ms) over the imaging grid (i.e. as shown on Fig. 4.5b).

Fig. 4.5b confirms that the conventional acoustic image obtained for α = 0 ms allows one to image the shell's outer wall using the specular echo (with a reference amplitude set here to 0dB). But the same specular echo was actually tightly focused on the shell center for an earlier time delay α=-0.3 ms, thus having a significantly higher amplitude of +15dB (see Fig. 4.5a). Furthermore, on the conventional acoustic image shown in Fig. 4.5b the elastic echoes are imaged as a separate low-amplitude feature (with a value -15.2 dB compared to the specular echo's amplitude) located more than one meter behind the shell. Thus this elastic feature could be misrepresented as a secondary target or might not be visible at all on this image if the ambient

noise or clutter levels were to be too high in practice. On the other hand, using a later time-delay α=1.25 ms, brings the same elastic echo into focus at the shell's center, thus now appearing as an energetic feature with a +6 dB amplitude (see Fig. 4.5d) which could provide a significant signal-to-noise ratio advantage for detection purposes. As mentioned in the introductory section, this elastic echo could be used to help discriminate between a man-made object and a simple rock of similar dimension (i.e. with no characteristic elastic return). Fig. 4.5a-d also shows the entire recorded backscatter data actually emanate from the same location at a down range of 10 m and not from two different targets. Consequently, these results indicate that the conventional acoustic image shown on Fig. 4.5b only provides an incomplete representation of the full spatio-temporal refocusing of the elastic response of the spherical shell contained in the backpropagation movie when the time-delay α varies as shown on Fig. 4.5a-d. Thus tracking the spatio-temporal evolution of selected energetic features from the backpropagation movie, simply obtained by varying the parameter α in Eq. (24) (as shown on Fig. 4.5a-d), could potentially be used to develop robust methods to image and detect elastic objects with little added computational effort over what's required to obtain the conventional acoustic image (i.e. $\alpha = 0$ only here).

One alternative to visualizing or analyzing multiple frames of the back propagating movie, could simply be to generate a single acoustic image where the value $D_{i,j}$ at each pixel is set to the maximum value of the integrated beamformer output $C_{i,j}(\alpha)$ (see Eq. (24)) over a selected interval of time-delay α i.e. such that

$$D_{i,j} = \max_{\alpha}(C_{i,j}(\alpha)) \tag{25}$$

This maximum search method (MSM) allows one to simply visualize where each received wavefront (or backscatter's feature) focuses with maximal amplitude in the imaging plane. But this MSM requires in effect to first separate each received wavefront in the received backscattered data, for instance by directly time-windowing out the specular echo or first elastic echo from the received data. Otherwise, the

MSM would simply represent the stronger of the two signal components (i.e. here the broadband specular echo) and ignore the weaker one (i.e. here the narrowband elastic echo). Fig. 4.5e and Fig. 4.5f display the images obtained with the MSM after selecting respectively the specular or first elastic wavefront from the received mono-static data. As expected, both MSM images show a tight focus of both wavefronts on the elastic shell's center -thus confirming that both echoes are generated by the same elastic target instead of two closely spaced targets. This occurs at the center of the sphere due to the spherical spreading, and would only be expected to occur as such for similar objects or point scatterers (such as corners or edges of a target). The amplitude of the specular increases by +15.4 dB by the tight focus of energy produced by the MSM image. Furthermore, the amplitude of the refocused elastic echo at the center of the MSM image is +6.9dB as opposed to the low-amplitude (-15.2 dB) and defocused elastic wavefront displayed on the conventional acoustic image (see Fig. 4.5b).

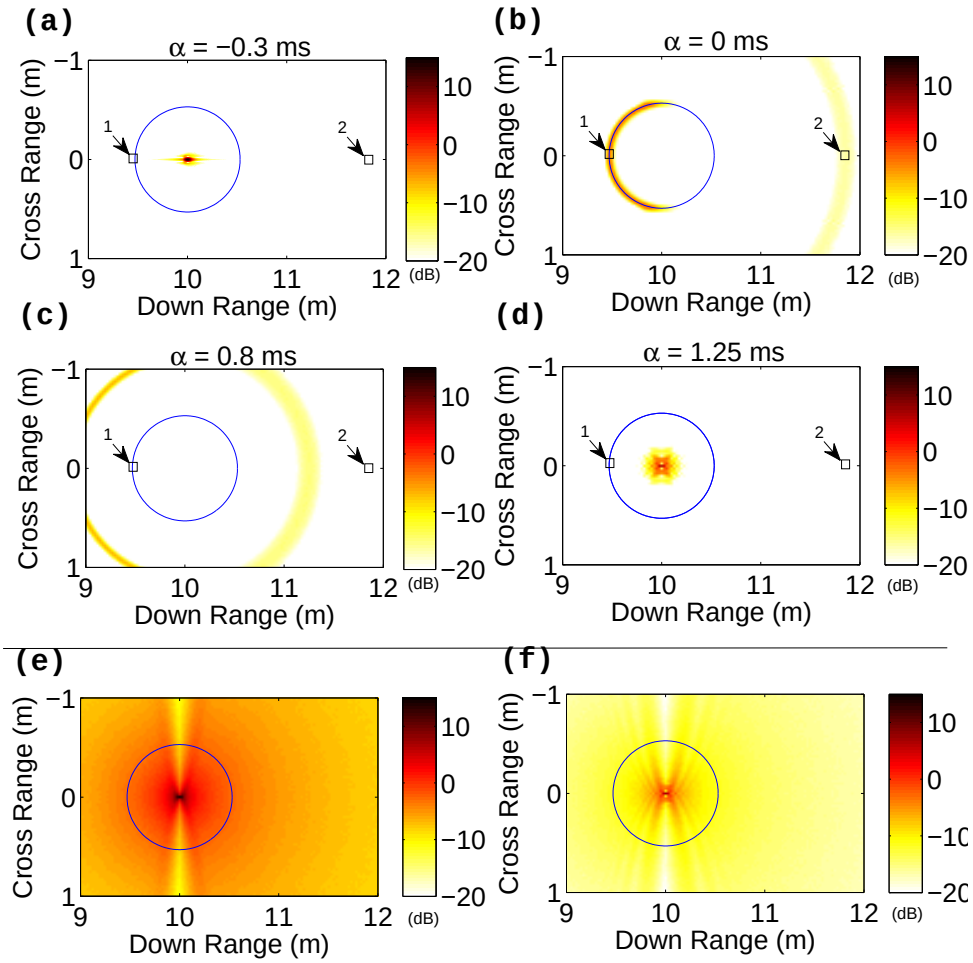

Figure 4.5: Spatio-temporal evolution of the integrated value of the beamformer envelope $C_{i,j}(\alpha)$ (see Eq. (24)) of the monostatic response of a spherical shell for four increasing time-delays (a) $\alpha = -0.3$ ms, (b) $\alpha = 0$ ms, (c) $\alpha = 0.8$ ms, and (d) $\alpha = 1.25$ ms. (e) Amplitude variations of the MSM output $D_{i,j}$ (see Eq. (25)) using only the portion of the backscattered data corresponding to the specular echo. (f) Same as (e) but using only the portion of the backscattered data corresponding to the first elastic echo. The solid circle overlaid on the imaging area-centered at (10m,0m)-indicates the location of the shell's outer surface. All logarithmic values (dB scale) were normalized by the same reference amplitude defined here as the maximum amplitude of the refocused specular echoes measured along the shell's outer wall on the conventional acoustic image shown in (b).

4.3.3 Acoustic imaging of the bistatic response of a thin spherical shell

Fig. 4.3b displays the simulated bistatic response (i.e. where the source and receiver's azimuth angle differ) of the same spherical shell used in the previous section. This bistatic response was computed by keeping the far-field source at an azimuth of $\theta = 180°$ while the receiver's azimuth vary from θ =90° to θ =270° at 1° increments thus covering the same 180° circular aperture sketched in Fig. 4.2. Fig. 4.3b displays the variations of the shell's bistatic response across the $N = 180$ receiver positions. The first wavefront still corresponds to the specular echo. But contrary to the previous monostatic configuration, the first elastic echo is now split in two branches corresponding to the clockwise and counter-clockwise antisymmetric Lamb waves propagating around the shell[5]. Later replicas of this X-shaped feature correspond to multiple revolutions of these two counter-propagating Lamb waves. Thus, the clockwise and counter-clockwise Lamb waves effectively appear as two moving sources circling around the shell while radiating energy into the surrounding fluid. Note that these two counter-propagating Lamb waves interfere constructively for θ =180° (monostatic configuration) to generate a single enhanced return centered at t=7.7 ms (see Fig. 4.3a).

In a similar fashion to Fig. 4.5a-d, Fig. 4.6a-d display four successive frames of the backprogation movie generated using this bistatic response of the spherical shell. To ease comparison, the logarithmic values of $C_{i,j}(\alpha)$ displayed in each of the four frames were also normalized by the maximum value of $C_{i,j}(\alpha = 0 \text{ ms})$ over the imaging grid (i.e. as shown on the conventional acoustic image on Fig. 4.6a). As expected, this conventional acoustic image Fig. 4.6a shows that the specular echo is focused around the front of sphere's contour -facing the receiver array- while the first elastic echo appears defocused at the back of the sphere (i.e. spread in the cross-range direction at a down-range of 10.5) with a low amplitude of -16.9 dB. On the other hand, Fig. 4.6b-d show the progressive spatio-temporal refocusing of the bistatic elastic echoes

as two bright spots circling around the shell-fluid interface in a symmetric fashion. These trajectories of these bright spots appear to trace back the original path of the original circumnavigating Lamb waves while radiating into the surrounding fluid. For instance these refocused elastic echoes are visible at a 10 m range and ± 0.5 m cross range location on Fig. 4.6c for a time delay $\alpha = 0.94$ ms, or at a 9.6 m range and ± 0.45 m cross range location on Fig. 4.6d for a later time delay $\alpha = 1.4$ ms. Thus the full spatio-temporal refocusing of the bistatic response of the thin spherical shell provides additional insights on the generation mechanism and spatial origin of the elastic echoes, when compared to the single frame Fig. 4.6a corresponding to the conventional acoustic image.

Finally, Fig. 4.6e and Fig. 4.6f display the acoustic images of the bistatic response of the spherical shell obtained with the MSM (see Eq. (25)) after selecting respectively the specular or first elastic wavefront from the received bistatic data (see Fig. 4.3b). When compared to the 0 dB reference for the amplitude of the specular echo in the conventional acoustic image shown in Fig. 4.6a, the specular echo appears instead as a concentrated energetic bright spot on the MSM image (see Fig. 4.6e) centered at a 9.7 m range and 0 m cross range location with a significantly higher amplitude of +19.7 dB. Similarly the maximum amplitude of the elastic echo on the MSM image (at a 10.3 m range and $\pm$ 0.5 m cross range location on Fig. 4.6f) is -11.2 dB, i.e. 5.7 dB higher than the amplitude of the elastic echo on the conventional acoustic image (see Fig. 4.6a). Furthermore, the refocused energy of the elastic echo is also clearly localized around the shell-fluid interface and not behind the shell as in Fig. 4.6a, -thus confirming that both specular and elastic echoes are generated by the same elastic target instead of two closely spaced targets.

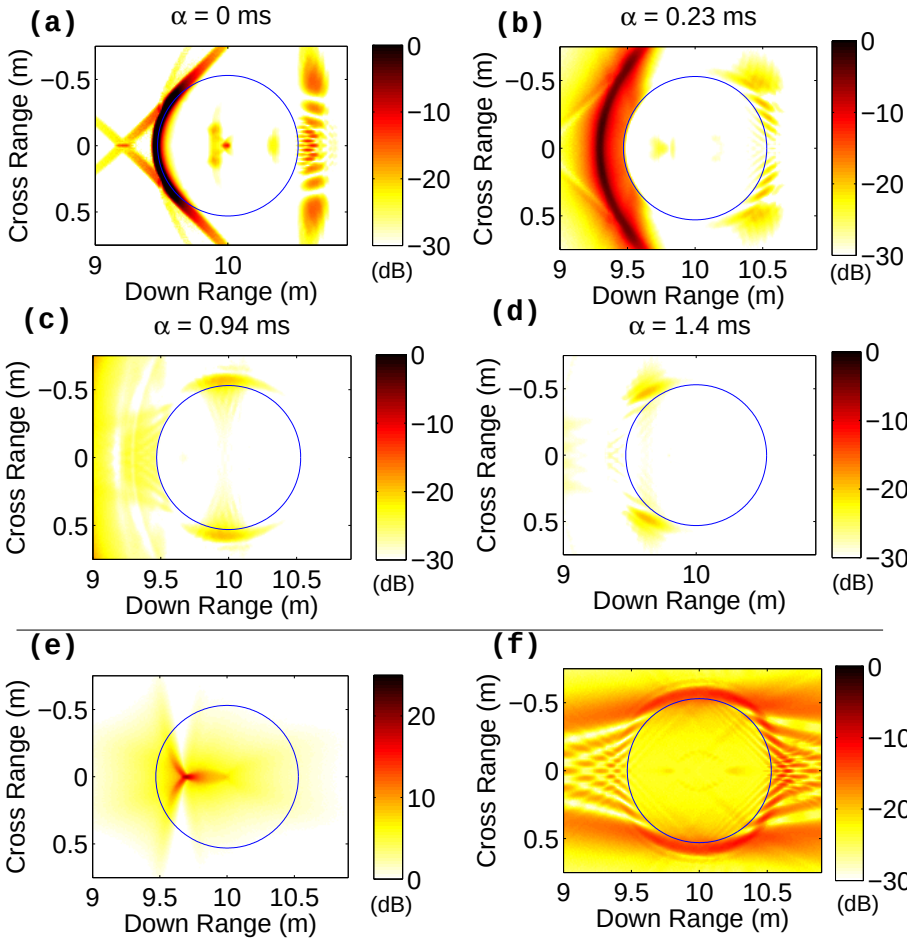

Figure 4.6: Same as Fig. 4.5 but showing instead the spatio-temporal evolution of the integrated value of the beamformer envelope $C_{i,j}(\alpha)$ of the bistatic response of a spherical shell. Note that for four different time-delays were selected here (a) $\alpha = 0$ ms, (b) $\alpha = 0.23$ ms, (c) $\alpha = 0.94$ ms, and (d) $\alpha = 1.4$ ms.

4.4 Experimental Results

4.4.1 Experimental set-up

The monostatic responses of a thin steel spherical shell and a solid aluminum cylinder were measured during experiments conducted by the Naval Surface Warfare Center (Panama City, Florida) at their instrumented pond facility, which is a 14-m deep, 110-m long, and 80-m wide test-pool with a 1.5 m layer of sand on the bottom. The sound speed in the water was 1486 m/s. The experimental collection methods and apparatus is discussed in details in a previous study[97] conducted by the team of

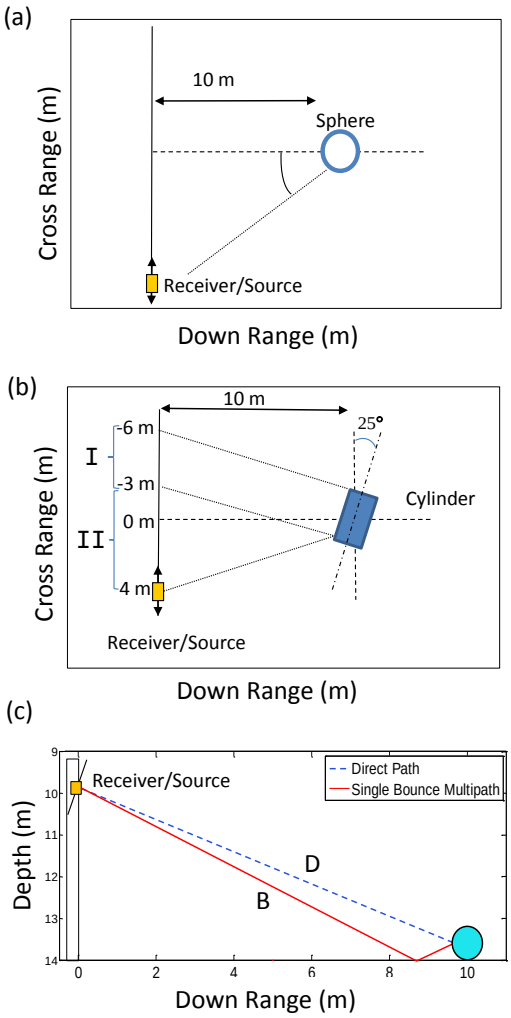

Figure 4.7: Overhead view of the experimental geometry used for backscatter measurements of (a) the thin spherical shell and (b) solid cylinder. (c) Elevation view of the experimental geometry. The direct and single bottom bounce paths between the target and source/receiver locations are also indicated qualitatively.

researchers who shared these acoustic backscatter data from the experiment. In short, the source and receiver array were mounted in quasi-monostatic configuration on a rigid tower frame and were located at a depth of 10 m (see Fig. 4.7c). The transmitter and receiver array were mounted on a panel -tilted at 20° angle towards the bottom and were separated horizontally by about half a meter. The receiver array, composed of six hydrophones, had a 10 cm horizontal aperture and 1 m vertical aperture. The

received signals by the 6 elements were added coherently (broadside summation) to minimize scattering interference from the water/air boundary. The source-receiver tower was moved in 2.5 cm increments along a 20 m long rail to create a synthetic aperture and collect backscattering measurements of the elastic targets over a 40° aperture (see Fig. 4.7a-b). The transmitter maintained a horizontal beamwidth greater than 40° over the entire frequency band to allow for SAS processing. At the point of closest approach- corresponding to a cross-range of 0.8 m here- the horizontal distance between the source-receiver tower and targets (both centered on approximately the same location) was close to 10 m. From these measurements, the grazing angle for the ray drawn from the centers of the transmitter and receiver array to the center of each target was approximately 21° (see Fig. 4.7c).

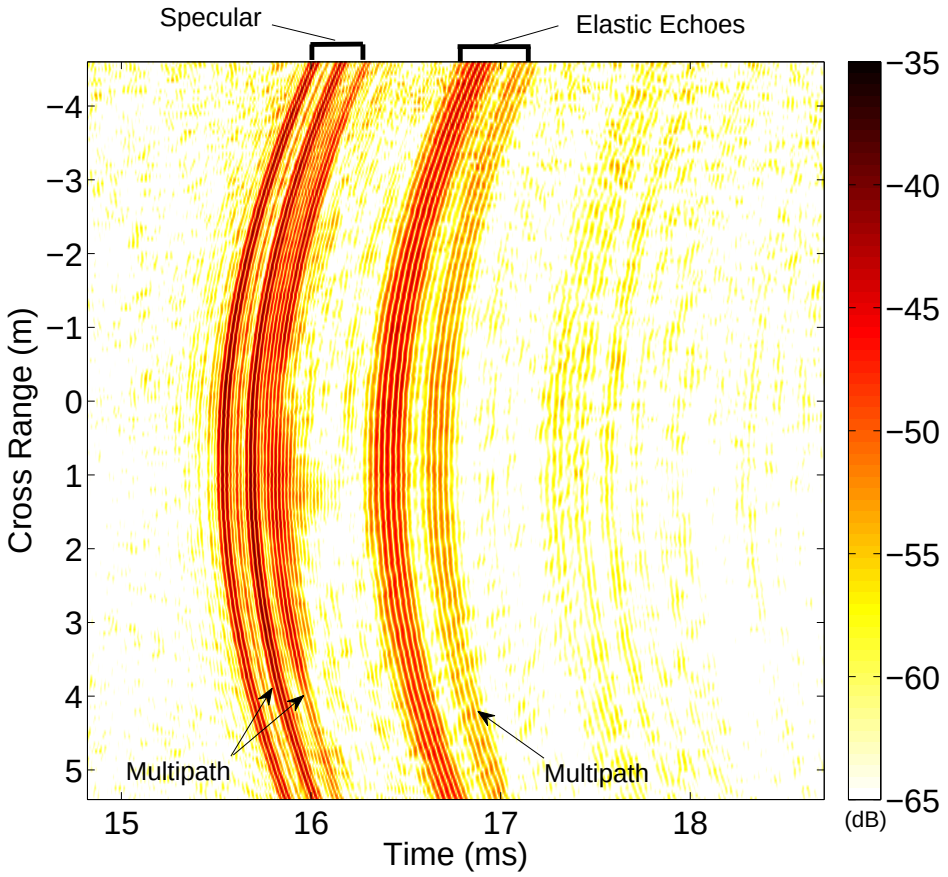

Figure 4.8: Evolution of the envelope (in logarithmic scale) of the spherical shell's backscatter vs receiver's cross-range. The group of arrivals the specular and later arriving elastic echo's are labeled. Two main groups of wavefronts, centered respectively around 16 ms and 16.8 ms, correspond respectively to the specular echo and first elastic echo (A_0 wave) of the spherical shell convolved with the multipath arrival structure of the shallow water waveguide (see Fig. 4.7c). The amplitudes were normalized with respect to the maximum displayed value.

4.4.2 Thin Spherical Shell

The first target studied was a hollow 59.9 cm diameter steel spherical shell with a thickness of 1.54 cm (density = 5773 kg/m^3, compressional velocity = 7970 m/s and shear velocity = 3020 m/s). Using the setup described in the previous subsection, the sphere was excited by a linear frequency modulated (LFM) waveform ranging from 12 kHz to 28 kHz. Fig. 4.8 displays the 400 backscatter signals measured by the source-receiver tower while moving in 2.5 cm increment along the cross-range axis, the image

shows illumination of approximately an arc of 37° on the sphere (slightly less than the 40° aperture used). Two main groups of wavefronts, centered respectively around 16 ms and 16.8 ms, correspond respectively to the specular echo and first elastic echo (i.e. antisymmetric guided wave) of the spherical shell convolved with the multipath arrival structure of the shallow water waveguide. Based on a simple ray approximation (see Fig. 4.7c), these various arrivals shown on Fig. 4.8 can be interpreted as acoustic energy traveling along four different paths between the source and receiver arrays, namely (1) the first direct reflection path (Source-Shell-Receiver path), followed by (2) two reciprocal paths of equal length (thus recorded simultaneously by the receivers) interacting only once with the bottom (Source-Shell-Bottom-Receiver and Source-Bottom-Shell-Receiver paths) and finally (3) a path interacting twice with the bottom (Source-Bottom-Shell-Bottom-Receiver) thus having a weaker amplitude than the previous paths. Note, that the angles of incidence on the shell of these bottom-interacting multipath effectively introduce bistatic scattering paths even though the source and receiver are arranged in a quasi-monostatic geometry [97, 26, 20]. This bistatic effect can be seen if an approach of an image source and receiver is used to analyze the multipath, as discussed in Appendix C.

In a similar fashion to Fig.4.5a-d, Fig.4.9a-d displays the successive spatio-temporal refocusing and defocusing of the experimental backscattered wavefronts shown on Fig. 4.8 along the pond's bottom in the vicinity of the sphere's location (indicated by a thin line). In particular, the elastic echoes located along the back wall of the shell (at an average down range of 10.5 m) appear slightly defocused with an amplitude of -2.7 dB on the conventional acoustic image (Fig. 4.9b, $\alpha = 0$ ms). But the same elastic echoes are more tightly focused at the sphere's center on the next selected frame of the backpropagation movie (Fig. 4.9c, $\alpha = 0.74$ ms) and consequently are imaged with a slightly higher amplitude of 1.0 dB.

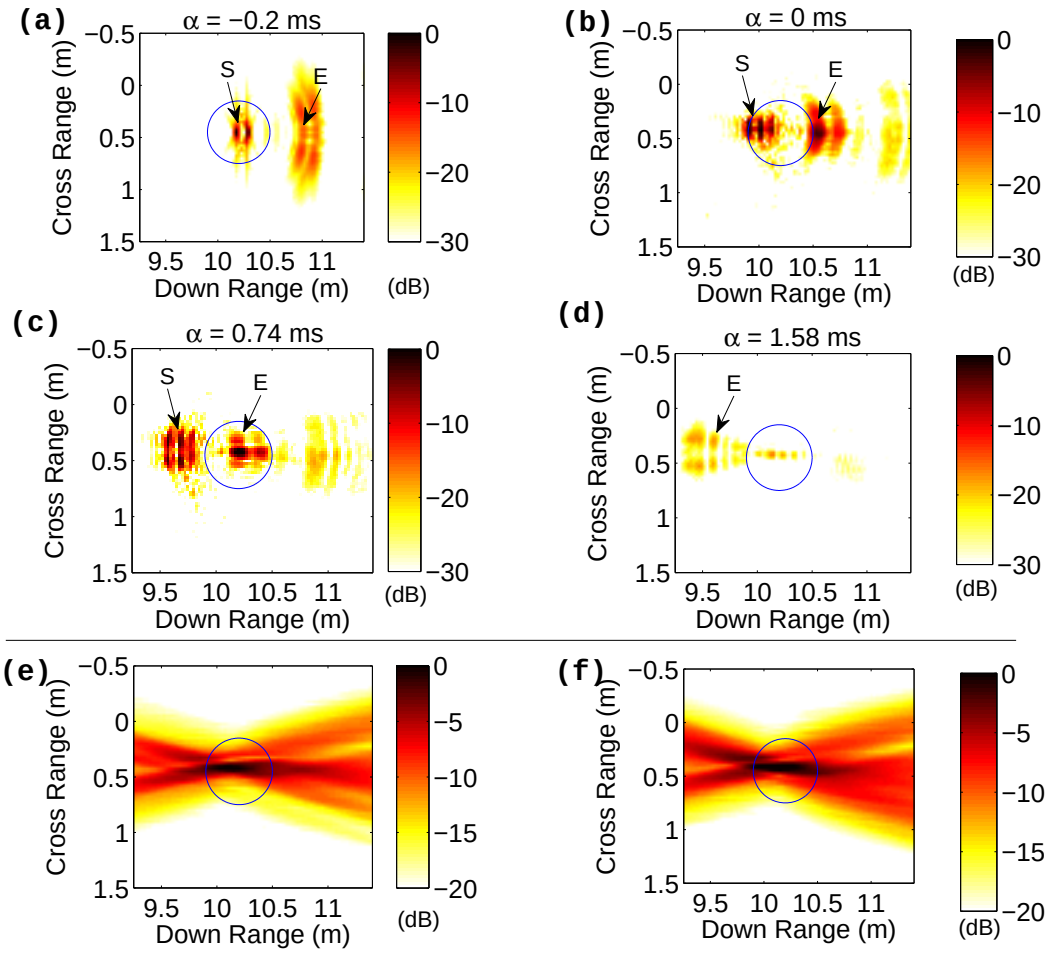

Figure 4.9: Spatio-temporal evolution of the integrated value of the beamformer envelope $C_{i,j}(\alpha)$ (see Eq. (24)) of the monostatic response of a spherical shell for four increasing time-delays (a) $\alpha = -0.2$ ms, (b) $\alpha = 0$ ms, (c) $\alpha = 0.74$ ms, and (d) $\alpha = 1.58$ ms. The refocused specular (labeled S) and elastic echoes (labeled E) are marked on each plots. (e) Amplitude variations of the MSM output $D_{i,j}$ (see Eq. (25)) using only the portion of the backscattered data corresponding to the specular echo (f) Same as (e) but using only the portion of the backscattered data corresponding to the first elastic echo. The solid circle overlaid on the imaging area indicates the approximate location of the shell's outer surface. All logarithmic values (dB scale) were normalized by the same reference amplitude defined here as the maximum amplitude of the refocused specular echoes measured along the shell's outer wall on the conventional acoustic image shown in (b).

Furthermore, similarly to Fig. 4.5e-f, Fig. 4.9e-f shows the acoustic images obtained with the MSM output (see Eq. (25)) after selecting respectively the specular or first elastic wavefront from the measured backscattered wavefronts shown on Fig.

4.8. Compared to the conventional acoustic image, (Fig. 4.9b, $\alpha = 0$ ms), the maximum amplitude of the refocused specular and elastic echoes are now located near the sphere's center at a down range of 10 m. In particular, the maximum amplitude of the elastic echo displayed on the MSM image (Fig. 4.9f) appears to be +6dB higher than the maximum amplitude of the elastic echo displayed on the conventional acoustic image (Fig. 4.9a). But this increase in refocused amplitude in the MSM image (Fig. 4.9f) comes at the expense of the spatial localization of the elastic echo when compared to conventional acoustic image (Fig. 4.9b). Hence the refocused energy is now "smeared" across the down range (or time resolution) direction due to the definition of the MSM output in Eq. (25). Indeed, this smearing of the focus region on Fig. 4.9f along a X-shaped pattern (whose branches are centered on the sphere's center) corresponds of the whole area illuminated by the refocused elastic wavefront while it successively converges to and diverges away from the sphere's center (as shown in the successive frames on Fig. 4.9a-d). Furthermore, when compared to Fig. 4.5f, the spatio-temporal refocusing on the sphere's center is significantly less pronounced on Fig. 4.9f as the received backscattered wavefronts are now only measured across a limited angular aperture of 40° instead of the larger aperture of 180° used for the numerical simulations. A similar explanation can be applied when comparing the spatial extent of the refocused specular echo on Fig. 4.9b and Fig. 4.9e.

4.4.3 Model Validation and Experimental Comparison

Though the model and numerical methods have been well studied, the implementation and work in this research benefits greatly from the validation of the model with experimental results. Objectives of this section are to validate the results of the imaging method and the numerical mode based on the results from the experimental data. Additionally the model allows one to isolate the features to confirm behavior and echoes associated with each image feature. For this purpose the data from the

spherical shell will be compared directly to that of the numerical model.

The numerical model presented in Chapter II was implemented using parameters that match the conditions of the experimental data, in order to validate the code and verify the imaging results. The following model parameters where modeled: a 59.9 cm diameter steel spherical shell (density = 5773 kg/m^3, compressional velocity = 7970 m/s and shear velocity = 3020 m/s). The model is excited by a Gaussian shaded pulse ranging from frequencies of 12 kHz to 28 kHz, which is the same spectrum and length as the matched filtered LFM pulse used in the experiment. The backscatter data was calculated across 400 positions to simulate the source-receiver positions at 2.5 cm increment along the cross-range axis, thus illuminating an approximate arc of 40° on the sphere. The sound speed of the water was modeled as 1486 m/s. The distance at the point of closest approach to the target was set to 10 m. The comparison of the backscatter data at the point of closest approach for the model and experiment is shown in Fig. 4.10.

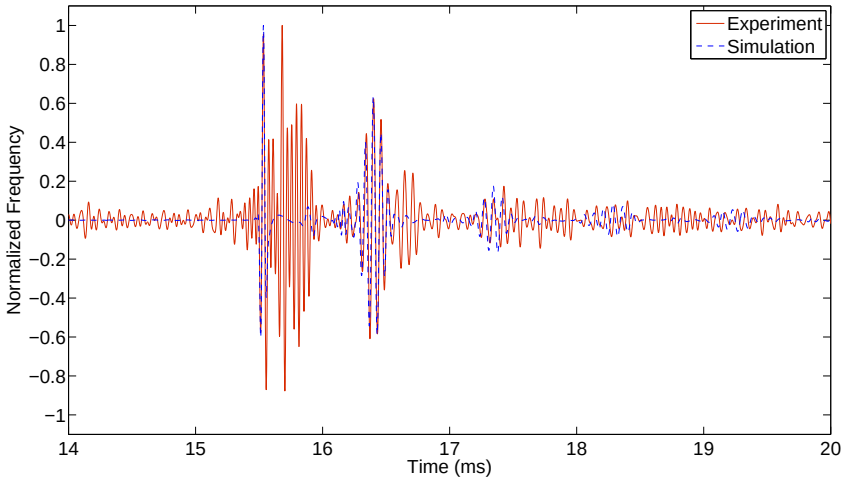

Figure 4.10: Comparison of experimental (solid line) and model (dashed line) backscatter data at the point of closest approach from source/receiver to the target.

The direct comparison of the time series from the model data and experimental

data, shown in Fig. 4.10 verifies the expected behavior in both the model and experiment, with a broadband specular arrival and subsequently a narrower band elastic echo arrival. For easier comparison, the signals are overlaid and the first specular arrivals are time aligned. For this comparison, the multipath effect of the experimental data was neglected on the model, but will be added in for comparison of the imaging results. The comparison reveals that the peak of the first (direct path) elastic echo arrives 0.88 ms and 0.87 ms after the specular echo for the experimental data and model respectively.

Furthermore the center frequency and behavior of the time-frequency representation of the model and experiment are presented in Fig. 4.11. Measuring the peak amplitude of the elastic echo results in the center frequencies of 16.75 kHz (data) and 16.65 kHz (model) with an uncertainty of $\pm$ 150 Hz in the approximation of the instantaneous frequency. These results in combination with the time series overlay show close matching of the numerical and experimental results and thus verify the model is accurate for the thin spherical shell. It would be beneficial for future work to validate the model with other types of materials similar to those presented in Chapter II.

Additionally to confirm the results and impact of each component on the image formation, a model to data comparison will be presented here. For the standard imaging method, the multipath has significant impact on the image, and therefore the imaging model includes the first energetic multipath effect. The multipath effect induced by the bottom reflection was simply simulated by adding the free-space contribution of various image spheres with respect to the bottom interface following the approach used by Williams et al. [97] and presented in Appendix C. This approach neglects the reduced energy of the reflection off the sediment. This loss can be neglected since the second arrival is actually a combination of two simultaneous arrivals of the single bottom bounce (Source-Shell-Bottom-Receiver and Source-Bottom-Shell-Receiver

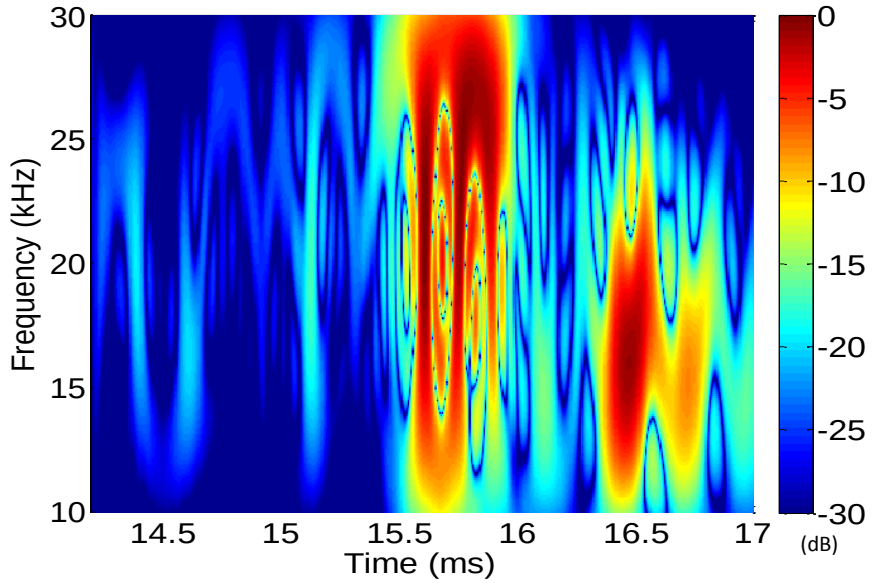

(a)

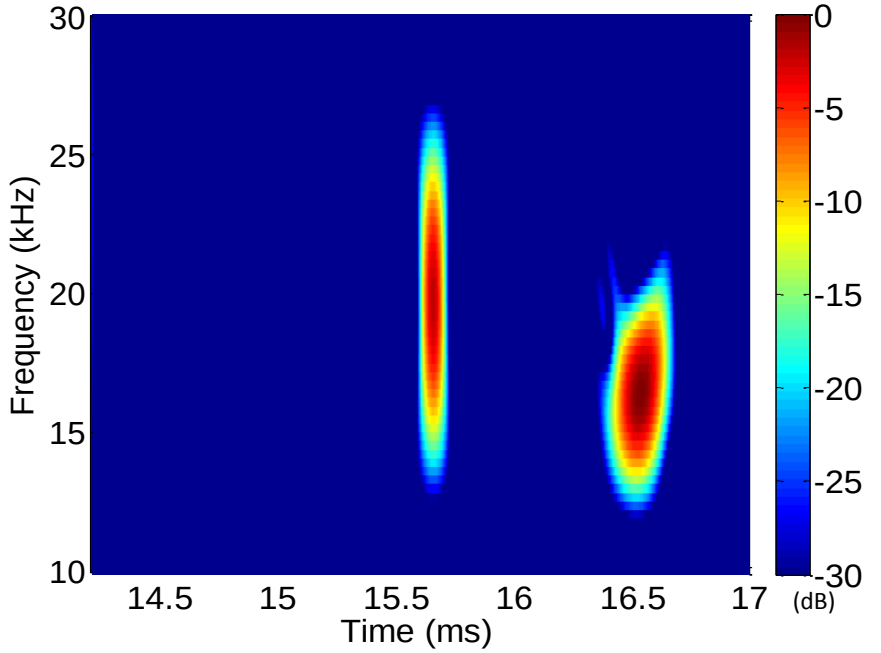

(b)

Figure 4.11: Time-Frequency Distribution of Model and Experiment results, where the model amplitude was normalized to the max amplitude of the experimental data. Center Frequency of model = 16650 ±150 Hz dt between spec and MFE = 0.87 ms, for experiment Fc=16750 Hz and dt =0.88 ms

paths), which is a fairly energetic return.

Using the same numerical model as previously presented, a comparison of the experiment and model imaging was conducted for two reasons. The first was to discern if the arrivals after the specular were associated with the multipath and elastic response, as opposed to possible clutter or noise. The second was to verify that the expected spherical shell model images match the results from experimental data. Good agreement is shown between the numerical model in Fig. 4.12 for the different imaging methods, though slightly more curvature can be seen in the specular (9.75,0) image. This difference is most likely due to the plane wave source in the model being able to fully illuminate the target at all angles equally, whereas the experimental data does not illuminate the sphere equally over all cross ranges.

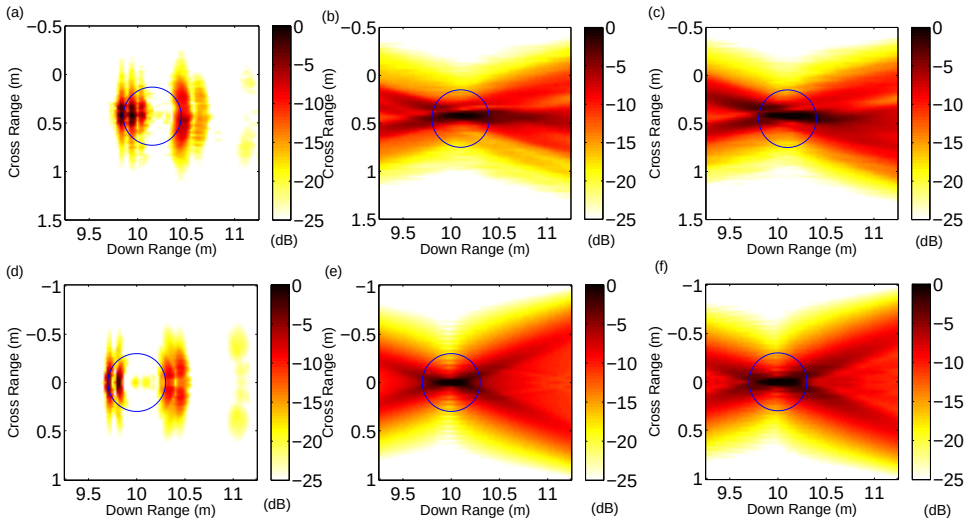

Figure 4.12: Acoustic images of monostatic spherical shell for experimental data for (a) conventional imaging method (b) MSM image of the specular echoes and (c) MSM image of the elastic echoes. Simulated data matching the experimental setup for (d) conventional imaging, and (e) MSM image of the specular echoes and (f) MSM image of the elastic echoes. The solid circle overlaid on the images indicates the approximate location of the shell's outer surface. All logarithmic values (dB scale) were normalized by the same reference amplitude defined here as the maximum amplitude of the refocused specular echoes measured along the shell's outer wall on the conventional acoustic image shown in (a) and (d). The refocused specular (labeled S) and elastic echoes (labeled E) are marked on (a).

Overall, the simulated imaging results shown in Fig. 4.12d-f closely match the experimental results shown in Fig. 4.12a-c, thus confirming the previous interpretation in Section 4.4.2 of the spatio-temporal refocusing of the shell's elastic response in the presence of multipath effects.

4.4.4 Solid Aluminum Cylinder

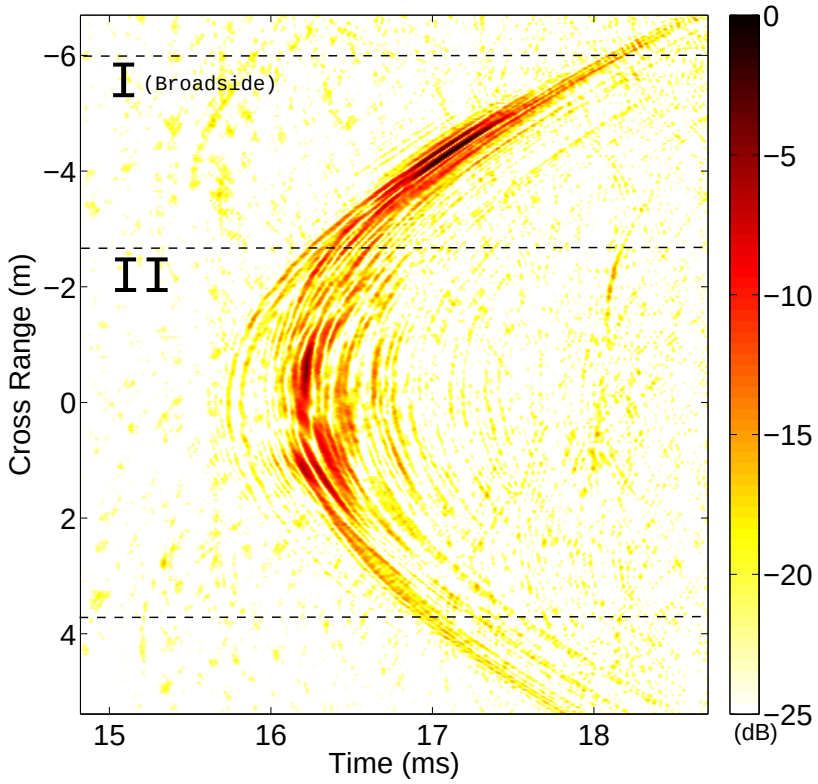

Figure 4.13: Evolution of the envelope (in logarithmic scale) of the solid cylinder's backscatter vs receiver's cross-range. The amplitudes were normalized with respect to the maximum displayed value. The section labeled (I) and (II) along the cross-range axis correspond to the receiver laying broadside or approximately 25° off-axis from the cylinder (see Fig. 4.7b).

The second elastic target under study is a 30.6 cm by 61 cm solid aluminum cylinder. The cylinder was excited by a 6 ms long linear frequency modulated (LFM) waveform ranging from 1 kHz to 30 kHz, transmitted every 2.5 cm along the 20 m track. Figure 4.13 displays the stacked backscattered measurements (obtained after

matched filtering) measured along the receiver's track. Due to the lack of axisymmetry about all axes, the orientation of the cylinder relative to the receiver array must be considered for detection purposes. As indicated in Fig. 4.7b, when the receiver's cross range lies between -6 m to -3 m (labeled as Section I), the receiver array orientation lays approximately parallel or broadside to the cylinder's main axis. Fig. 4.13 shows that the backscatterer measurements collected over broadside Section I correspond to high amplitude echoes caused by the specular reflection of the cylinder in a quasi-monostatic configuration. On the other hand, when the receiver's cross range lies between -3 m to 4m (labeled as Section II), the cylinder is insonified at a tilted angle of approximately 25° ±15°. This off-axis insonification efficiently excites guided waves (meridional and helical elastic waves) radiating back to the receiver [97]. An additional acoustic feature in the data is the earliest faint arc (t = 15.9 ms) that extends through both regions. This faint arc can be attributed to the edge diffraction of the cylinder, while the faint replica behind this arc can be attributed to multipath effect. Further discussion and details of the nature of these waves can be found in previous studies.[97, 7]

Fig. 4.14a-c displays three frames of the backpropagation movie for the cylinder's backscatter data recorded under broadside illumination only (i.e. for receivers located within Section I). As expected, the conventional acoustic image (see Fig. 4.14b) show that the refocused specular echoes and multipath replicas highlight the cylinder's length insonified by the broadside illumination. This good spatial focusing indicates that the distributed bright-spot model is applicable to the backscatter data-dominated by specular echoes- recorded under broadside illumination. However, when using this quasi-monostatic source/receiver configuration, the wavefronts associated with these specular echoes were recorded only a very small cross-range aperture (≈1m) and thus had very little curvature . Consequently, this short receiver aperture limits the effective amplitude of the refocused field. This short aperture also explains why

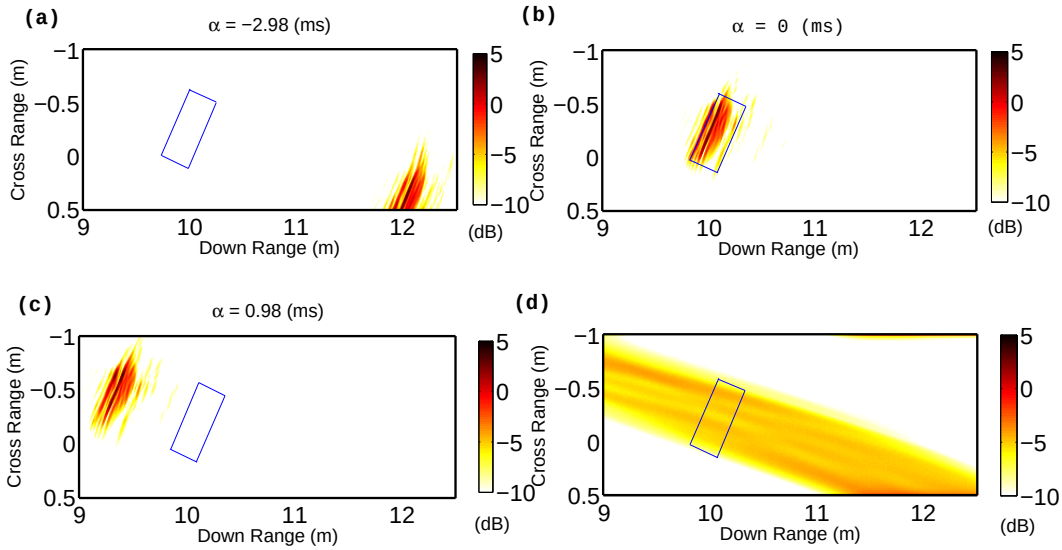

Figure 4.14: Spatio-temporal evolution of the integrated value of the beamformer envelope $C_{i,j}(\alpha)$ (see Eq. (24)) of the broadside backscatter of the cylinder (i.e. for receivers located within Section I-see Fig. 4.13) for three increasing time-delays (a)$\alpha = -2.98$ ms, (b)$\alpha = 0$ ms, and $\alpha = 0.98$ ms. (d) Amplitude variations of the MSM output $D_{i,j}$ (see Eq. (25)) using only the same portion of the backscattered data. The estimated cylinder location is marked with a solid line. All logarithmic values (dB scale) were normalized by the same reference amplitude defined here as the maximum amplitude obtained for the conventional acoustic image shown in (b)

the three progressive frames shown on Fig. 4.14a-c do not display the same focusing and diverging of the refocused field onto the cylinder's location as previously observed when imaging the spherical shell's data recorded along a much larger receiver aperture (see Fig. 4.8 and Fig.4.9a-c). Finally, Fig. 4.14 displays the amplitude variations of the MSM output $D_{i,j}$ (see Eq. (25)) for the same Section I of the backscatter data. Here, the MSM method fails to accurately localize the cylinder's location since the specular echoes were only recorded over a very short aperture, instead the refocused energy is "smeared" across the down range direction.

For comparison, Fig. 4.15 displays similar results for the backscatter data when the cylinder is insonified off-axis (i.e. for receivers located within Section II) thus

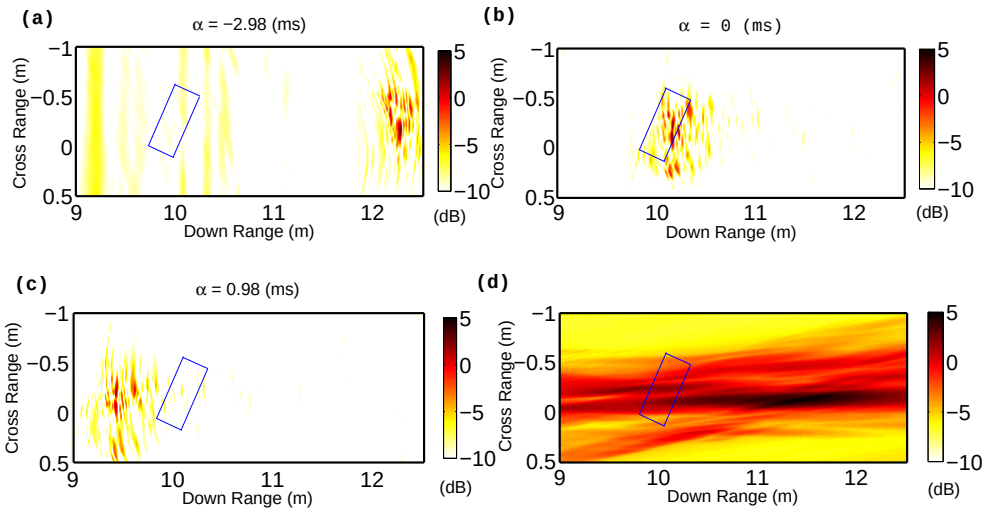

Figure 4.15: Same as Fig. 4.14 but using instead the off-axis backscatter of the cylinder (i.e. for receivers located within Section II-see Fig. 4.13).

favoring the generation of elastic echoes. Overall, Fig. 4.15 indicates that the free-space backpropagation approach does not yield a clear focusing of the elastic echoes regardless of the method used to image these echoes. These results confirm that that the distributed bright spot model is not directly applicable to elastic echoes having a complex generation mechanism such as meridional and helical elastic waves here. But, it can be noted that the MSM image (see Fig. 4.15d) provides a small-and potentially fortuitous- gain in refocused amplitude of +2dB when compared to the conventional acoustic image (see Fig. 4.15b).

4.5 Discussion and Summary

In conclusion, it can be noted that the original use of the free-space back-propagation algorithms (as done in SAS processing) was to primarily image the contours (and shadows) of rigid targets based on the "distributed bright-spot model" using only specular echoes. When using high-frequency monostatic SONAR systems and a sufficiently large receiving aperture, this approach can yield high-resolution acoustic

images which can be processed using automatic target recognition algorithms (typically relying on image processing) to detect specific target shapes. On the other hand, the development of low-mid frequency SONAR systems was motivated for their capability to excite and detect elastic echoes of the target of interest to enhance target's recognition and classification. So although acoustic imaging can be performed using low-frequency SONAR systems-as shown in this study- these systems can only offer limited spatial resolution for shape-recognition purposes due to their significantly larger insonification wavelengths. Furthermore, similar to glint angles of non-axis symmetric targets, these elastic echoes are frequently observed only over a limited angular aperture. This physically limits the effective recording aperture of these elastic echoes-especially for monostatic systems-which in turn drastically reduce the focusing ability of the standard acoustic imaging methods. To address this issue, one could use instead bistatic or multi-static low-frequency SONAR systems to obtain a wider coverage of the target's elastic echoes, thus potentially enhancing the probability of detection of these elastic echoes. However, due to their complex generation mechanisms, these elastic echoes cannot be effectively focused onto their spatial origin using a simple free-space back-propagation algorithm, contrary to well-behaved specular echoes. Consequently, this may ultimately limit the usefulness of SAS-like algorithms for accurately imaging the spatial origin of elastic echoes using low-frequency SONAR systems.

The numerical simulations and experimental results presented in this study indicate that the elastic response of simple targets (spherical shell and solid cylinder here) excited in the structural acoustic regime of frequencies create additional complexities for acoustic imaging. In particular, due to their specific generation mechanisms and radiation patterns, these elastic echoes (also referred to as elastic echoes) cannot be simply described by the distributed bright-spot model used for conventional acoustical imaging (e.g as used for SAS processing) of the specular echoes of the same

targets. Consequently, the elastic echoes can appear defocused (or blurred) and not centered on the target location on the conventional acoustic image. However, this study demonstrates that the same simple free-space beamforming algorithm used by conventional acoustic imaging can also provide images of the full evolution of the spatio-temporal refocusing (as a "back propagation movie") of both specular and elastic echoes. This was achieved by varying the selected time-windows of the beamformer output used for acoustic imaging to partially account for the delayed arrivals of elastic echoes with respect to specular echoes. Numerical and experimental results for a thin spherical shell indicate that this approach can significantly enhance the refocusing of elastic echoes onto the actual target's location if the echoes are effectively recorded across a large angular aperture (e.g. as used in circular SAS systems [60, 27]). In this case, this approach may produce acoustic images with higher SNR compared to conventional acoustic images obtained for a single reference time-delay. Thus in practice, this enhanced SNR could then provide a significant advantage for detecting elastic echoes in the presence of high level of ambient noise or clutter. However, experimental results for a solid cylinder show that this approach provides little focusing capability for elastic echoes radiating within a small angular aperture.

This chapter also investigated the possibility of condensing the whole information contained in the successive frames of the backpropagation movie into a single acoustic image (as done by conventional acoustic imaging) by simply representing the maximum refocused amplitude at each pixel of the acoustic image across all times. This modified imaging can thus yield a single acoustic image with higher amplitude for the elastic echoes, especially when using a larger aperture as done in circular SAS[60, 27]. However this modified imaging method loses the time resolution (or down range resolution) for tight focusing of the acoustic energy which becomes a clear disadvantage over conventional acoustic images, especially when using a limited receiver aperture. Thus overall, tracking the kinematics of the refocusing of high-amplitude features

associated with elastic echoes across successive frames of the whole backpropagation movie could potentially enhance the concurrent detection, classification and localization of elastic targets. Furthermore, the kinematics of the elastic echoes do not appear to be easily condensed in an optimal fashion in a single acoustic image: doing so appear to inherently limit the amplitude or spatial resolution of the refocused elastic echoes based on the two approaches (conventional and modified imaging methods) illustrated in this research.

The bistatic results for the spherical shell may be particularly useful since the elastic response essentially illuminates part of the shell that would not be able to be imaged with only the specular response in a bistatic recording. Additionally it is worthwhile to note on the imaging of the elastic response from a target that there is physically a limited aperture that is useful for elastic response from a target. Similar to glint angles of non-axis symmetric targets the elastic response will only be constructively combined on a limited range along an array. This is due to the acoustic energy being shed only in certain directions and not acting as a spherical or point source from the target's surface.

The important contributions to take away from this chapter are:

1. The back-propagated movie contains the information of the full scattered field and different approaches that exist to process the information from elastic targets.

2. The new maximum search method (MSM) proposed allows one to partially account for the non-free space propagation paths that the guided waves travel around a spherical elastic target.

3. This imaging method resulted in an improvement in maximum amplitude of the resultant image, but lost time information to focus the image. This resulted in a "smearing" of the image and required a large array angular coverage for

focusing the image to a recognizable target.

4. The bistatic result from the spherical shell and a 180° circular aperture provided an improved result using the MSM over the conventional approach, since it is able to focused the energy at the surface of the shell.

5. The physics of the guided waves on a solid cylinder limits the effective recording aperture (which is also the expected case for other complex shapes like truncated cones), thus practical use of simple imaging methods in this chapter is drastically reduced when applied to elastic echoes.

CHAPTER V

SPACE-TIME-FREQUENCY PROCESSING

5.1 Motivation

Noise reduction is a necessity in a variety of fields requiring signal processing, especially in SONAR and array processing. Measurements of any type have an inherent difficulty of recording a signal of interest in the presence of noise, which can have a detrimental effect on detection and classification performance. Noise can be the result of a variety of factors for acoustic measurements including ambient noise, thermal acoustic noise, reverberation, electrical line noise, flow noise etc. Methods for optimal array processing attempt to mitigate the impact of noise on a signal. Some common approaches include Wiener filter, frequency filtering, Kalman filtering, and beamforming (spatial filtering). An ideal solution to noise reduction would allow noise to be completely isolated from the signal and thus return an exact measurement of the input signal. This process in fact becomes extremely challenging when signal characteristics (e.g. duration, frequency content) are not precisely known a priori. Processing a signal without knowing the source specifics is often referred to as blind source separation in the literature [9, 63, 93, 99].

Further complications arise when processing non-stationary signals (signals that change in frequency content through time). These signals require broadband noise reduction techniques in order to not distort the original signal. Previous work has demonstrated that signal decorrelation occurs due to Doppler shift, and it has been shown that differential Doppler compensation is required for two sensor cross correlation cases [70]. There has also been previous work on handling noise reduction of non-stationary signals recorded across a receiver for the application of speech signals

[39]. Several methods currently exist to leverage this space-time-frequency information from an array. For example a wideband spatial processing method was developed using wavelets for the analysis of the received signals. But, this implementation is dependent on the selected wavelet basis functions used to decompose the received signals [95, 94]. There remains a need for noise reduction of signals that contain different frequencies (i.e. non-stationary signals) along the array itself. This is a standard problem dealt with in Doppler compensation of signals along an array. In addition to the Doppler application, this effect is shown in Chapter III where the signal from the MFE (elastic wave) of a spherical shell has an apparent frequency shift that is dependent on the bistatic receiver angle along an array. Chapter III applied a time-frequency beamformer developed for Doppler compensation to address the shift, which required knowledge of the time-frequency behavior. However, if the signal behavior is unknown, blind noise reduction techniques need to be implemented. The noise reduction problem for this research can then be posed to handle the non-stationary signal measured across an array.

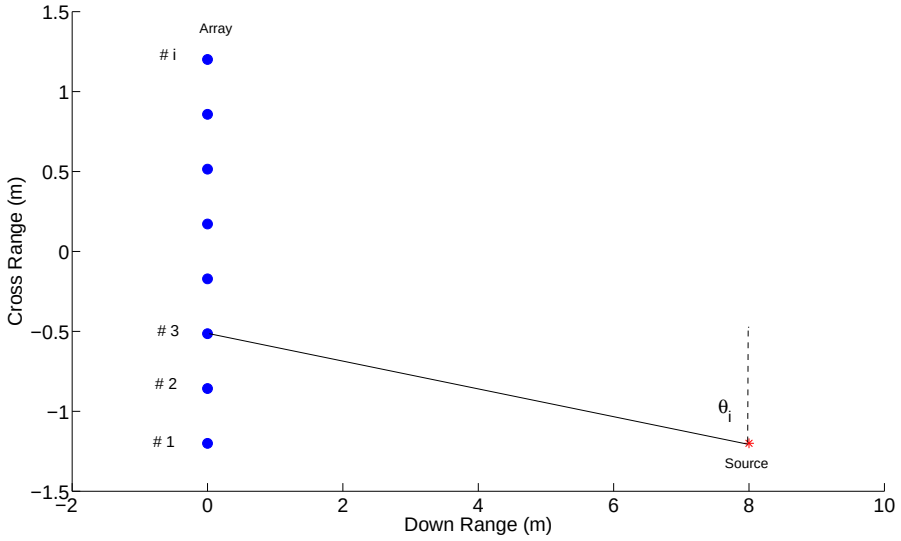

Figure 5.1: Schematic of the model setup with a source located 8 m from the receiver array (8 receivers) depicted with a radial range to each receiver at angle θ_i

In order to isolate one component of the bigger problem, this chapter will utilize an arbitrary time frequency relationship rather than the complex time-frequency behavior of guided waves measured bistatically from a spherical shell (see Chapter III). For this research and noise reduction method, a dilation parameter, β, and geometrical distance from source to each receiver will allow for each receiver in the array to record the source signal at a unique time and frequency shift. This arbitrary frequency shift will be defined by the following relationship:

$$\Delta f = -\frac{\beta}{c_0} cos(\theta_i) F_c \tag{26}$$

where the recorded change in frequency of the signal is dependent on the center frequency, F_c, and the source-receiver angle, θ_i, and the medium sound speed, c_0. This simple model will ease the analysis and allow control of the time and frequency behavior across the array.

This chapter will introduce the background and previous work done in this area. Then two previously developed broadband subspace methods utilizing the Singular Value Decomposition (sometimes referred to as Principle Component Analysis) will be reviewed and a third noise reduction method will be introduced. Finally, the use of the Space-Time-Frequency distribution incorporating the Smoothed Pseudo Wigner-Ville distribution is proposed to separate the signal from the background noise. This numerical tool is developed to process and enhance the signal for a non-stationary behavior measured along an array (i.e. Doppler, MFE, etc). In the following section these methods will be applied to a simple case of an arbitrary shift across an array for a performance comparison. A performance and parameter study of this space-time-frequency distribution (STFD-SVD) will be presented, followed by an application to data from the monostatic shell experiment presented in Section 4.4.

5.2 Background

There are many methods present in literature to reduce noise from a measured signal. The SVD and principle component analysis are subspace methods that allow the separation between noise and signal subspace, thus allowing for noise reduction [30]. The compact and sparse representation of a signal is extremely useful for noise suppression and signal detection, as it eases the signal detection. The quality of how sparse a signal is compared to the noise can be quantitatively measured with a Signal to Noise Ratio (SNR) metric. Known methods of obtaining a sparse representation of a signal include Fourier transforms as well as time-frequency transforms.

For example, a simple Gaussian pulse of 30 ms, with a center frequency of 500 Hz and a 100 Hz bandwidth can be simply represented in time and frequency domain (see Fig. 5.2). This signal will be the baseline pulse used in this chapter. The sampling frequency is set to 5 kHz hereafter. Without additive noise, the signal remains sparse in all three domain representations: Fig. 5.2a represents the Fourier domain, Fig. 5.2b is the Smoothed Pseudo Wigner-Ville (SPWV) time-frequency domain, and Fig. 5.2c presents the time domain representation of the pulse.

The addition of white Gaussian zero mean noise to the baseline pulse will, as expected, obscure the signal representation. A noise level with a standard deviation of 0.5 is added to the baseline pulse using the normally distributed pseudo-random number generator function "randn" built in to the numerical software MatLab, followed by a low-pass filter set at the Nyquist Frequency of 2.5 kHz. The three domains of interest, time, frequency, and time-frequency, are presented in Fig. 5.3. The signal is shown to be more sparse in the frequency domain than the time domain (compare Fig. 5.3a to Fig. 5.3c). This gain in signal to noise level is due to the spreading of the energy across all frequencies. The time-frequency domain is particularly useful for SNR gain when analyzing chirps as well as non-stationary signals. There is SNR gain across both time and frequency domains as shown in Fig. 5.3b. This gain is

due to the even spread of white noise across the entire domain, where as the signal is compact over its bandwidth in this domain.

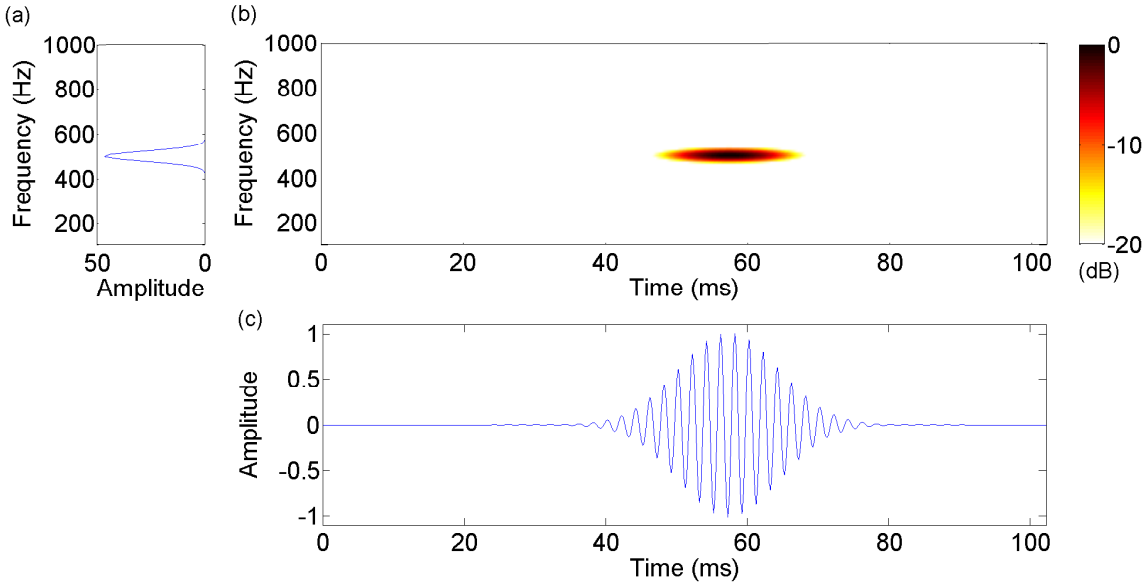

Figure 5.2: Depiction of the transmitted pulse without added noise: (a) Fourier domain depicting frequency content of the signal of a 500 Hz signal with a 100 Hz bandwidth, (b) time-frequency plot via Smoothed Pseudo Wigner-Ville distribution of the pulse, and (c) time domain signal of a 30 ms chirp emitted from the source.

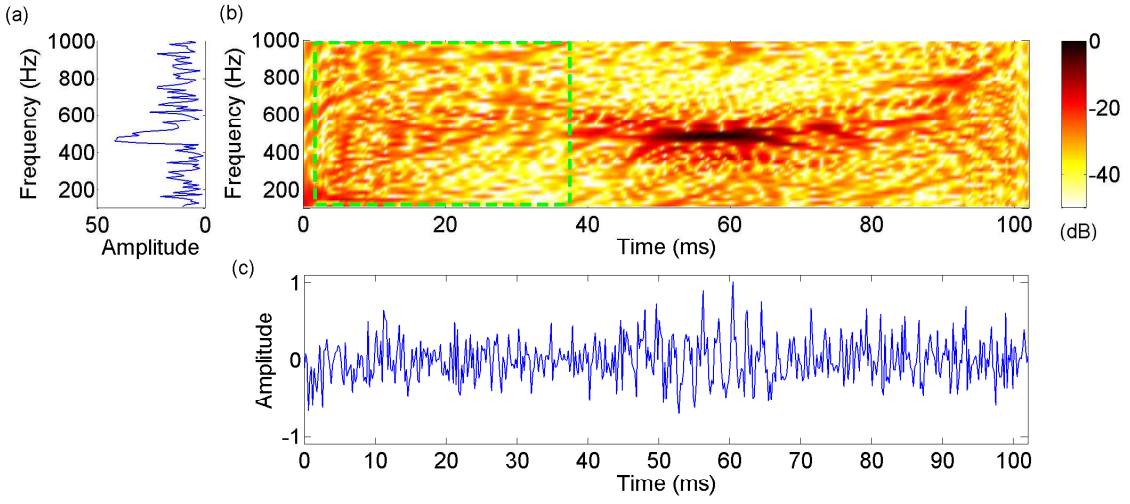

Figure 5.3: Time frequency representation of a signal from Sensor 1 (located at $y = -1.2$ shown in Fig. 5.1) with added whitenoise ($\sigma = 0.5$): (a) the frequency spectrum of the noisy signal, (b) Smoothed Pseudo Wigner-Ville Distribution, and (c) time domain plot of the signal.

Additional processing has been shown to further increase SNR (reduce noise) by using spatial domain behavior to process array data. For example there is extensive literature to handle RADAR jamming by non-stationary interference. Some of these methods include the use of the spatial time-frequency distribution (STFD which is discussed in further detail in Section 5.3.3) with subspace methods for use with Blind Source Separation by STFD, time-frequency multiple signal classification (TF-Music), and time-frequency minimum variance distortionless response (TF-MVDR) [9, 10, 17, 99, 108]. These studies assume a non-stationary signal is recorded across the entire array, and the use of wideband processing takes into account the change frequency content. However, for a Doppler signal the non-stationary behavior is recorded across the array (each receiver records a different time and frequency), and these methods may not be applicable. Additionally, the previous methods utilizing the Space-Time-Frequency distribution only proved to be effective when isolating the signal in the time and frequency space, requiring some a priori knowledge of the signal.

Further studies have shown Space-Time Adaptive Processing (STAP) is capable of wideband processing using the receiver (space), fast-time (time), and slow-time (snapshot) three dimensional space for processing. The STAP methods do not take full advantage of the time-frequency information across an array; unlike the STFD which uses it to characterize the non-stationary space-time-frequency data. Using the space-time-frequency coherence simultaneously will provide a means for improving processing non-stationary signals along an array and merits further investigation in this research.

For clarity the following sub-sections will present the basic background methodology used in modeling the noisy signal, present a means to measure SNR in the time-frequency domain, and introduce singular value decomposition for the purpose of noise reduction.

5.2.1 Discrete Signal Model

The method of developing a process for noise reduction requires a noisy signal model for the data from an array. For the purposes of this research the model is given as a simple linear mixture of original source signal (s) plus noise (ν). This model can also be represented for the observed discrete time samples, t, during the sample time as:

$$x_i[t] = s_i[t] + \nu_i[t] \tag{27}$$

where the subscript, i, indicates the sensor number on the array from $i = 1, 2, ..., N$, with N being the total number of sensors in the array. The added noise is modeled as zero mean white Gaussian noise, with a known variance, σ_v^2, and will be assumed to be uncorrelated across the array shown in Fig. 5.1. For physical arrays, this uncorrelated model may not hold since the dominant noise sources (reverberation, flow noise, ambient ocean noise) tend to be coherent. However, when the system is setup as a synthetic array each position of the receiver occurs at different times and locations and therefore the incoherent model will hold for flow and ambient noise, though not necessarily reverberation since this is environment dependent and will most likely not be affect by the different times the synthetic array data is captured. The signal at each sensor, i, is then modeled at different times and frequencies along the array to obtain a non-stationary signal along the array. The companded signal model presented in Chapter III, $x_i = s_i[\gamma_i(t+\tau_i)] + \nu_i[t]$, can be used to model the signal across the array for a time and frequency shift based on the propagation distance and frequency shift respectively. Where the parameter τ_i is selected for the time shift, and companding (or time-scaling) parameter γ_i is selected to model the frequency shift. This noisy signal model will be used to present noise reduction methods.

A discrete Fourier transform may then be applied to this signal to obtain a discrete representation of the signal in the frequency domain as presented in Eq. (28).

$$x_i[f] = FFT(x_i[t]) \tag{28}$$

In practice the discrete Fourier transform computes the Fourier domain representation of the signal using the numerically efficient Fast Fourier Transform (FFT). Here f denotes the frequency samples in Hz, and the Fourier samples are divided into finite length frequency bins of length ≈10 Hz given the selected sampling parameters and signal duration. The array data can then be represented by a set of single frequency vectors with entries for each receiver, where $X(f_l)$ represents the data vector across the array at frequency, f_l.

$$X(f_l) = [x_1(f_l), x_2(f_l), ..., x_i(f_l)] \tag{29}$$

It is now useful to define the conventional Cross Spectral Density Matrix (CSDM), sometimes referred to as the spatial correlation matrix since it contains the inter-element correlation information from the data within an array. This matrix has been defined and shown to be extremely useful in numerous optimal array processing techniques including beamforming [42, 89]. The CSDM is a narrowband matrix that computes the correlation between all inter-element array pairs at a specified frequency. This is simply implemented by taking the outer product (in frequency domain) of the array data as follows:

$$CSDM(f_1) = X(f_1)X^{\dagger}(f_1) = \begin{bmatrix} x_1(f_1)x_1^*(f_1) & \cdots & x_1(f_1)x_N^*(f_1) \\ \vdots & \ddots & \vdots \\ x_N(f_1)x_1^*(f_1) & \cdots & x_N(f_1)x_N^*(f_1) \end{bmatrix} \tag{30}$$

Here the notation † indicates the Hermitian transpose and $*$ indicates the complex conjugate of the scalar. Applying this formulation to noisy data allows the formation of a sample or estimated CSDM. This is simply an estimate of the expected or true value of the CSDM. Taking multiple "snapshots" of the array can provide a better

estimate of the true CSDM [59, 6, 79]. These snapshots are obtained using a fixed environment and signal behavior with different noise realizations. Previous studies have shown the number of snapshots, R, should be greater than two times the number of receivers, N, in the array ($R > 2N$) [69, 21]. This criteria was proposed in order to obtain a well conditioned (or a Full Rank) sample CSDM [69]. Studies and methods exist [59, 6, 79] to process and deal with rank deficient sample CSDM; however, for simplicity and for optimal performance, the numerical experiments in this research will be run with $R = 2N + 1$ ($R = 17$ here). Eq. (31) defines the expected value of the correlation by the linear addition of the snapshots.

$$\hat{\boldsymbol{C}} \equiv E\langle XX^{\dagger}\rangle = \frac{1}{R}\sum_{i=1}^{R}\{X_i[f]X_i[f]^{\dagger}\} \tag{31}$$

These discrete representations of the signal and estimated CSDM can now be used to present the methods for constructing noise reduction methods, which will be presented in the next section.

5.2.2 Signal-to-Noise Ratio

In order to properly quantify the performance for a given noise reduction method, it is necessary to perform a measurement of the signal level with respect to the noise level. This measure can however depend on the domain in which these levels are observed [98]. For example a narrowband signal in the presence of white noise can have a different measure of signal amplitude above noise amplitude between observations in the time or frequency domain (see Fig. 5.3). The narrowband signal will be sparse in the frequency domain (represented by very few Fourier coefficients). For the purpose of non-stationary signals, this research will be measuring the SNR of a given signal in the time-frequency domain, which allows for sparse representation, by spreading the noise energy across all time-frequency bins, allowing for a sparse representation of the signal. For this purpose, the method presented by Xiang et al. [98] for measuring SNR

directly in the time frequency domain will be used and is presented in the following equation:

$$SNR = \frac{\frac{1}{\beta}\sum_{t,f\in\beta}|SPWV[t,f]|^2}{\sigma^2} \tag{32}$$

where $SPWV[t,f]$ is the smoothed pseudo Wigner-Ville time-frequency representation (i.e. discrete time and frequency locations), β is defined as the area of domain for the signal above the -3dB level from the maximum amplitude measured, and σ^2 is the variance away from this region (selected as the boxed region in Fig. 5.3b). In general terms this method provides a ratio of the average signal power with respect to the noise level (variance).

5.2.3 Singular Value Decomposition Approach to Noise Reduction

For a subspace projection method, one must first estimate orthogonal subspaces of the data. The Singular Value Decomposition (SVD) has been shown to be a reliable tool for determining subspace projections [77, 93]. This method of using the SVD for subspace decomposition is presented here then applied to three noise reduction approaches in the following section. The SVD theory states that for any matrix $\boldsymbol{C} \in \mathbb{C}^{m\times n}$ ($\boldsymbol{C}$ is an element of the complex numbers of dimension $m \times n$), there exists unitary matrices $\boldsymbol{U} \in \mathbb{C}^{m\times m}$ and $\boldsymbol{V} \in \mathbb{C}^{n\times n}$ such that its decomposition can be written as follows [74]:

$$\boldsymbol{C} = \boldsymbol{U}\Sigma\boldsymbol{V}^{\dagger} \tag{33}$$

where Σ is the diagonal matrix whose entries are the singular values σ_i of C in descending order. The columns of $\boldsymbol{U}$ are referred to as the left singular vectors, and the columns of $\boldsymbol{V}$ are referred to as the right singular vectors. The singular values represent the energy content of the singular vectors.

An application of the SVD approach allows separation of the decomposition into subspaces. From Eq. (33) this subspace separation allows the CSDM $\hat{\boldsymbol{C}}$ to be written

as:

$$\hat{\boldsymbol{C}} = \begin{pmatrix} U_s & U_n \end{pmatrix} \begin{bmatrix} \Sigma_s & 0 \\ 0 & \Sigma_n \end{bmatrix} \begin{pmatrix} V_s & V_n \end{pmatrix}^{\dagger} \tag{34}$$

where Σ_s contains the largest singular values which are associated with the highest energy (i.e. signal space), and Σ_n contains the remaining noise space. It is important to note that this estimate of the signal subspace contains an amount of noise as well, and therefore it is not possible to completely remove the noise, without knowing the true subspace of the signal alone. The column vectors associated with U_s is the subspace spanned by the signal and therefore referred to here as the signal subspace, and U_n is referred to as the noise subspace. From linear algebra, it is known that U_s provides the orthonormal bases for the signal subspace [81]. Therefore the signal and noise subspaces are mutually orthogonal, and noisy array data can be projected onto the signal subspace by an projection matrix formed by these bases to obtain noise reduction [39, 89]. For this purpose the orthonormal projection matrix, P, can be calculated directly from the left singular vectors as follows:

$$P = U_s U_s^{\dagger} \tag{35}$$

This projection matrix can then be used to project to the noisy data onto the signal subspace:

$$PX(f_l) \approx [s_1(f_l), s_2(f_l), ..., s_i(f_l)] \tag{36}$$

The projected signal $PX(f_l)$ can provide a partially denoised replica of the original source signals, $s_i(f_l)$. This method for noise reduction by SVD can be implemented in a number of ways to account for different types of signal behavior. The following section will provide three approaches to noise reduction utilizing this subspace (signal space projection) applied to a non-stationary signal across an array.

5.3 Subspace Noise Reduction Methods

This section will present two previously developed noise reduction methods, and propose a third method. The first uses the CSDM and applies the subspace noise reduction independently frequency-by-frequency, essentially combining frequency data individually to create a wideband method, whereas the second method uses a 'super' CSDM that uses all the frequencies simultaneously for noise reduction, utilizing the cross-frequency coherence. The third proposed method uses space-time-frequency coherence simultaneously for noise reduction across the array. The goal of this section is not to provide an exhaustive presentation of denoising methods, but rather present techniques developed in literature, which are applicable to the denoising of signals that exhibit non-stationary behavior across an array for comparison to the proposed method. This section is divided into three subsections, each dedicated to introducing the concepts and implementation of the proposed methods.

5.3.1 Single Frequency Processing

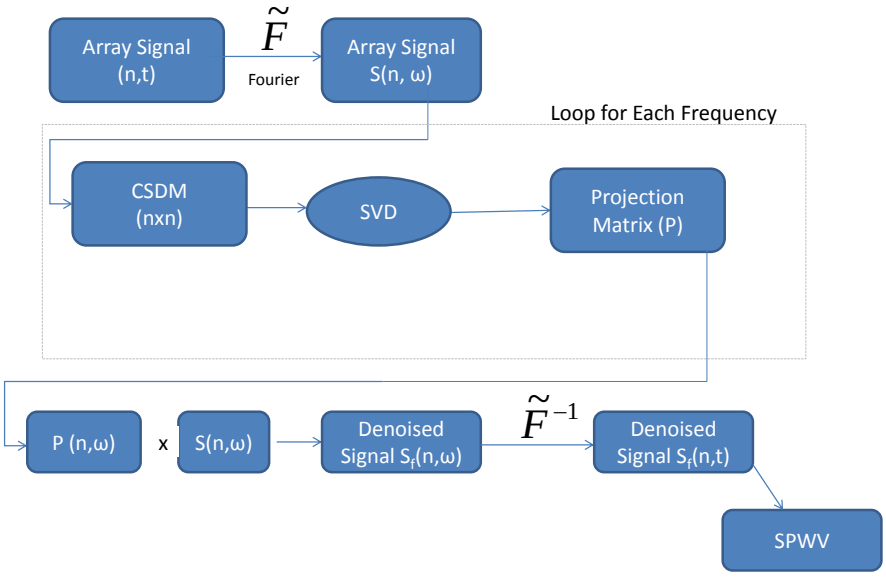

Figure 5.4: Depiction of the single frequency denoising process flow.

The first noise reduction method is the conventional and most widely documented method in literature [59, 39, 89]. The single frequency process uses the standard narrowband CSDM presented in Section 5.2.1. To incorporate broadband processing, the frequency data vectors are calculated via the FFT, denoised by the SVD project onto the signal subspace (done frequency by frequency), and then the denoised data vectors are recombined via the inverse Fourier transform (IFFT). This method is limited in its effectiveness in handling non-stationary signals as it only exploits spatial coherence along the array and can not take into account cross-frequency behavior that occurs in non-stationary signals.

The first step of this method is to take the Fourier transform of the data across the array and form the sample CSDM for each frequency. The CSDM is formed by taking the outer product of the data vector as shown in Eq. (30). Additional snapshots are combined to form an accurate estimate and full rank CSDM. For each frequency, the SVD of the CSDM matrix is formed; then the signal subspace is determined by selecting the highest valued singular values to create a projection matrix. The projection matrix is then applied to the frequency domain data vector. This is then repeated for all frequencies, and the projected data is recombined before taking the inverse Fourier transform to obtain the denoised signal. Fig. 5.4 depicts the visual process flow of this method, and indicates the loop to include all frequencies to extend the method to wideband processing.

5.3.2 Cross Frequency Processing

The next method was developed to coherently process wideband data across an array, and the schematic of the process described in this section is presented in Fig. 5.5. In order to accomplish the wideband processing of the array it has been shown that by concatenating the frequency data vectors from an array, one can form a super-vector as shown in Eq. (37) [17]. This super-vector can then be used in place of the single

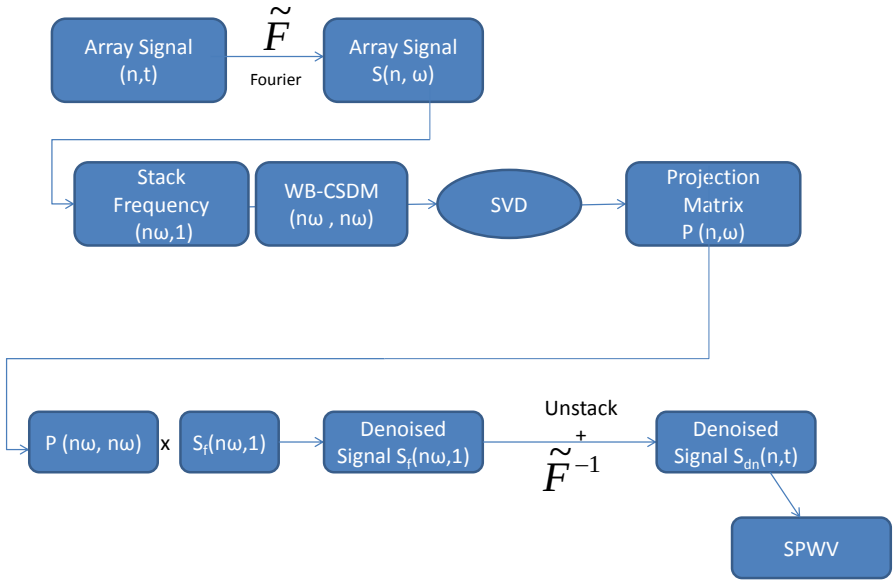

Figure 5.5: Depiction of the simultaneous frequency denoising process flow.

data vector $\boldsymbol{X}$ in Eq. (30) to create a "Super" CSDM.

$$\hat{\boldsymbol{X}} = [x_1(f_1), x_2(f_1), ..., x_N(f_1), ..., x_1(f_L), x_2(f_L), ..., x_N(f_L)]^T \tag{37}$$

For succinct representation $\boldsymbol{x}_i(f_l)$ denotes the frequency (complex field) received on the receiver, i, and f_l is the individual frequency bin to be considered. The construction of a Super-CSDM provides additional information between cross-frequency correlations as shown in the off diagonal terms in Eq. (38), which have been shown to be useful in processing non-stationary signals [17]. Once the Super-CSDM is formed, a similar SVD approach is applied to separate the signal and noise subspace, then project the super-vector onto the signal space to denoise the data.

$$\hat{\boldsymbol{X}}\hat{\boldsymbol{X}}^{\dagger} = \begin{bmatrix} x_1(f_1)x_1^*(f_1) & \cdots & x_1(f_1)x_4^*(f_2) & \cdots & x_1(f_1)x_N^*(f_l) \\ \vdots & \ddots & \cdots & \cdots & \vdots \\ x_4(f_2)x_1^*(f_1) & \cdots & x_4(f_2)x_4^*(f_2) & \cdots & x_4(f_2)x_N^*(f_l) \\ \vdots & \vdots & \vdots & \ddots & \vdots \\ x_N(f_1)x_1^*(f_1) & \cdots & x_N(f_1)x_4^*(f_2) & \cdots & x_N(f_l)x_N^*(f_l) \end{bmatrix} \tag{38}$$

This approach also requires snapshots of data to properly estimate the true CSDM blocks. These snapshots are simple linear combinations as presented in Section 5.2.3. The linear combination of these snapshots results in an expected value of the Super-CSDM shown here:

$$E\langle \hat{X}\hat{X}^{\dagger} \rangle = \frac{1}{R}\sum_{i=1}^{R} \{\hat{X}_i \hat{X}_i{}^{\dagger}\} \tag{39}$$

Then by unstacking the super-vector and applying the IFFT one can potentially obtain the noise reduced version of the original received data.

5.3.3 Space-Time-Frequency Processing Using Cross Wigner-Ville

One approach for utilizing time-frequency distributions is discussed previously in literature [35] where the SVD is used on a single Time-Frequency representation of non-stationary signals. This method does not utilize spatial information available across an array of N receivers. To use the extent of all three dimensions of space-time-frequency, one approach is to construct a matrix that uses this information simultaneously. The use of the Smoothed Pseudo Wigner-Ville distribution lends itself to this methodology quite well, in that the implementation for this Cohen class time-frequency distribution involves the Fourier transform of the autocorrelation (or cross-correlation) to estimate instantaneous frequency (See Chapter 2). Eq. (40) presents the cross Smooth Pseudo Wigner-Ville distribution between two different signals denoted $x_1(t)$ and $x_2(t)$.

$$WV_{x_1x_2}(t,f) = \int_{-\infty}^{+\infty} h(\tau) \int_{-\infty}^{+\infty} g(u-t) x_1(u+\frac{\tau}{2}) x_2^*(u-\frac{\tau}{2}) e^{-j2\pi f\tau}\, \mathrm{d}u\, \mathrm{d}\tau \qquad (40)$$

Where $g(u-t)$ and $h(\tau)$ are the time and frequency smoothing windows, and the inner integral produces a function similar to a time correlation of the signals (analogous to the $\hat{\boldsymbol{X}}\hat{\boldsymbol{X}}^\dagger$ matrix used in the previous approach). The outer integral then takes the Fourier transform of this and produces a cross time-frequency distribution. It is then possible to construct a spatial time frequency distribution (STFD) by stacking these distributions in the same manner and construction of the Super-CSDM presented in Section 5.3.2. These methods are similar in that the blocks of the Super-CSDM are correlations of the array output, likewise the STFD uses the Fourier transform of these correlations to form the time-frequency distribution. The STFD "super" matrix is then formatted as follows:

$$STFD = \begin{bmatrix} WV_{x_1x_1}(t,f) & WV_{x_1x_2}(t,f) & \cdots & WV_{x_1x_N}(t,f) \\ WV_{x_2x_1}(t,f) & WV_{x_2x_2}(t,f) & \cdots & WV_{x_2x_N}(t,f) \\ \vdots & \vdots & \ddots & \vdots \\ WV_{x_Nx_1}(t,f) & WV_{x_Nx_2}(t,f) & \cdots & WV_{x_Nx_N}(t,f) \end{bmatrix} \qquad (41)$$

where each $WV_{x_ix_j}(t,f)$ $(i,j = 1...N)$ represents the discrete matrix blocks. The diagonal blocks of the STFD are the Auto Wigner-Ville distributions and the off-diagonal elements are Cross Wigner-Ville distributions of the receiver signals. This "super" matrix then contains all the inter-element (space) time-frequency information and can now be used for noise reduction.

The noise reduction process flow will now be summarized and the visual representation is shown in Fig. 5.6. First, the array data is recorded across N sensors, and discrete times, t. Then each SPWV and Cross-SPWV is computed for all sensor pairs. These time frequency distributions are then stacked block-wise into the STFD which now has dimensions Nt $\times$ Nf (number of sensors times time samples by number

of sensors times frequency samples). The SVD of the "super" matrix is computed and only the most energetic singular values (which represent the signal subspace) are used to reconstruct a denoised version of the STFD. The diagonal blocks from the reduced STFD are the denoised time-frequency distributions for each sensor.

It is important to note that some important differences of this method, which will be referred to hereafter as the STFD-SVD. This method does not require multiple snapshots for lower noise levels in order to effectively reduce the noise; due to the additional information provided by the inter-element time-frequency process, the STFD has a rank sufficient to perform the SVD to decompose the data into subspaces. Additional snapshots can be used in the same manner as the other methods to improve the performance of the method for higher noise levels. Additionally this method does not project the data onto an estimated CSDM like the previous two method, since the data is directly used to form the noise reduced signal.

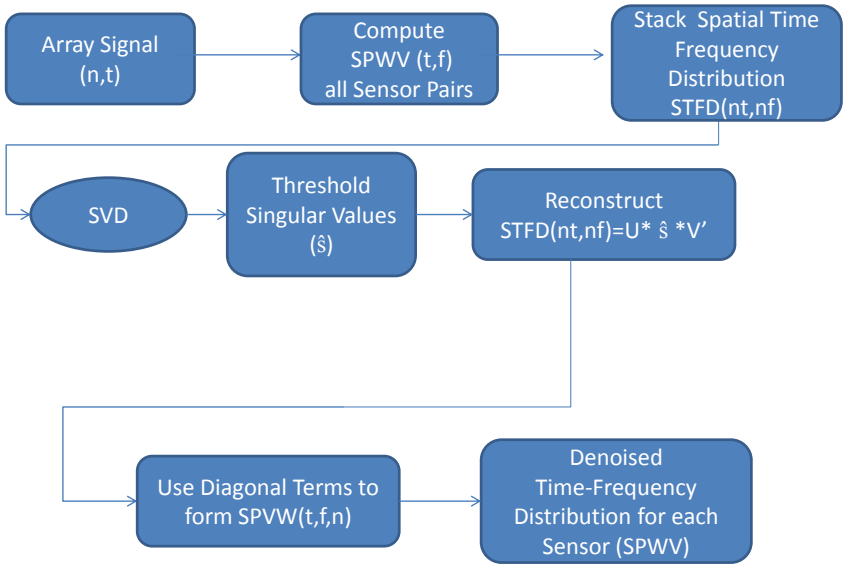

Figure 5.6: Depiction of the space time frequency denoising process flow.

5.4 Numerical Experiment Results

The Doppler experiment introduced at the beginning of this Chapter (presented in Fig. 5.2) will now be used for numerical experiments for a side by side comparison of the three noise reduction methods presented. This section will measure the performance of the methods based on the SNR gain (SNR of denoised signal minus the SNR of the noisy signal both measured from Eq. (32)) for a noise level of additive white Gaussian noise with a standard deviation of $\sigma = 0.5$ added to the baseline signal of a normalized amplitude of 1. For this noise level, the signal is buried within the noise and not easily identified in the time domain (see Fig. 5.3). Additionally, the baseline comparison will be modeled using a source velocity of $V_s = 600$ m/s with the sound speed of air used at $c_0 = 343$ m/s. The average frequency shift between adjacent receivers is calculated to be ≈36 Hz. With the bandwidth of 100 Hz, this results in approximately 64% frequency overlap between adjacent receivers, with the first and last receiver having a difference of about 250 Hz between their respective center frequencies.

5.4.1 Singular Value Selection Methodology

One consideration that arises in the SVD process as stated previously is the selection and separation of the singular values associated with the signal and with the noise subspaces. When there is a high enough SNR in the noisy signal, the singular values drop off rapidly (this behavior is also dependent on the number of snapshots, R, used). However, when the signal is buried in the noise, the delineation is not as clear-cut. For the numerical simulation, this selection is slightly different for each method.

The first single frequency method requires an SVD for each frequency, and therefore the frequencies that contain the signal have larger separation between the signal singular values and noise. As seen in Fig. 5.7a only some of the frequencies show a first singular value with significant value due to the limited bandwidth of the signal

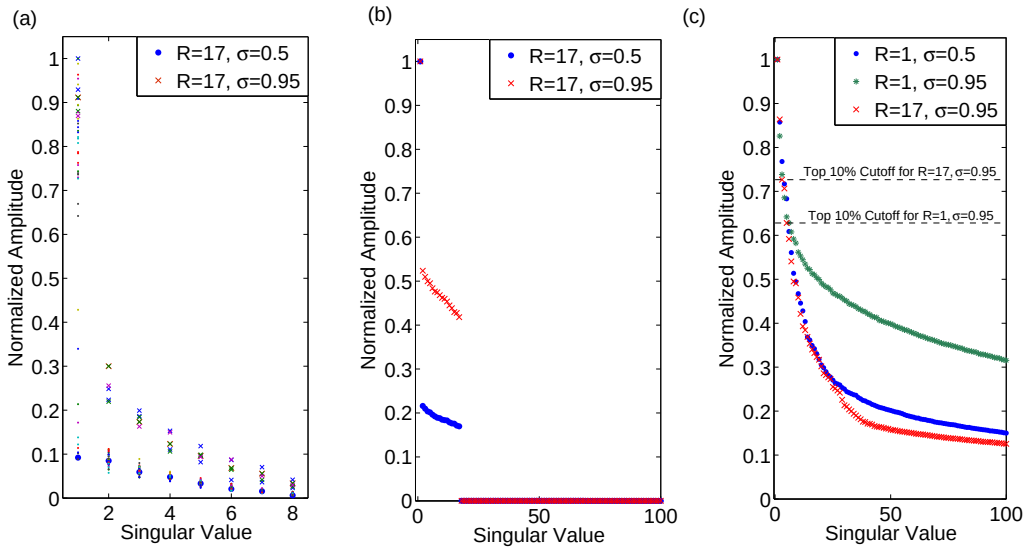

Figure 5.7: Singular value amplitude plotted for each denoising method: (a) single frequency (singular values for each frequency are stacked), (b) cross-frequency, and (c)STFD-SVD. Results shown for the added noise level of $\sigma = 0.5$. The STFD-SVD (c) additionally depicts the singular values for a noise level of $\sigma = 0.95$, for 1 realization (R=1) and 17 realizations (R=17). And depicts the threshold of the top 10% based on energy for these cases.

(100 Hz); therefore, there are frequency bins here that only contain noise. These bins have a low amplitude first singular value. Next, the Cross Frequency method uses the SVD of the Super-CSDM, and again, with a well conditioned CSDM, the separation between the signal and noise is apparent and the first singular value can be used (see Fig. 5.7b).

The separation is not nearly as apparent for the STFD-SVD method as shown in Fig. 5.7c (R=1, $\sigma = 0.5$). In this situation, a threshold can be selected to separate the signal from noise subspace. For the sparse signal and a given noise level, the top 10% of the singular values were chosen to estimate the signal subspace, which results in the first 2 singular values to be used for the $\sigma = 0.5$ case. For a higher noise case ($\sigma = 0.95$), the singular values do not drop off as quickly, and the first 6 singular values lie within the top 10%. The use of the same number of snapshots (R=17) as the previous two methods brings the higher noise level to roughly the same drop off

as the lower noise with a single snapshot.

The first two SVD methods use 17 noise realizations to form snapshots in order to create the projection matrices for denoising an 18^{th} realization. The same noise realization was used for each of the three methods for easy side-by-side comparison and consistency. Each method was successful at reducing the noise floor and thus increasing the SNR. These methods are all applied as blind noise reduction, and thus no information about the signal of non-stationary behavior was required. The STFD did perform better than the first two methods in this case. Additionally, the method performed better with only a single realization at the lower noise level. The measured SNR gain for this baseline noise reduction is 7.8 dB, 10.6 dB, and 13.1 dB for the Single Frequency, Cross-Frequency, and STFD-SVD respectively. The time-frequency representation of these results is shown in Fig. 5.8.

It should be noted that the performance of the STFD-SVD would likely be degraded for signals that are not as sparsely represented in the time-frequency domain. The reason for this thought is seen in Fig. 5.8d in which the noise reduction appears to be a result similar to applying a band-pass filter and time-gate around the signal (though with the STFD, the selection of this time-frequency filter is done automatically via the SVD processing).

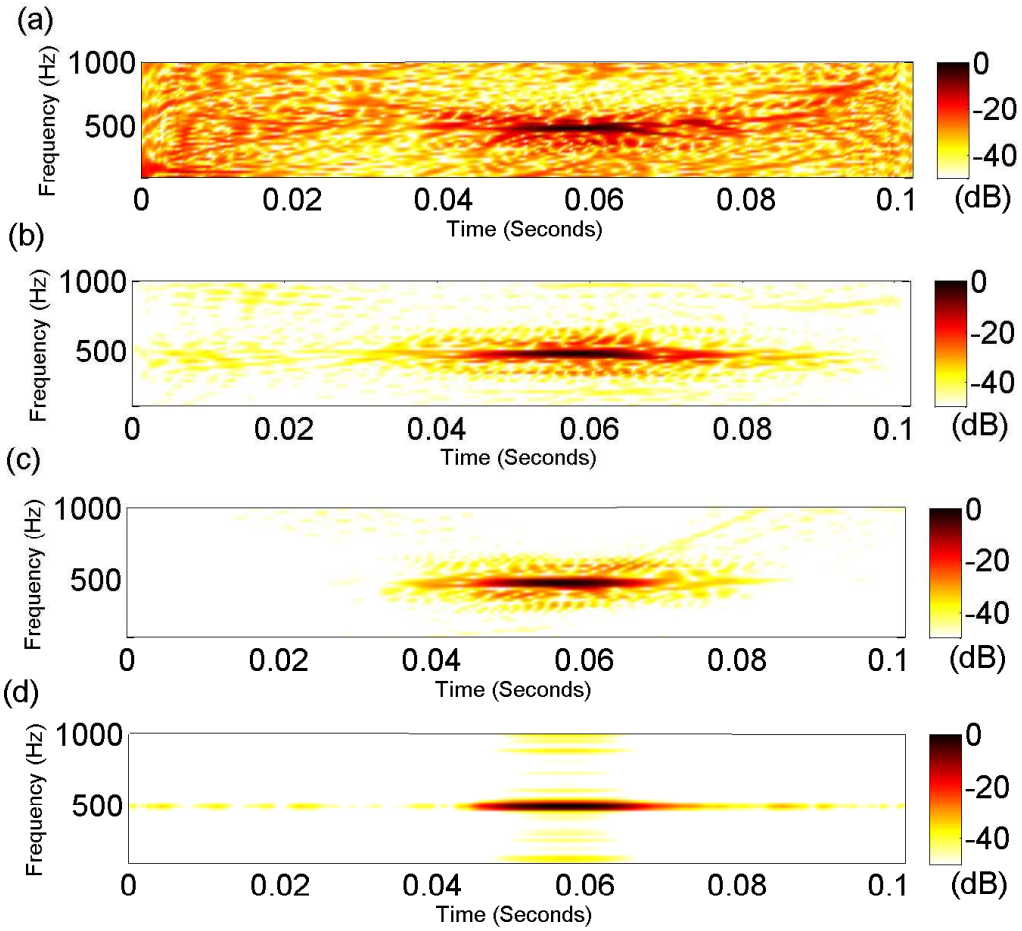

Figure 5.8: Time-frequency representation of sensor 1 from the receiver array shown in Fig. 5.1 with added white noise ($\sigma = 0.5$) and an average frequency overlap between sensors of 64%. The time frequency representation is calculated using the Smoothed Pseudo Wigner-Ville Distribution for (a) noisy signal, (b) single frequency denoised method (R=17), (c) cross-frequency method (R=17), and (d) STFD method (R=1).

5.5 STFD Parameter Study

Since the Space Time Frequency Distribution singular value decomposition method is a new approach to noise reduction, there exists an interest to determine the sensitivity and performance relative to the numerous inputs to the method. A parameter study was conducted to test a variety of input parameters. The parameters chosen to include in the study were: noise level, snapshots, time overlap, frequency overlap, center frequency of the signal, bandwidth of the signal, and the amount of smoothing in the time and frequency domain. The performance of the STFD-SVD method will

be measured based on the SNR gain [SNR(Denoised signal) - SNR(Noisy Signal)]. For the study each parameter was changed from the baseline ($\sigma = 0.5$, R=1, f_c =500 Hz, BW=100 Hz) while holding all other parameters constant, except for the time and frequency overlap study which were interdependent on one another for the denoising performance.

The study results are summarized below:

- Time and frequency overlap, noise level, and snapshots are the most crucial parameters affecting the performance of this method.
- Time and frequency overlap are interdependent, and the performance is best around $70\% - 95\%$ range for both domains.
- The SNR gain decreases with increased noise level due to the reduced ability to separate signal and noise subspaces.
- Increased snapshots increase the performance by effectively reducing noise prior to subspace separation via SVD.

5.5.1 Study Details

The first case of the study uses two high noise levels of additive white Gaussian noise with a standard deviation of $\sigma = 0.5$ and $\sigma = 0.95$. These cases were run through a range of frequency overlaps to determine the performance of all three methods with respect to varying degrees of Doppler shift for two high noise scenarios. The frequency overlap is determined by the frequency shift between adjacent receivers and the signal bandwidth:

$$Overlap\,\% = 100\% - \frac{f_{c2} - f_{c1}}{BW} * 100 \tag{42}$$

where f_{c1} and f_{c2} are the center frequencies of the received signal for sensor 1 and 2 respectively, and BW is the bandwidth of the source signal. Similarly the time

overlap is calculated using the center times and pulse duration.

The STFD-SVD method performs better than the other two methods for the $\sigma = 0.5$ noise level; However, the higher noise level brought the performance of the STFD-SVD down. This is thought to be due to the selection of the singular values, which becomes much more difficult with higher noise levels (see Fig. 5.7).

The noise level directly influences the use of the SVD for separation of the signal and noise subspaces. As shown in Fig. 5.10, the performance of the STFD-SVD method degrades as noise level increases, holding all else equal. This is similar behavior of other subspace methods, due to the difficulty of accurately estimating the signal subspace.

The performance at the higher noise level can be improved by using a higher number of snapshots (equal to those used in the previous methods, R=17). This leads to the next parameter study in which the higher noise level ($\sigma = 0.95$) is used to study the impact of snapshots on the SNR gain. As expected, the increase of snapshots increases the SNR gain to a point, when the signal and noise subspace can be separated.

Further study suggested that the performance or gain of this process seems to rely on the overlap in time and frequency of the signals across the array. These overlaps of time and frequency are mutually dependent on each other as shown in Fig. 5.12. This figure depicts the SNR gain, resulting in lower performance when either time or frequency overlap are less than 80% and 60% respectively. Changing one affects the other, which makes sense, in that if the signal does not share any common time or frequency with the signals on other receivers, little is gained by processing the array data simultaneously. Additionally, it is seen that if the same signal is measured across the array (i.e. 100% frequency overlap), there is slightly less gain, which is thought to be due to loss of the inter-sensor gain brought about by the off-diagonal blocks within the STFD.

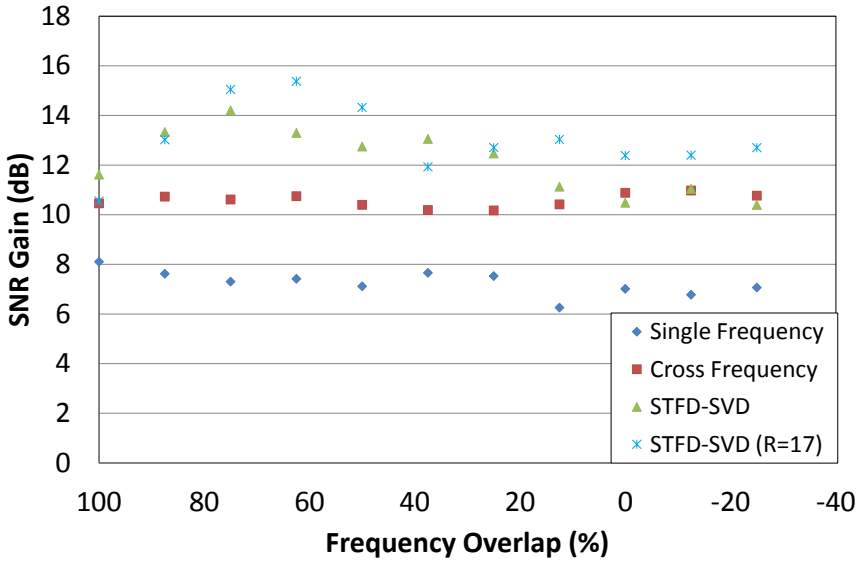

(a)

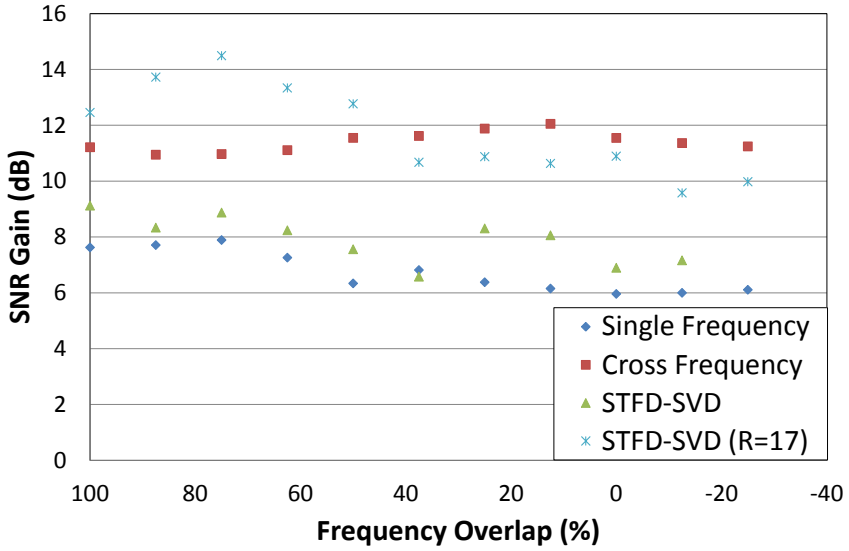

(b)

Figure 5.9: Comparison of SNR gain for the three noise reduction methods for the average array received signals for added white noise at high level of (a) $\sigma = 0.5$ (b) $\sigma = 0.95$, versus frequency overlap for the reference signal ($F_c = 500$ Hz, $BW = 100$ Hz).

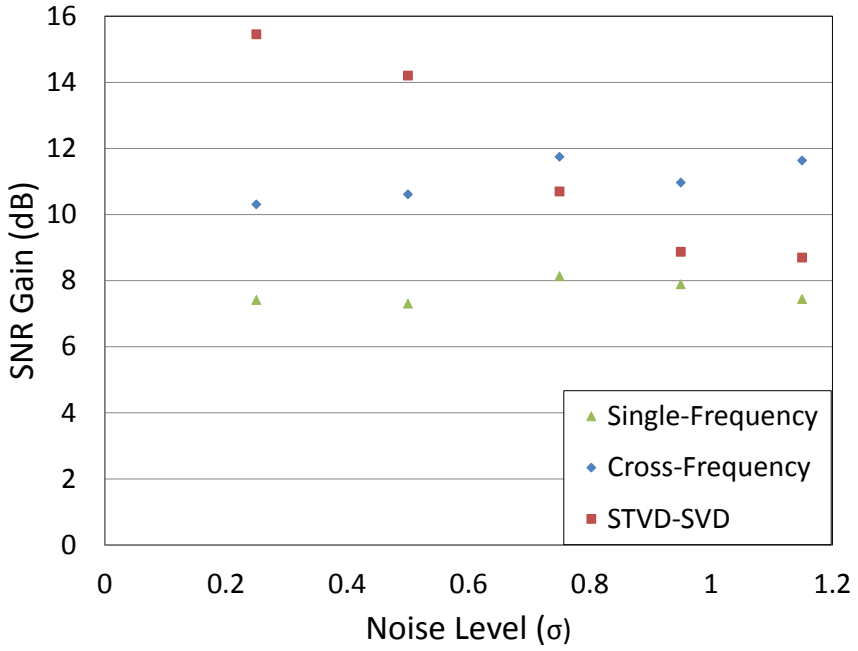

Figure 5.10: Plot of noise level vs SNR gain for the three different methods as labeled in the legend.

Bandwidth had some effect on the SNR gain, though this is thought to be due to the reduced frequency overlap as the frequency shift, bandwidth, and pulse length are dependent on one another. This parameter does not appear to be a critical input for the denoising performance. The change in performance shown in the Fig. 5.13a is due to the change in frequency overlap, not the bandwidth. Further study reveals that both center frequency and time smoothing window size did not drastically affect the STFD-SVD performance. Finally the frequency smoothing window size does not appear to affect the performance of the method until the smoothing becomes larger than the chirp bandwidth. The smoothing window being larger than the chirp results in the performance drop due to the stretching the signal and loss of compact and sparse time-frequency representation (see smoothing selection study in Appendix B).

This study reveals that the STFD-SVD method remains robust to various input parameters and signal behavior. In the certain case of time-frequency overlap of between the 70%-95% range, the method performed its best. Further extension of

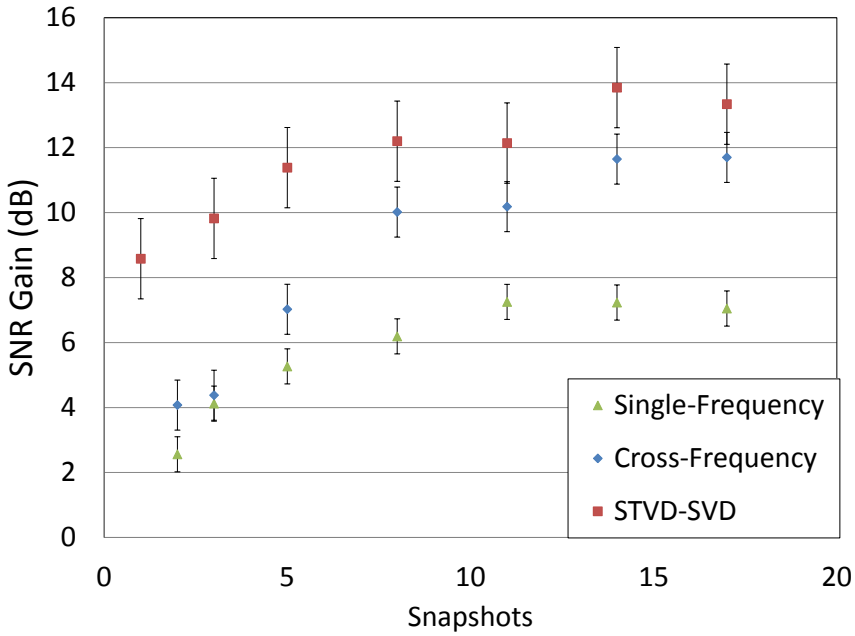

Figure 5.11: Plot of snapshots vs. SNR Gain for a noise level of $\sigma = 0.95$, for the three methods. The STFD-SVD is using the top 10% of the singular values. Error bars displayed are representative of one standard deviation from 10 numerical experiments with different noise realizations for the indicated number of snapshots.

this method could involve the use of a mask to isolate the signal in the time-frequency domain, which could be used as a time-frequency filter. Another method would be to map the two dimensional time-frequency function back to a one dimensional time function using a Wigner-Ville synthesis algorithm [12, 64]. The Wigner-Ville synthesis algorithm presented by Boudreaux et al. [12] is a minimization problem to best approximate a digital signal whose time-frequency representation matches the given time-frequency distribution by a least squares approach. The synthesized signal must be bounded by additional phase information since the synthesis will not result in a unique signal, since multiple signals with different phases may give the same time frequency distribution (i.e. sine and cosine functions have phase offset of $\pi/2$ but present the same time-frequency distribution). These approaches would allow time domain processing to be used on the synthesized version of the denoised signal. This extension will remain as a possible direction for future work.

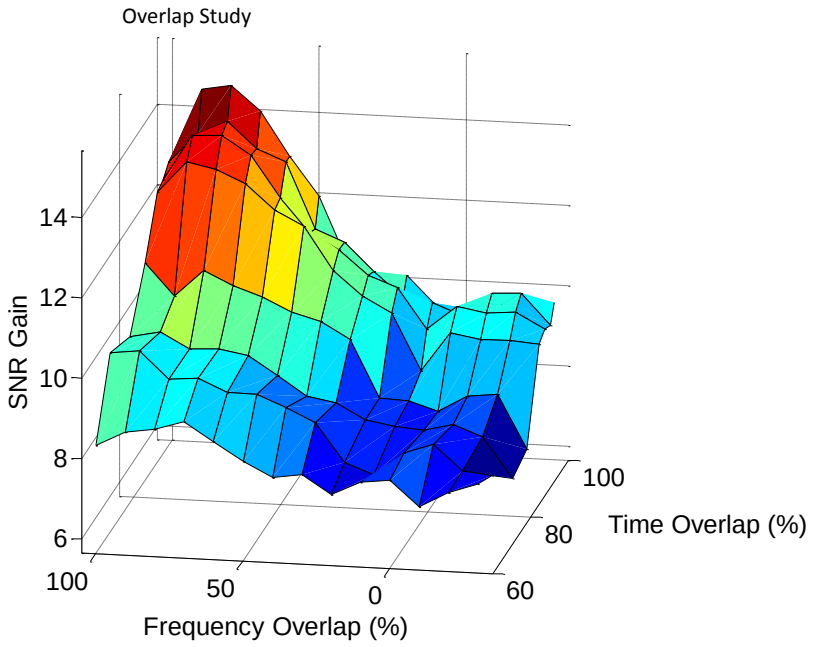

Figure 5.12: Surface plot of the STFD-SVD approach depicting the SNR gain for various combinations of time overlap and frequency overlap from adjacent receivers for the reference signal ($F_c = 500$ Hz, $BW = 100$ Hz,$T_l = 40$ ms).

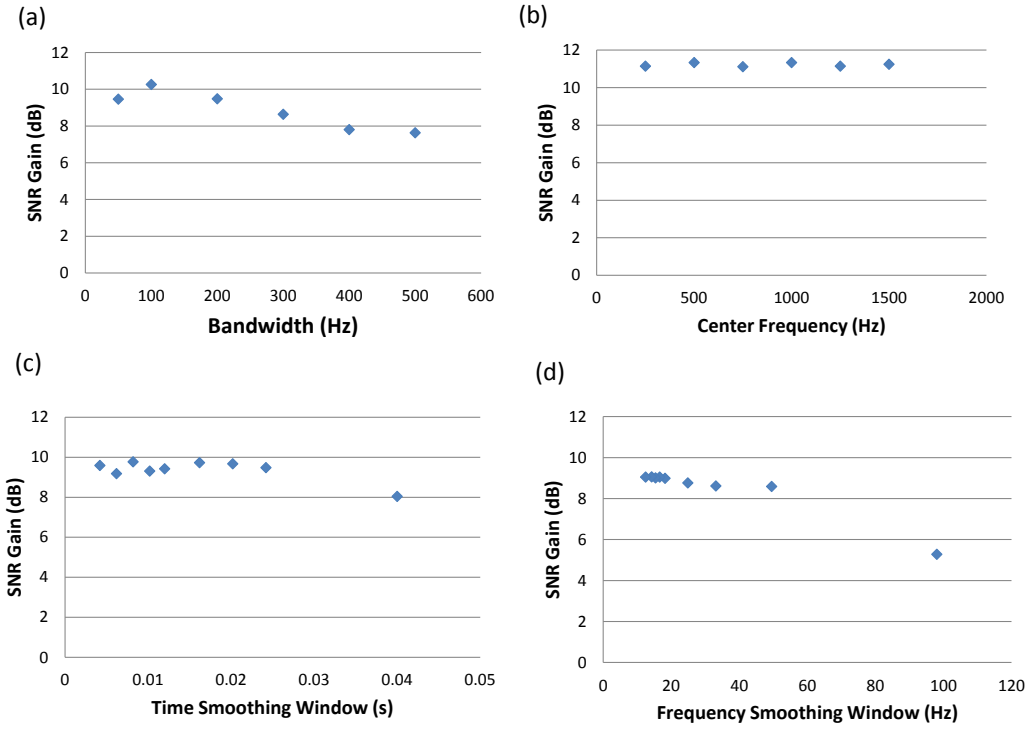

Figure 5.13: Graph results of study for STFD sensitivity to input parameters.

5.6 Application to Experimental Data

In order to test the viability and performance for application beyond simulated data, the STFD-SVD method is applied to the synthetic aperture experiment introduced in Chapter IV. As this experiment was not conducted for the purposes of a noise reduction experiment, additional snapshots are not available to implement the two other methods, and the signal to noise ratio of the experimental data is already fairly high (22.4 dB in time-frequency domain) due to low ambient noise, and preprocessing via Matched Filter. This section the results of the improvement to the SNR will be discussed and some of the factors that influence the results of denoising the experimental data will be discussed.

For consistency, the application to the data will remain a blind noise method though the signal time and frequency content is known. Additionally the signal contains more complex behavior than the previous modeled approach with the signal containing: a broadband specular echo, narrow band MFE, noise, multipath, and reverberation. These added features to the signal are expected to decrease the performance of the SVD approach since the signals are not completely sparse in the time-frequency domain, and are expected to lead to complications with separating singular values that contain the noise and signal. Therefore, care will need to be taken when selecting the singular values to recover a distinguishable signal from the noise.

It was found that choosing the top 20% of singular values was the best threshold for the balance between recovering the signal and maximize the noise reduced from the recorded data. The data set has 400 positions available for creating a synthetic array spaced at 2.5 cm apart. For the denoising purpose 8 elements were selected to create an array over 3 different spacing between elements, (2.5 cm, 10 cm, 50 cm). These spacing to create synthetic arrays were selected in attempt to reduce any coherence of the noise from sensor to sensor created by reverberation, as the further

apart the sensors, the less likely each sensor would record the same diffuse scattering from the environment.

The initial SNR for the noisy signal in the time domain (using Eq. (32)) was 22.4 dB. Using the 8 sensors at the minimum separation distance gave a 2.9 dB increase in the SNR. The further separations with 10 cm and 50 cm resulted in an SNR increase of 4.4 dB and 4.6 dB respectively. This increase in noise reduction performance supports the idea of the correlation of noise playing a role in the denoising. The synthetic array data collection method lends itself to containing uncorrelated noise quite well since the recording is both at different times as well as capable of wide separation in space, so time varying white noise and environment reverberation will have little correlation between sensors.

The time-frequency results from the noise reduction for the 10 cm separation case are shown in Fig. 5.14. The specular echo and its multipath arrivals are seen at times 15.6 and 15.7 ms, followed by the MFE arrival at 16.4 and 16.6 ms. The noise considered here is measured before the arrival of the signal as indicated in Fig. 5.14a. The results reveal that not only is the noise reduced by this approach but additional smoothing of the interference patterns (seen in between the specular arrivals at 15.65 ms) is accomplished with the SVD applied to the Smoothed Pseudo Wigner-Ville.

In conclusion, the STFD-SVD method performs well in the experimental case, where the noise level was cut by over half of the initial value through a blind noise reduction method. Based on this experimental application and modeling results, the method is expected to perform better for narrowband signals and higher noise levels (where the signal is sparse in the time-frequency domain). This should be investigated in future research with simple experiments developed in particular for this approach, which could verify this expectation. The experiment could also be developed to take additional snapshots to allow for the model and experiment validation of the other two methods as well.

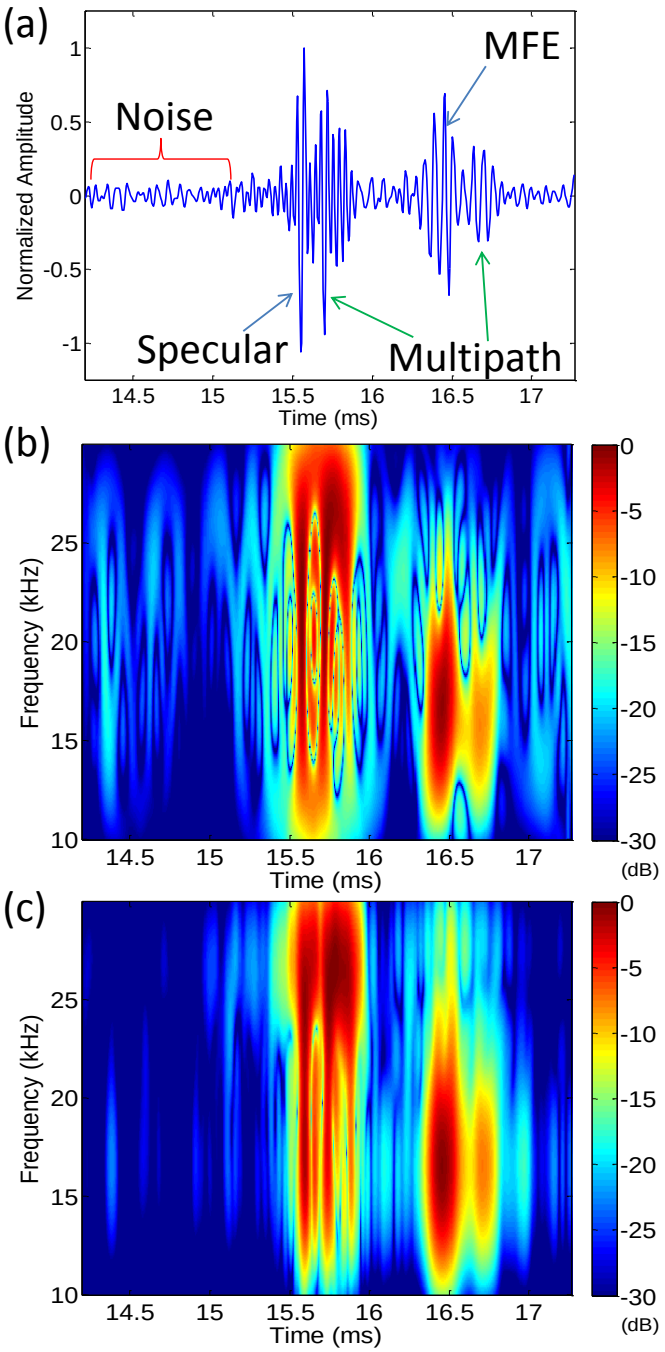

Figure 5.14: Experimental data representations for point of closest approach for monostatic data of spherical shell from the NSWC pond experiment (a)time series (b) Time-frequency noisy signal (c) Time-frequency STFD-SVD data. Experiment setup details are presented in section 4.4.

5.7 Discussion and Summary

The blind source separation of non-stationary signals across an array is a valuable tool in many applications, specifically bistatic detection of elastic echoes (see Chapter III), and as applied in this chapter, an arbitrary frequency shift of a signal along an array of receivers. The non-stationary behavior of the signals require wideband methods for proper treatment of the signal for noise reduction. The STFD-SVD method using the cross Wigner-Ville time-frequency distribution was proposed as an extension to the single and cross-frequency subspace methods. The main benefit of the STFD-SVD method, in addition to its performance, is the ability to achieve blind source separation of a Doppler shifted signal using only a single snapshot for lower noise levels. This becomes important, especially for a Doppler signal, due to the constantly changing Doppler shift (as the source moves) across the array, which can physically limit the number of snapshots available. Further improvement can be achieved for higher noise levels with additional snapshots.

The conclusions and contributions that can be drawn from this research for denoising via the proposed STFD-SVD method are as follows:

- At lower noise levels the STFD-SVD performs as well if not better than single frequency and cross-frequency subspace methods.
- For the higher noise levels, the methods show an SNR gain though the sparse representation of the signal begins to degrade and the SVD approach begins to breakdown, which requires more singular values to represent the signal subspace.
- Time and frequency overlap, noise level, and snapshots are the critical parameters affecting the performance of this method.
- There is a performance increase using the STFD-SVD method for non-stationary signals that have an overlap between ≈70-95% in both time and frequency.

- The time and frequency smoothing windows only weakly affect the performance of the STFD-SVD Method, and only when the smoothing window exceeds the bandwidth of the signal.
- The actual bandwidth and center frequency do not appear to have a significant impact on the performance of the proposed method.
- The STFD-SVD method performs well in the experimental case, where the noise level remaining after the Matched filter processing was cut by over half of the initial value through a blind noise reduction method.

CHAPTER VI

CONCLUSIONS AND FUTURE DIRECTIONS

The goal of research in the field of mine countermeasure efforts can be conveyed in two words: "detection" and "classification." The tools proposed in this research were investigated and developed with the intent to improve these processes, through the use of the elastic echoes from simple elastic targets in both monostatic and bistatic source-receiver configurations.

The monostatic and bistatic behavior of a thin spherical shell at low-mid frequency ranges was thoroughly investigated. From this research it was determined that the elastic echoes from the spherical shell target required methods to account for the varying time-frequency behavior for bistatic measurements. A time-frequency beamformer was found to work to improve signal amplitude across an array, for known time and frequency shifts.

The acoustic imaging of the simple elastic targets was then investigated to determine the limitations and possible improvements of this detection method. It was shown that the elastic echoes are not properly focused with conventional back-propagating methods due to their delayed propagation physical formation. An alternative maximum search method was proposed and applied to simulation and experimental data. The MSM image allowed tracking of the maximum energy across varying focus times, which increased the signal level. However, the MSM image is of limited use due to the loss of time resolution, and therefore requires sufficient angular coverage of a target to be recorded. This limitation also highlights a flaw in using the elastic echoes from more complex shapes, such as a solid cylinder, due to the limited angles at which guided waves can be excited and recorded.

Finally, with the knowledge of the time-frequency behavior of the elastic echoes (analogous to a arbitrary time and frequency shifts), a Space-Time-Frequency blind noise reduction technique was proposed using an SVD subspace methodology. The Space-Time-Frequency Distribution SVD method was implemented for a numerical model of an arbitrary frequency shift law along an array. Furthermore, the STFD-SVD approach was investigated to determine the performance sensitivity to the input parameters selected.

The investigation of the simple spherical shell led to the application and development of several approaches for handling the time-frequency behavior of the elastic echoes observed. The objectives of this research were met by developing methods for improving the detection and classification of a man-made target by means of time-frequency analysis and bistatic enhancement of the elastic echoes from a man-made target.

6.1 Contributions

The main accomplishments and contributions of the research are summarized below:

- The study of the bistatic behavior for the mid-frequency enhancement revealed the occurrence of a time-frequency shift.
- The benefit of using a time-frequency beamformer to enhance detection of the MFE was applied to simulation data.
- The limitations of acoustic imaging (i.e. SAS processing) of guided waves from a spherical shell were investigated.
- The Maximum Search Acoustic Imaging method was introduced and applied to simulation data from a spherical shell and experimental data from a spherical shell and solid cylinder. Limitations and requirements of large angular coverage for imaging of guided waves were discussed.

- Space-Time-Frequency method using the smoothed pseudo Wigner-Ville transform was proposed and investigated as a method for blind noise reduction of non-stationary signals measured on an array.

6.2 Suggested Future Directions

This work has provided additional tools for enhancement and use of the elastic contributions from simple elastic targets. These tools have proven to be useful in the numerical models and a single controlled pond experiment. The results suggest a number of directions for future research to continue this work.

1. The obvious extension is to apply these methods to investigate and study of more complex objects. These should include cylindrical shells and truncated cones, which are representative of modern mine designs.

2. The imaging of the elastic echoes from a spherical shell especially, in the bistatic measurement region, gave promising results when using the MSM imaging for large angular coverage. Further investigation on the use of models that account for the full propagation paths of the guided waves and account for the environmental multipath could be helpful to determine the usefulness of imaging elastic echoes from non-axisymmetric shapes.

3. Finally the blind noise reduction method using the STFD-SVD method seems to have excellent denoising behavior for the cases in which it was applied. Further investigations and extensions to other applications, such as RADAR or speech processing (which contain non-stationary signals) may prove to be fruitful for future research.

APPENDIX A

MODAL EXPANSION COEFFICIENTS

$$A_l^{\mathrm{I}} = -i^l(2l+1)\frac{\begin{vmatrix} a_1 & \alpha_{12} & \alpha_{13} & \alpha_{14} & \alpha_{15} & 0 \\ a_2 & \alpha_{22} & \alpha_{23} & \alpha_{24} & \alpha_{25} & 0 \\ 0 & \alpha_{32} & \alpha_{33} & \alpha_{34} & \alpha_{35} & 0 \\ 0 & \alpha_{42} & \alpha_{43} & \alpha_{44} & \alpha_{45} & \alpha_{46} \\ 0 & \alpha_{52} & \alpha_{53} & \alpha_{54} & \alpha_{55} & \alpha_{56} \\ 0 & \alpha_{62} & \alpha_{63} & \alpha_{64} & \alpha_{65} & 0 \end{vmatrix}}{\begin{vmatrix} \alpha_{11} & \alpha_{12} & \alpha_{13} & \alpha_{14} & \alpha_{15} & 0 \\ \alpha_{21} & \alpha_{22} & \alpha_{23} & \alpha_{24} & \alpha_{25} & 0 \\ 0 & \alpha_{32} & \alpha_{33} & \alpha_{34} & \alpha_{35} & 0 \\ 0 & \alpha_{42} & \alpha_{43} & \alpha_{44} & \alpha_{45} & \alpha_{46} \\ 0 & \alpha_{52} & \alpha_{53} & \alpha_{54} & \alpha_{55} & \alpha_{56} \\ 0 & \alpha_{62} & \alpha_{63} & \alpha_{64} & \alpha_{65} & 0 \end{vmatrix}} \tag{6a}$$

for $l \geqq 1$, and

$$A_0^{\mathrm{I}} = -\frac{\begin{vmatrix} a_1 & \alpha_{12} & \alpha_{14} & 0 \\ a_2 & \alpha_{22} & \alpha_{24} & 0 \\ 0 & \alpha_{42} & \alpha_{44} & \alpha_{46} \\ 0 & \alpha_{52} & \alpha_{54} & \alpha_{56} \end{vmatrix}}{\begin{vmatrix} \alpha_{11} & \alpha_{12} & \alpha_{14} & 0 \\ \alpha_{21} & \alpha_{22} & \alpha_{24} & 0 \\ 0 & \alpha_{42} & \alpha_{44} & \alpha_{46} \\ 0 & \alpha_{52} & \alpha_{54} & \alpha_{56} \end{vmatrix}}. \tag{6b}$$

Using the abbreviations $x=kR$, $x_L=k_LR$, $x_T=k_TR$, $y=k(R-\Delta)$, $y_L=k_L(R-\Delta)$, and $y_T=k_T(R-\Delta)$, the elements of the determinants are given by

$$a_1 = j_l(x)\rho_{\mathrm{I}}/\rho_{\mathrm{II}}, \tag{7a}$$

$$a_2 = x j_l'(x), \tag{7b}$$

$$\alpha_{11} = h_l^{(1)}(x)\rho_{\mathrm{I}}/\rho_{\mathrm{II}}, \tag{7c}$$

$$\alpha_{21} = x h_l^{(1)\prime}(x), \tag{7d}$$

$$\alpha_{12} = [\lambda_{\mathrm{II}} j_l(x_L) - 2\mu_{\mathrm{II}} j_l''(x_L)]/(\lambda_{\mathrm{II}} + 2\mu_{\mathrm{II}}), \tag{7e}$$

Figure A.1: Modal expansion coefficients taken from Eq. (6a) and Eq. (6b) in paper by Goodman and Stern [31].

$$\alpha_{22}=x_L j_l'(x_L), \tag{7f}$$

$$\alpha_{12}=2[x_L j_l'(x_L)-j_l(x_L)], \tag{7g}$$

$$\alpha_{42}=[\lambda_{11} j_l(y_L)-2\mu_{11} j_l''(y_L)]/(\lambda_{11}+2\mu_{11}), \tag{7h}$$

$$\alpha_{82}=y_L j'(y_L), \tag{7i}$$

$$\alpha_{62}=2[y_L j_l'(y_L)-j_l(y_L)], \tag{7j}$$

$$\alpha_{13}=-2l(l+1)x_T^{-2}[x_T j_l'(x_T)-j_l(x_T)], \tag{7k}$$

$$\alpha_{23}=l(l+1)j_l(x_T), \tag{7l}$$

$$\alpha_{33}=x_T^2 j_l''(x_T)+(l+2)(l-1)j_l(x_T), \tag{7m}$$

$$\alpha_{43}=-2l(l+1)y_T^{-2}[y_T j_l'(y_T)-j_l(y_T)], \tag{7n}$$

$$\alpha_{63}=l(l+1)j_l(y_T), \tag{7o}$$

$$\alpha_{63}=y_T^2 j_l''(y_T)+(l+2)(l-1)j_l(y_T), \tag{7p}$$

$$\alpha_{14}=[\lambda_{11} n_l(x_L)-2\mu_{11} n_l''(x_L)]/(\lambda_{11}+2\mu_{11}), \tag{7q}$$

$$\alpha_{24}=x_L n_l'(x_L), \tag{7r}$$

$$\alpha_{34}=2[x_L n_l'(x_L)-n_l(x_L)], \tag{7s}$$

$$\alpha_{44}=[\lambda_{11} n_l(y_L)-2\mu_{11} n_l''(y_L)]/(\lambda_{11}+2\mu_{11}), \tag{7t}$$

$$\alpha_{54}=y_L n_l'(y_L), \tag{7u}$$

$$\alpha_{64}=2[y_L n_l'(y_L)-n_l(y_L)], \tag{7v}$$

$$\alpha_{15}=-2l(l+1)x_T^{-2}[x_T n_l'(x_T)-n_l(x_T)], \tag{7w}$$

$$\alpha_{25}=l(l+1)n_l(x_T), \tag{7x}$$

$$\alpha_{35}=x_T^2 n_l''(x_T)+(l+2)(l-1)n_l(x_T), \tag{7y}$$

$$\alpha_{45}=-2l(l+1)y_T^{-2}[y_T n_l'(y_T)-n_l(y_T)], \tag{7z}$$

$$\alpha_{55}=l(l+1)n_l(y_T), \tag{7aa}$$

$$\alpha_{65}=y_T^2 n_l''(y_T)+(l+2)(l-1)n_l(y_T), \tag{7bb}$$

$$\alpha_{46}=j_l(y)\rho_{11}/\rho_{11}, \tag{7cc}$$

$$\alpha_{56}=y j_l'(y). \tag{7dd}$$

Figure A.2: Additional details of Modal Expansion coefficients taken from Eq.(6a) and Eq. (6b) in paper by Goodman and Stern [31].

APPENDIX B

SMOOTHED PSEUDO WIGNER VILLE SMOOTHING SELECTION

B.1 Smoothing Window Selection

Stated in Chapter II, the benefit of using the SPWV analysis is the ability to select the time and frequency smoothing windows separately. This does present additional complexity in choosing the appropriate type and size of the window for optimal time and frequency localization. In order to select the window size, further study was conducted on a representative temporal response for a spherical shell computed from Fig. 2.3. This was selected to investigate the appropriate amount of smoothing for the best visualization of the time-frequency distribution of the echoes from a shell.

The initial step for selecting a window size was to choose the shape of smoothing window. For this, five types of standard smoothing windows were overlaid to compare the shape of each windowing function (see Fig. B.1). It was decided that the Hann type of window was a good compromise between the sharpness of the Kaiser window, and the broadness of the Hamming window. Additionally, for the given structure of the scattered field from a shell, the Hann window gave a time frequency representation that could suppress the interference patterns of the higher order transform and maintain a higher time frequency resolution than standard STFT technique.

Once the type of window was selected, an empirical study was conducted to evaluate the effect of broad vs. narrow smoothing windows in both time and frequency for the given SPWV representation. These results are shown in Fig. B.2. As shown, when little smoothing is used, the results revert to a standard Wigner-Ville distribution in which the interference patterns are prevalent. The goal of getting the smoothing

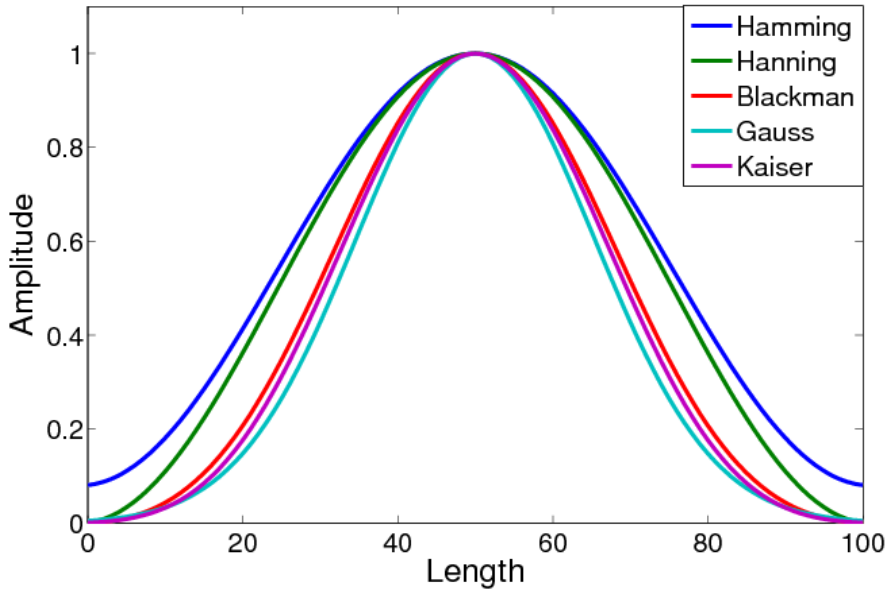

Figure B.1: Overlay of standard amplitude smoothing windows including Hann, Hamming, Blackman, Gauss, and Kaiser. Each window has length of 100 points, and the defining parameters of the Gaussian window and the Kaiser window were selected to be $\alpha = 0.005$, and $\beta = 3\pi$ respectively.

windows set at a desired width in time domain is a balance between suppressing the interference patterns and retaining a good time-frequency localization of a signal. For the given response of the shell, the time smoothing window was determined to be a Hann window of 0.2 ms (205 points) and a frequency smoothing window was a Hann window of 192 Hz (171 points). This is not to say that these are the resolution limits (which are 0.0012 ms and 210 Hz), but rather the length of smoothing window. The results of appropriately selected smoothing windows for the SPWV representation are shown in Fig. B.2. Though this empirical method is not readily applied in the field, one can select smoothing windows a priori that are appropriate for the targets, and noise anticipated for a given environment.

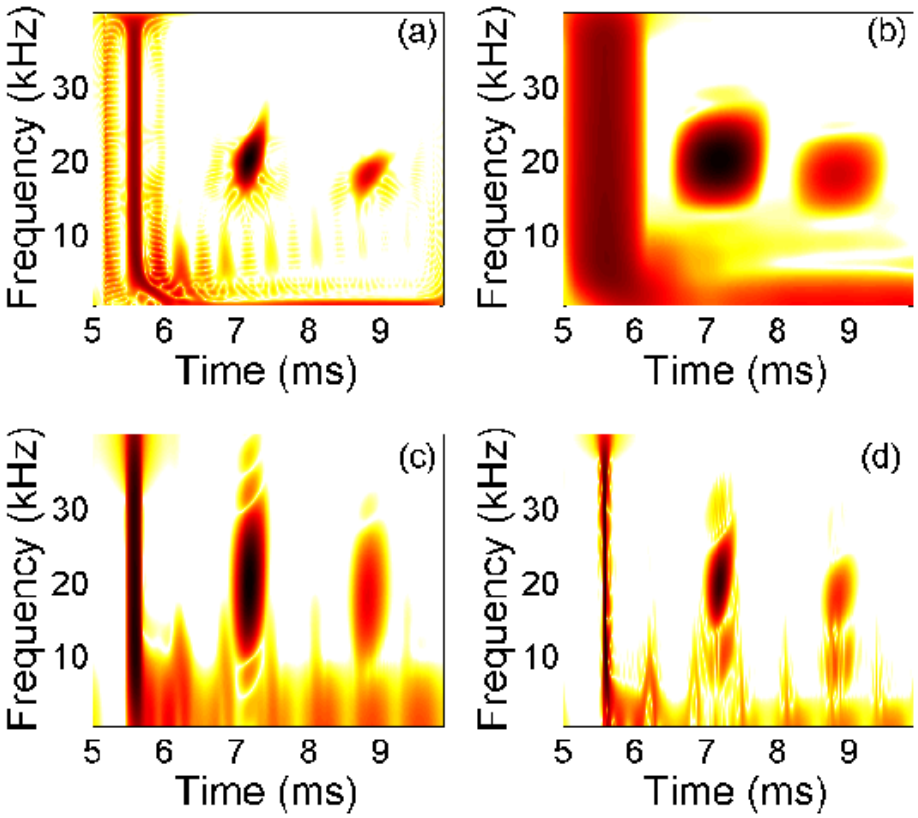

Figure B.2: SPWV with different Hann window sizes with double (wide) and half (narrow) the length of reference smoothing window (reference window sizes are 205 points in time and 171 points in frequency): (a) narrow window in frequency domain, (b) narrow window in time domain, (c) broad window in frequency domain, and (d) broad window in time domain.

APPENDIX C

IMAGE METHOD FOR EXPERIMENTAL OBSERVATIONS

For continuous inhomogeneities, deviation from the propagation predicted by the free-space Green's function is referred to as refraction (bending of rays). For discontinuities in the medium, the deviation is referred to as diffraction or scattering. These mechanisms are both forms of wave propagation. However, typically, they are treated differently.

Ray theory provides a high-frequency approximation to the Helmholtz equation. It is an intuitive approach, which significantly predates its formal mathematical formulation; the original concept of rays is attributed to Euclid in the 3rd century BC. Rays have been used extensively for modeling electromagnetic and acoustic wave propagation [41]. The ray theory is derived in Appendix A2, and the practical implementation of an acoustic ray in the quantitative ray theory model uses the ray-tracing technique to determine the distance and path traveled by individual waves interacting with the shell. For propagation to and from the target, this simple ray method will be used in conjunction with the free space Green's function.

To account for this simplified half-space, an image method is used [41](pg. 100-102). This method allows the use of the free space Green's function by accounting for the half-space reflection by the addition of image sources or receives. This method is depicted in Fig. C.1, where there is an image source/receiver and the arrows indicate the path to or from the receiver or source respectively. The four propagation paths identified correspond physically to the (1 to 2) Source-Target-Receiver, Source-Target-Bottom-Receiver (1 to 4), Source-Bottom-Target-Receiver (3 to 2),

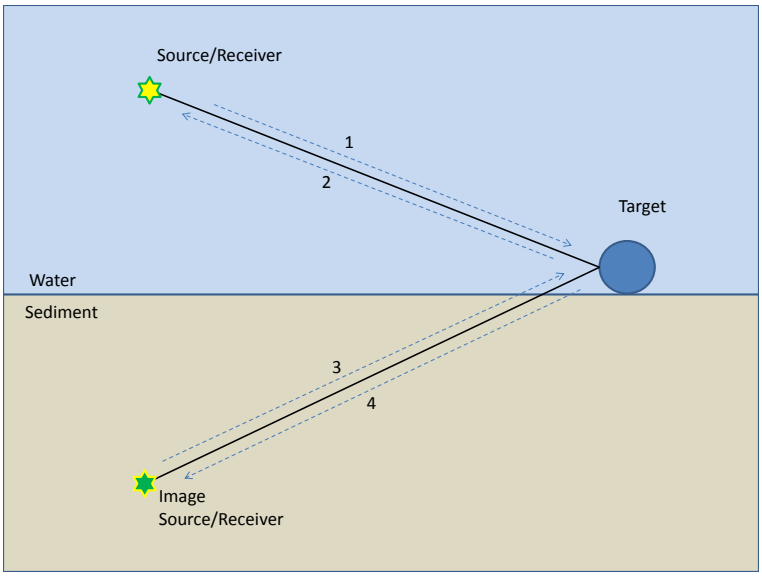

Figure C.1: Ray Method proposed to model the multipath propagation between Source, Target, and Receiver.

and Source-bottom-Target-Bottom-Receiver (3 to 4). The response can then be calculated by the linear summation of each individual target-receiver path combination. As the method does not account for the amplitude loss due to bottom penetration, only single bounce paths which arrive at the same time (1-4 and 3-2) will be input into the model (double bottom bounce multipath receiver is assumed to be low in amplitude).

APPENDIX D

MATLAB CODE

D.1 Numerical Shell Model

```
% spherical Functions of Bessel + derived first + derived seconds.
%
%
% Definition:
% the spherical functions of Bessel of 1st and 2nd species of order m,
% noted respectively j_m and y_m, are the particular solutions of
% the diffentielle equation of Bessel written in spherical co-ordinates:
%
% f' ' + (2/z)*f' (z) + (1 m(m+1)/z^2)*f = 0; F = f(z), Z = alpha*r.
%
% syntax of the function: [ J, y, jp, YP, js, ys ] = bes_prim_sec_hs(M, x)
%
% M: a vector (column preferably) containing the orders
% whole sussecssifs ' m_i' of the spherical functions of Bessel.
% X: a scalar % J: vector column containing the functions of Bessel of here
% species of orders ' m_i' as in point X, j_m_i(x).
% y: vector column containing the values of the functions of
% Bessel spherical of 2nd species of orders ' m_i' at the point
% X, y_m_i(x). % jp: vector column containing the values of derived from
% spherical functions of Bessel of 1ere species of orders ' m_i' to
% not X, I _m_i(x).
% YP: vector column containing the values of derived from
% spherical functions of Bessel of 2nd species of orders ' m_i' to
% not X, y' _m_i(x). % js: vector column containing the values of derived
```

```
% seconds from the functions of Bessel of 1ere species of orders
% ' m_i' as in point X, I ' _m_i(x).
% ys: vector column containing the values of derived
% seconds from the functions of Bessel of 2nd species of orders
% ' m_i' as in point X, y' ' _m_i(x).

function [j,y,jp,yp,js,ys]= bes_prim_sec_hs(M,x)
[m,n]=size(M);

if n > 1 & m > 1
  disp('Error, M must be a vector column');
end

if n > 1 | m == 1,
  M=M';
end

ord=[M ; max(M)+1];
long=length(ord);

% Formulas binding the spherical functions of Bessel to the functions of
% Bessel normals (valid for the functions of 1st species like
% for the functions of 2nd species): % j_m(z) = sqrt(pi/(2z))*J_(m+1/2)(z)
% j(small): spherical function of Bessel
% J(capital letter): normal function of Bessel
j_temporaire=sqrt(pi/(2*x))*besselj((ord+0.5), x);
y_temporaire=sqrt(pi/(2*x))*bessely((ord+0.5), x);
j=j_temporaire(1:long-1);
y=y_temporaire(1:long-1);

% Relation of recurrence for the derivative 1st:
% z*j' _m(z) = m*j_m(z)-z*j_(m+1)(z)
```

```
% This formula is valid also for y_m(z).
aux1=ord(1:long-1)./x;
jp=aux1.*j-j_temporaire(2:long);
yp=aux1.*y-y_temporaire(2:long);
% Relation of recurrence for the derivative second:
% z^2*j' ' _m(z) = (m(m+1)-z^2)*j_m(z)-2*z*j' _m(z)
% This formula is valid also for y_m(z).
aux=((M.*(M+1))./x.^2)-1;
js=-(2*jp./x)+aux.*j;
ys=-(2*yp./x)+aux.*y;



%       Acoustic Scattering by a Spherical Shell
% for rap1=[0.8,0.85,.9,.925,.95,.96,.975,.98,.99];
        global file
% file =['marston_shell.txt'];
file =['nswc1.txt'];
%file =['exp1.txt'];
% file =['thinnest_shell.txt'];
%file =['plastic_filled_shell.txt'];%animation paramter
clc;
disp(['Experiment File: ',file]);

readfile;    %Read Parameters file.
% rap=rap1;
% b=rap*a;
sweep_theta=[90:270];
sweep_dist=10;
%  sweep_theta=[180:1:360];%animation paramters
% sweep_dist=[0.515:.025:2];
%%
%----------    First and Second Lame Coefficient         ----------------%
```

```
% Observation medium ("OUTSIDE")
 cl1=cl1-0.05*cl1/40/pi/log10(exp(1))*i;
% cl2=cl2-0.2*cl2/40/pi/log10(exp(1))*i;
% cl3=cl3-0.35*cl3/40/pi/log10(exp(1))*i;
  mu1 =    rho1*ct1^2;
  lamda1 = rho1*cl1^2-2*mu1;

% SHELL
  mu2    =    rho2*ct2^2;
  lamda2 = rho2*cl2^2-2*mu2;
%-------------------------------------------------------------------------%
jkr=[];ykr=[];
%phi1=[];
reduced_freq=[];
ent=0;
cnt_freq=0;
for f=fmin:df:fmax
    %clc;disp(['Estimated % Completed: ',num2str(f/fmax*100,3),' %']);
    cnt_freq=cnt_freq+1;
  omega =  2*pi*f;           % pulsation
  K     =  omega/cl1;        %WAVENUMBER in SURROUNDING medium
  Kl    =  omega/cl2;        %Longitudinal WAVENUMBER in the shell
  Kt    =  omega/ct2;        %Transverse WAVENUMBER in the shell
  X     =  K*a;              %Reduced frequency. Surrounding medium,
  Xl    =  Kl*a;             %Longitudinal Reduced frequency. Shell.
  Xt    =  Kt*a;             %Transverse Reduced frequency. Shell.
  Y     =  omega/cl3*b;     % WAVENUMBER MEDIUM (III) INSIDE the shell
  Yl    =  Kl*b;
  Yt    =  Kt*b;
  reduced_freq=[reduced_freq X];

  ord = (0:1:nb_mode)';
```

```
%   Bessel Function. Also First and Second derivative :

    [jX,yX,jpX,ypX,jsX,ysX ]      = bes_prim_sec_hs(ord,X) ;
    [jXl,yXl,jpXl,ypXl,jsXl,ysXl ]= bes_prim_sec_hs(ord,Xl);
    [jXt,yXt,jpXt,ypXt,jsXt,ysXt ]= bes_prim_sec_hs(ord,Xt);
    [jY,yY,jpY,ypY,jsY,ysY ]      = bes_prim_sec_hs(ord,Y) ;
    [jYl,yYl,jpYl,ypYl,jsYl,ysYl ]= bes_prim_sec_hs(ord,Yl);
    [jYt,yYt,jpYt,ypYt,jsYt,ysYt ]= bes_prim_sec_hs(ord,Yt);
    cnt_r=0;
    for dist_r=sweep_dist
        cnt_r=cnt_r+1;
        [jkr(:,cnt_freq,cnt_r),ykr(:,cnt_freq,cnt_r),...
            jpkr,ypkr,jskr,yskr ]= bes_prim_sec_hs(ord,(K*dist_r)) ;
    end

% Hankel Functions.

    h1X  = jX  + i*yX  ;
    h1pX = jpX + i*ypX ;
    h1sx = jsX + i*ysX ;

%----------------DETERMINANT PARAMETES-----------------------------------------------

  a11 = rho1/rho2*h1X;
  a12 = (lamda2*jXl-2*mu2*jsXl)/(lamda2+2*mu2) ;
  a13 =  -2*ord.*(ord+1).*(Xt*jpXt-jXt)/Xt^2;
  a14 = (lamda2*yXl-2*mu2*ysXl)/(lamda2+2*mu2);
  a15 =  -2*ord.*(ord+1).*(Xt*ypXt-yXt)/Xt^2;
  %a16 =0;

  a21 = X*h1pX;
```

```
a22 = Xl*jpXl;
a23 = ord.*(ord+1).*jXt;
a24 = Xl*ypXl;
a25 = ord.*(ord+1).*yXt;
%a26 = 0;

%a31 = 0;
a32 = 2*(Xl*jpXl-jXl);
a33 =  (ord+2).*(ord-1).*jXt+Xt^2*jsXt;
a34 = 2*(Xl*ypXl-yXl);
a35 =(ord+2).*(ord-1).*yXt+Xt^2*ysXt;
a36 =zeros(nb_mode,1);

%a41 = 0;
a42 = (lamda2*jYl-2*mu2*jsYl)/(lamda2+2*mu2);
a43 =  -2*ord.*(ord+1).*(Yt*jpYt-jYt)/Yt^2;
a44 = (lamda2*yYl-2*mu2*ysYl)/(lamda2+2*mu2);
a45 = -2*ord.*(ord+1).*(Yt*ypYt-yYt)/Yt^2;
a46 = jY*rho3/rho2;

%a51 =0;
a52 = Yl*jpYl;
a53 = ord.*(ord+1).*jYt;
a54 = Yl*ypYl;
a55 = ord.*(ord+1).*yYt;
a56 = Y*jpY;

%a61 =0;
a62 = 2*(Yl*jpYl-jYl);
a63 = (ord+2).*(ord-1).*jYt+Yt^2*jsYt;
a64 = 2*(Yl*ypYl-yYl);
a65 = (ord+2).*(ord-1).*yYt+Yt^2*ysYt;
```

```
  %a66 = 0;

  a1 =jX*rho1/rho2;
  a2 =X*jpX;

  %%Expression of the scalar potential (phi1) associated with the scattered
  %%pressure field by the spherical shell.
Al1=[];
%Pl_theta=genpol(nb_mode,cos(theta_rd))';%%Create Legendre Polynomial
    for l=1:nb_mode+1
        if l==1
            dl=[ a11(l) a12(l)  a14(l)    0    ; ...
                 a21(l) a22(l)  a24(l)    0    ; ...
                  0     a42(l)  a44(l)  a46(l) ; ...
                  0     a52(l)  a54(l)  a56(l)];
        else
              dl= [ a11(l) a12(l) a13(l) a14(l) a15(l)   0   ; ...
                    a21(l) a22(l) a23(l) a24(l) a25(l)   0   ; ...
                     0     a32(l) a33(l) a34(l) a35(l)   0   ; ...
                     0     a42(l) a43(l) a44(l) a45(l) a46(l); ...
                     0     a52(l) a53(l) a54(l) a55(l) a56(l); ...
                     0     a62(l) a63(l) a64(l) a65(l)   0  ];
        end

         aux=dl;
         aux(1,1)=a1(l);
         aux(2,1)=a2(l);
         dl1=aux;
         Al1=[Al1;(- i^l*(2*l+1)*det(dl1)/det(dl))];
    end
    Al2(:,cnt_freq)=Al1;
end
```

```
Pole=sum(Al1);
%

clear Al1 dl1 aux dl a2 a1 a65 a64 a63 a62 a56 a55 a54 a53 a52 a46 a45 a44 a43 a42 a3
    a33 a32 a25 a25 a24 a23 a22 a21 a15 a14 a13 a12 a11 h1sx h1X jX yX jpX ypX jsX ys
    ysXl jXt yXt jpXt ypXt jsXt ysXt jY yY jpY ypY jsY ysY jYl yYl jpYl ypYl jsYl ysY
    ysYt jpkr ypkr jskr yskr frequency dist theta K Kl Kt X Xl Xt Y Yl Yt...
    alpha0_rd b cl1 cl2 cl3 ct1 ct2 ct3 ent f h1pX l lamda1 lamda2 mu1 mu2 omega ord
    reduced_freq rho1 rho2 rho3 s z;

phi_all=zeros(length(sweep_theta),(fmax/df),length(sweep_dist));
cnt_theta=0;
%phi1=zeros(1,cnt_freq);
for theta=sweep_theta
    clc;theta
    cnt_theta=cnt_theta + 1;
    theta_rd=theta*pi/180;
    Pl_theta=genpol(nb_mode,cos(theta_rd))';%%Create Legendre Polynomial
    for dist=1:cnt_r
       for frequency=1:cnt_freq
        phi1l=nansum(Pl_theta.*Al2(:,frequency).*(jkr(:,frequency,dist)+i*ykr(:,frequ
%         phi1_modes=(Pl_theta.*Al2(:,frequency).*(jkr(:,frequency,dist)+i*ykr(:,freq
        %phi1(1,frequency)=phi1l;
        phi_all(cnt_theta,frequency,dist)=phi1l;
%         phi_all_modes(:,cnt_theta,frequency,dist)=phi1_modes;
       end
    end
end
clear jkr ykr Al2
phi_all(:,1)=0;
clc;disp(['!!!Done!!!']);
```

```
%    Legendre Polynomial for zero order.
%

%
%     P[n+1](z)=1/(n+1)*((2n+1)*z*P[n](z)-n*P[n-1](z)


function [p] = genpol(deg,x)

%on initialize
p(1) = 1;


if deg > 0,
    p(2) = x;

    if deg ≥ 2,

        for l = 3:deg+1
        p(l) = ((2*l-3)*x*p(l-1)-(l-2)*p(l-2))/(l-1);
        end

    end

end


%%%
% f1=1;
% f2=800000;
% df=200;
 f1=1;
```

```
 f2=100000;
 df=20;

Fs=df;
Fe=round(f2*10.5/Fs)*Fs;
Ts=1/Fe;N=1/Fs/Ts;T=N*Ts;

freq=[0:N-1]/N/Ts;
Ifreq=find(freq≥f1 & freq≤f2+df/10);

%%%%For Filtering
 Fmin=0;
 Fmax=f2/2;
%Fmin=1e3;
%Fmax=800e3;
Ifilter=find(freq(Ifreq)≥Fmin & freq(Ifreq)≤Fmax);

time=[0:N-1]*Ts;
c0=1500;zTARG=100;L=200;
for i=1:length(phi_all(:,1))
phi1=phi_all(i,:);
phi1(1)=0;
Kij=zeros(size(freq));
Kij(Ifreq(Ifilter))=conj(phi1(Ifilter)).*hanning(length(Ifreq(Ifilter))).';
%FP(:,jj).*Prod.*hanning(length(Ifreq));
P=real(ifft(Kij));

%freq_int1=[Fmin  Fmax];  [BB1,AA1]=butter(4,[freq_int1]/Fe*2);
%Pfil=filtfilt(BB1,AA1,P);
%%%%%%%%%%
%find(isnan(phi1)==1)
% figure(2);clf;%hold on
```

```
% %subplot(2,1,1)
% plot(time,P)
% title(['Receiver Angle ',int2str(sweep_theta(i)),' '])
% axis tight
% drawnow
% pause(.05)
 Irec=find(time>0.019&time≤0.029);
% Irec=find(time≥5e-3&time≤3e-2);
Pall(:,i)=P(Irec);%.*hanning(length(P(Irec))).';
% subplot(2,1,1);plot(time,P);
% subplot(2,1,2);plot(time(Irec),Pall(:,i));
% drawnow
% pause(.25)
IDX=find(abs(Pall(:,i))==max(abs(Pall(:,i))));
%P_spec(:,i)=Pall(:,i)*0;
%P_spec([IDX-50:IDX+50],i)=Pall([IDX-50:IDX+50],i);
end
clear IDX
% for i=1:length(P_spec(1,:))
%  [res,lags]=xcorr(P_spec(:,find(sweep_theta==180)),P_spec(:,i),'coeff');
%     IDX=lags(find(res==max(res)));
%     Pall_sft(:,i)=circshift(Pall(:,i),IDX);
% end
% Pall_old=Pall;
% Pall=Pall_sft;
% clear Pall_sft IDX res lags
%     noise=wgn(length(Pall(:,1)),1,-90);
% for i=1:length(Pall(1,:))
%     Pall(:,i)=awgn(Pall(:,i),-5,'measured');
% end
%%2D plot
%MM=max(max(Pall));
```

```
%figure(1);clf;hold on
%imagesc(time(Irec),sweep_theta,20*log10(abs(Pall)'/MM))
%caxis([-60 0]);colorbar;
if 1==0
    %% WV ANALYSIS
%%%%^^^^^^^^^^^^^^^^^^^^^^^^^^^^^^^^^^^^^^^^^^^^^^^^^^^^^^^^^^^^^^^^^^^^^^
%%%%^^^^^^^^^
%%%%%%%TIME-FREQUENCY ANALYSIS
%%%%%%%%%%%%%%%%%Time Frequency analysis;
      addpath('C:\Program Files\MATLAB\R2007a\toolbox\tftb-0.1\mfiles')
%%%%%%%%%%%%For Time Frequ Analysis
%%Select one angle
for Iang=1:length(sweep_theta)
    %pause
%Iang=find(sweep_theta==0);

%%Downsample to reduce the number of time samples to minimum necessary;
RATE=3;%round(Fe/Fmax/4);
FeNEW=Fe/RATE;
TsNEW=1/FeNEW;
DATA=decimate(Pall(:,Iang),RATE);%.*hanning(length(Pall(:,Iang))/RATE+1);
Nnew=length(DATA);
timeNEW=[0:Nnew-1]*TsNEW; % redefine time axis
Istart=min(find(DATA≥(max(DATA))))-50;  %[500:830]; %%Select a time-window
timeNEW=timeNEW-timeNEW(Istart);
% Istart=min(find(timeNEW≥0));  %[500:830]; %%Select a time -window
Npts=2^10;
IcentTF=[1:Npts]+Istart;
if max(IcentTF)>length(timeNEW);IcentTF=1:length(timeNEW);end
%IcentTF=[500:1000];
freq_int1=[Fmin,Fmax];
%%Make it even number-> remove last point;
```

```
if (mod(length(IcentTF),2)>0);IcentTF(end)=[];end;
TcentTF=timeNEW(IcentTF);
LENGTH1=length(TcentTF)/2;
Nc_TF=length(TcentTF);
freqC_TF=[0:Nc_TF-1]/Nc_TF/TsNEW;
   CC=DATA(IcentTF);%.*hanning(length(IcentTF));
%WV Analysis Function
g=tftb_window(odd(LENGTH1/50),'hamming');%Time smoothing window
h=tftb_window(odd(LENGTH1/1),'hamming');%Frequency smoothing window
[Wig,Tc1,F1] =tfrspwv(CC+sqrt(-1)*hilbert(CC),[1:length(TcentTF)],...
    LENGTH1,g,h);
Wig=((Wig.'));%%each column is a frequency
Fc1=[0:LENGTH1-1]/length(TcentTF)/TsNEW;
If1=find(Fc1≥freq_int1(1) & Fc1≤freq_int1(2) );
Fc2=Fc1;If2=If1;
MMamp(Iang)=max(max(abs(Wig)));
        %WIG_all(:,:,Iang)=Wig(:,If1);
  %Plot Time Response
%         figure(Iang);clf
%     plot(timeNEW,DATA);axis([1.5e-4 TcentTF(end) min(DATA) max(DATA)]);

%         Scale=50; %%in DB
if 1==1 %Plot WV
figure(3);clf;%hold on
                %subplot(2,2,2);
         axes('Position',[0.2908 0.5838 0.6757 0.3405]);
         pcolor(TcentTF,Fc1(If1),20*log10(abs(Wig(:,If1).')/MMamp(Iang)));
         xlabel('Time','FontSize',20);ylabel('Frequency','FontSize',20);
         shading interp
        caxis([00 60]+10*log10(MMamp(Iang)));
        colorbar([0.1535 0.105 0.0357 0.3425])
%        xlim(0.1/2*[-1 1])
```

```
        ylim(freq_int1)
        hold off
        axis tight
title(['Smooth-Pseudo Wigner Ville : ',num2str(sweep_theta(Iang)),'deg'])
       % track(Iang,:)=ginput(1);
%Temporal Response
        %subplot(2,2,4);
        axes('Position',[0.2919 0.11 0.6746 0.3399]);
        plot(timeNEW,DATA);
        axis([TcentTF(1) TcentTF(end) min(DATA)/2 max(DATA)/2]);
%Frequency Response
        %subplot(2,2,1);
        axes('Position',[0.1047 0.584 0.09198 0.338]);
        plot(abs(fft(CC)),freqC_TF);
        set(gca,'XDir','reverse');
        xlim([0 max(abs(fft(CC)))]);ylim(freq_int1);
        ANI(Iang)=getframe(gcf);
% %Save Plots
%  direct = cd;
%  cd ..;cd iterations;
%  saveas(figure(3),[num2str(sweep_theta(Iang)),'deg_sphr','.fig'])
%  cd(direct)
end
end
end
% %% Plot Combination of all Angles
% for idx=1:length(WIG_all(1,1,:))
%     WIG_all(:,:,idx)=WIG_all(:,:,idx)/max(max(WIG_all(:,:,idx)));
% end
% wig_sum=sum(WIG_all(:,:,[30:180]),3);
% figure
% wig_log=20*log10((wig_sum.')/max(max(wig_sum)));
```

```
% pcolor(TcentTF,Fc1(If1),real(wig_log));
% shading interp
% caxis([-70 0]);colorbar
% ylim(freq_int1)
% axis tight
%% Plot Angle vs Time (Sinogram)
% figure
% pcolor(sweep_theta',time(Irec),20*log10(abs(Pall./max(max(Pall)))));
% shading interp
% caxis([-70 0])

%% Animation
% figure
% axes('Position',[0 0 1 1])
% movie(ANI,2,8)%playback 2 times at 8 frames/sec
%movie2avi(ANI,'test3.avi','fps',20,'compression', 'Cinepak')
```

D.2 Acoustic Imaging

```
% load SAS2.mat
 load('C:\Users\user\Desktop\air_atten_360.mat')
 AA=tic;
X=8.9:.01:10.9;
Y=0:.01:.75;
ang=[90:270];
n=find(time≥10/c0,1,'first');
% s(n:n+length(Pall(:,1))-1,:)=Pall(:,ang);
 s(:,:)=Pall(:,ang);
% time=time(1:idx1);
time=0:time(2):length(s)*time(2)-time(2);
% for kk=1:length(ang)
%    [tmp,idxx]=max(abs(hilbert(s(1:1.144e4,kk))));
```

```
%        s([1:idxx+750],kk)=0;%remove specular
%    s([1:idxx-100,idxx+100:end],kk)=0;%remove guided waves
% end
    %   s(time≤1.85e-3,:)=0;%remove specular
% s=Pall(:,ang);
% for ii=1:size(s,2)
%     [tmp,id]=max(abs(s(:,ii)));
%     s(:,ii)=0;
%     s(id-20:id+20,ii)=hanning(41);%remove guided waves
% %     s(:,ii)=s(:,ii)+flipud(s(:,ii));
% end

theta=sweep_theta(ang);%
t0=10/c0;%Time for plane wave to get to sphere center
G=abs(s)';
xg=max(max(G)); ng=min(min(G)); cg=255/(xg-ng);
if 1==0
figure;%colormap(gray(256))
imagesc(time,theta,20*log10((abs(G./xg))));
%axis('square');axis('xy')
xlabel('Fast-time t, sec')
ylabel('Synthetic Aperture (Slow-time) U, meters')
title('Measured Spotlight SAR Signal')
%%%Setup Image Grid.
end

y=sweep_dist.*sind(180-sweep_theta);
x=10-sweep_dist.*cosd(180-sweep_theta);
N=length(s);
SAS_im=zeros(length(X),length(Y));
SAS_time=SAS_im;
```

```
beam=zeros(N,length(ang));
SAS_data=zeros(length(1:6500),length(X),length(Y));
tmp_dt=zeros(length(ang),length(X));
tmp_circ=zeros(N,1);
% time=time+5e-3+.53/c0;
tt=60;
for ii=1:length(X)
    BB=tic;
    clc; ii
    TimeLeft_min=(length(X)-ii)*tt/60
    for jj=1:length(Y)
        tmp_t=0;%((X(ii)^2+Y(jj)^2)^0.5)./c0;
        tmp_dt(:,ii)=(((X(ii)-x(ang)).^2+(Y(jj)-y(ang)).^2).^0.5...
            -(10-((X(ii)).^2+(Y(jj)).^2).^0.5))./c0;
        if tmp_t≥0
            [tmp,idx]=find(time≥tmp_t,1);
        else
            [tmp,idx]=find(time≥abs(tmp_t),1);
            idx=length(time)-idx;
        end
        idxx(ii)=idx;
        for kk=1:length(ang)
            if tmp_dt(kk,ii)≤0
                [tmp,idx]=find(time≥abs(tmp_dt(kk,ii)),1);
                idx=-idx;
            else
                [tmp,idx]=find(time≥tmp_dt(kk,ii),1);
            end
            if idx<0;idx=N+idx;end
            tmp_circ(1:N-idx)=s(idx+1:N,kk);
            tmp_circ((N+1-idx):N)=s(1:idx,kk);
             beam(:,kk)=tmp_circ./ 4.2706e-004;%normalize for air filled
```

```
%               beam(:,kk)=tmp_circ./2.0357e-004;%normalize for oil filled
%                check(:,ii,kk)=(beam(1:5:end,kk)./max(beam(:,kk))+kk);
        end
        tmp2=abs(hilbert(sum(beam,2)));
%         figure
%         for ii=1:180
%             plot(beam(:,ii)./max(beam(:,ii))+ii)
%             hold on
%         end
%         plot(sum(beam,2),'r')
%         plot(abs(hilbert(sum(beam,2))),'g')
%           try;
                tmp=decimate(sum(beam,2),2);
                SAS_data(:,ii,jj)=tmp(1:6500);
                [SAS_im(ii,jj),iii(ii,jj)]...
                    =max(tmp2(idxx(ii):idxx(ii)+20,:));%focus at pixel
% %
%         catch;[SAS_im(ii,jj),iii(ii,jj)]=max(tmp2(idxx:idxx,:));
%          end
     [SAS_im(ii,jj),iii(ii,jj)]=max(tmp2);


    end
    tt=toc(BB);
end
toc(AA)
  save backup
Y=[-fliplr(Y),Y(2:end)];
SAS_im=[fliplr(SAS_im),SAS_im(:,2:end)];
figure
% plot(x(ang),y(ang),'.')
% hold on
axes('YDir','normal','FontSize',20);hold on
```

```
imagesc(X.',Y,20*log10(abs(SAS_im.')./15));
axis image
colorbar
plot(10+0.53*cosd([0:360]),0.53*sind([0:360]),'w')
caxis([-30 0])
xlabel('Down Range (m)','FontSize',20)
ylabel('Cross Range (m)','FontSize',20)
max(max(abs(SAS_im)))
```

D.3 Noise Reduction

D.3.1 Single Frequency

```
%%% Create nn element array
%%% Record 1 TF-Atom
%clear all;close all;
tic
cntr=0;
for jjj=20;%:-10:0;%0:10:130;
    clc
    cntr=cntr+1
    dpcnt=0;
    for dplr=4
        dpcnt=dpcnt+1;
        for itr=1
            %% Inputs
            %% Create target position
            c0=343;%m/s sound speed
            X=8;%m
            Y=-1;%m
            Vs=(dplr-1)*200;%Source Velocity (m/s)doppler shift +YDirection
            fc=500; %center frequency of pulse
            tau=0.01;%%Set bandwidth via envelop decay
```

```
            o=0.5;%Noise Std Dev %Noise Level
            d=(c0/fc)/2;%(m) sensor spacing ¬1/2 wavelength @0.5kHz

            Fe=5e3;%%Sampling frequency
            Fmin=100;
            Fmax=1000;
            N=512;%Number of samples
            rr=17;%number of realizations/snapshots (to increase rank)
            nn=8; %Number of elements
            y=[-nn/2+.5:(nn)/2-0.5]*d;%receiver postion
            x=zeros(1,nn);%receiver postion
            ang=90+180./pi.*atan2((Y-y),(X-x));

            %%Create Gaussian Windowed Sine-Pulse
            Ts=1/Fe;
            time=[0:N-1]*Ts;
            freq=[0:N-1]/N/Ts;
            Tshift=(time(round(end/3))); %Center the pulse in window
            %%Gaussian-Windowed sine pulse 1
          for ii=1:nn
%                 fshift(dpcnt,ii)=jjj*(ii-1);
          fshift(dpcnt,ii)=fc-(1-Vs*cosd(ang(ii))./c0)*fc;%Doppler Shift Calc
           Sig(ii,:)=(sin(2*pi*(fc+fshift(dpcnt,ii))*(time-Tshift)).*...
               exp(-((time-Tshift)/tau).^2))';
         end
      % %%Gaussian-Windowed sine pulse 2
      % fc=fc+200;
      % Tshift=Tshift+.02;
      % Sig=Sig+(sin(2*pi*fc*(time-Tshift)).*exp(-((time-Tshift)/tau).^2))';

%             S=Sig(1,:)./max(max(abs(Sig)));
%             FSig=fft(Sig(1,:),[],2);
```

```
%             figure(10);clf;hold on
%             subplot(2,1,1)
%             plot(time*1000,S);
%             subplot(2,1,2)
%             plot(freq(1:end/2),abs((FSig(1:end/2))))

            %%Plot pulses
            Sig=Sig./max(max(abs(Sig)));
            FSig=fft(Sig,[],2);
            % figure(10);clf;hold on
            % subplot(2,1,1)
            % plot(time,Sig);
            % subplot(2,1,2)
            % plot(freq(1:end/2),abs((FSig(1:end/2))))

            t=time;%0:1/50e3:.001;

            % s=chirp(t,f0,t(end),f1);
            % s=xcorr(s);
            % % s=s+chirp(t,f0+3000,t(end),f1+3000,'q');
            % s=[zeros(1,150),s,zeros(1,(2^10-length(s)-150))]; %pad chirp
            % ss=length(s);
            % t=0:1/50e3:2^10/50e3-1/50e3; %set time axis (sec)
            % S_f=fft(s);
            % freq=0:fs/length(s):fs-fs/ss;
            %spectrogram(y,256,200,256,50e3); % Display the spectrogram.
            S=Sig;
            S_f=FSig;
            k=2*pi*freq./c0;
            ss=length(S(1,:));
            for ii=1:nn
                temp=(S_f(ii,:).*exp(-sqrt(-1).*k.*((x(ii)-X).^2+...
```

```
        (y(ii)-Y).^2).^0.5));
    %temp=(S_f(ii,:).*exp(-sqrt(-1).*k.*(0.5*ii-1)));
    S(ii,:)=real(ifft(temp));
    S(ii,:)=S(ii,:)./max(abs(S(ii,:)));
end
%% Add noise
for jj=1:rr+1
    %             for ii=1:nn
    tmp=o*randn(nn,ss);
    %             if dplr==1 && itr==1 && jj==rr+1
    %                 save add_noise.mat tmp
    %             end
    if jj==rr+1
        load noise_50.mat;
    end
     S_n(:,:,jj)=S+tmp;%add noise
    %             end
end


%% Denoise process
S_n_f=fft(S_n,[],2);%% FT
S_dn_a=sum(S_n,3)./(rr+1);
S_n=S_n(:,:,rr+1);
%         if itr==1
%             save S_n_persistant.mat S_n
%         end
%         load('S_n_persistant.mat')
S_n_f1=fft(S_n,[],2);
n=1; %number of coeff to keep
for ii=1:ss
    DD=0;
```

```
    for jj=1:rr
        DD=DD+(S_n_f(:,ii,jj)*S_n_f(:,ii,jj)');
    end
    [U,s,V]=svds(DD./jj,8);
    sv(:,ii)=diag(s);
    %     si=inv(s);
    %     si(1:end-n,1:end-n)=0;
    %     DDn=U*s*V.';
    S_dn_f(:,ii)=U(:,1)*(U(:,1)'*S_n_f1(:,ii));
end


S_dn=real(ifft(S_dn_f,[],2));
S_dn=S_dn./max(max(S_dn));
%% Plot Sinogram and Signal
if 0
    for ii=1:nn
        tmp(ii,:)=abs(hilbert(S_n(ii,:,1)));
    end
    figure
    subplot(2,2,1)
    imagesc(t,y,20*log10(tmp));
    xlabel('Time (s)')
    ylabel('Sensor Position (m)')
    caxis([-20 0])
    title('Noisey')
    for ii=1:nn
        tmp(ii,:)=abs(hilbert(S_dn(ii,:)));
    end
    subplot(2,2,2)
    imagesc(t,y,20*log10(abs(hilbert(tmp))));
    xlabel('Time (s)')
```

```
                ylabel('Sensor Position (m)')
                caxis([-20 0])
                title('Denoised')
                subplot(2,1,2)
                plot(t,S_n(1,:)./max(abs(S_n(1,:))),':b',t,S_dn(1,:).'./...
                    max(abs(S_dn(1,:))),'r')
                title('Time Series Sensor 1')
                xlabel('Time (sec)')
                legend('Noisy Signal','Denoised Signal')
            end

            %% Time Frequency
            if 1
    for sr=1:nn;%sensor number
        CC=S(sr,:).';%orginal
        CC_n=S_n(sr,:).';%noisey signal
        CC_dn=S_dn(sr,:).';%denoised signal
        CC_dn_a=S_dn_a(sr,:).';%Average realizations
        IcentTF=[1:length(time)];
        freq_int1=[Fmin,Fmax];
        if (mod(length(IcentTF),2)>0);IcentTF(end)=[];end;
        TcentTF=time(IcentTF);
        LENGTH1=length(TcentTF)/2;
        Nc_TF=length(TcentTF);
        freqC_TF=[0:Nc_TF-1]/Nc_TF/Ts;
        Fc1=[0:LENGTH1-1]/length(TcentTF)/Ts;
        If1=find(Fc1≥freq_int1(1) & Fc1≤freq_int1(2) );
        %WV Analysis Function
        g=tftb_window(odd(21),'hanning');%Time smoothing window
        h=tftb_window(odd(251),'hanning');%Frequency smoothing window
[Wig,Tc1,F1] =tfrspwv(CC+sqrt(-1)*2*hilbert(CC),...
    [1:length(TcentTF)],LENGTH1,g,h);
```

```
[Wig_n,Tc1,F1] =tfrspwv(CC_n+sqrt(-1)*2*hilbert(CC_n)...
    ,[1:length(TcentTF)],LENGTH1,g,h);
[Wig_dn,Tc1,F1] =tfrspwv(CC_dn+sqrt(-1)*2*hilbert(CC_dn)...
    ,[1:length(TcentTF)],LENGTH1,g,h);
[Wig_dn_a,Tc1,F1] =tfrspwv(CC_dn_a+sqrt(-1)*2*hilbert(CC_dn_a)...
    ,[1:length(TcentTF)],LENGTH1,g,h);

                    tmp_n(:,sr,:)=abs(Wig_n(If1,:).');
                    tmp_dn(:,sr,:)=abs(Wig_dn(If1,:).');
                    tmp_dn_a(:,sr,:)=abs(Wig_dn_a(If1,:).');
%                     Fc1=[0:(N/2)-1]/(N/2)/Ts;
%                     If1=find(Fc1≥Fe/2,1);
%                     Fc1=Fc1(1:If1)/2;


                data=20*log10(abs(Wig(If1,:))/max(max(abs(Wig))));
                data_n=20*log10(abs(Wig_n(If1,:))/max(max(abs(Wig_n))));
                data_dn=20*log10(abs(Wig_dn(If1,:))/max(max(abs(Wig_dn))));


                    %% Plotting
    if 0
        figure(5)
        % cm=colormap(hot);
        % cm1=flipud(cm);
        kk=1;
        % subplot(1,3,1)
        % pcolor(time(1:2:end),Fc1(If1(1:2:end)),data(1:2:end,1:2:end));
        % axis square
        % % colormap(cm1);
        % shading interp
        % caxis([-35 0]);%colorbar
```

```
        % % xlim([0.0256 .1792])
        % xlabel('Time (Seconds)'); ylabel('Hz');
        % title('Original Signal');

        subplot(1,2,1)
        pcolor(time(1:2:end),Fc1(If1(1:2:end)),data_n(1:2:end,1:2:end));
        % colormap(cm1);
        axis square
        shading interp
        caxis([-50 0]);%colorbar
        % xlim([0.0256 .1792])
        xlabel('Time (Seconds)'); ylabel('Hz');
        title('Noisy Signal');
        subplot(1,2,2)
        pcolor(time(1:2:end),Fc1(If1(1:2:end)),data_dn(1:2:end,1:2:end));
        % colormap(cm1);
        axis square
        shading interp
        caxis([-35 0]);%colorbar
        % xlim([0.0256 .1792])
        xlabel('Time (Seconds)'); ylabel('Hz');
        title('De-Noised Signal');
                    end
[tmp,yy]=max(max(abs(Wig)));
[tmp,xx]=max(max(abs(Wig.')));
% SNR_TF_n=10*log10(max(max(Wig_n))./...
%     mean(std(Wig_n(yy(1)-50:yy(1)+50,xx(1)-50:xx(1)+50))))
SNR_TF(itr,sr)=10*log10(mean(mean(abs(Wig_n(xx-2:xx+2,...
    yy-30:yy+30)))./mean(mean(abs(Wig_n(:,1:yy-100)))));
SNR_TF_dn(itr,sr)=10*log10(mean(mean(abs(Wig_dn(xx-2:xx+2,...
    yy-30:yy+30)))./mean(mean(abs(Wig_dn(:,yy-100)))));
SNR_TF_dn_a(itr,sr)=10*log10(mean(mean(abs(Wig_dn_a(xx-2:xx+2,...
```

```
    yy-30:yy+30)))))./mean(mean(abs(Wig_dn_a(:,yy-100)))));
                end


                %% Plot Array Setup
                if 0
                    figure
                    plot(x,y,'x');hold on
                    plot(X,Y,'.r');
                    xlim([-2,X+2]);
                    ylim([min(y)-1,max(y)+1])
                    xlabel('Down Range (m)');
                    ylabel('Cross Range (m)');
                    text(x(end)-1.5,y(end),'Array')
                    text(X+.2,Y+.5,'Source')
                end
            end
%             doppler1(dplr)=mean(mean(SNR_TF_dn))
            SNR_dif(dplr)=mean(mean((SNR_TF_dn-SNR_TF)))
            SNR_dif_a(dplr)=mean(mean((SNR_TF_dn_a-SNR_TF)))
        end
    end
end
    toc


    if 1==0
    axes('Position',[0.2908 0.5838 0.6757 0.3405]);
        pcolor(time.*1000,Fc1(If1),data);hold on
        cm=colormap(hot);
        cm1=flipud(cm);
        colormap(cm1);
        shading interp
```

```
%         caxis([00 55]+10*log10(MMamp(Iang)));
        caxis([-30 0])
        colorbar([0.1535 0.105 0.0357 0.3425])
        xlabel('Time (ms)','FontSize',12);
        ylabel('Frequency (kHz)','FontSize',12);
% title(['Smooth-Pseudo Wigner Ville : ',num2str(sweep_theta(Iang)),'deg'])
%Temporal Response
        %subplot(2,2,4);
        axes('Position',[0.2919 0.11 0.6746 0.3399]);
        plot(time*1000,S(1,:)./max(S(1,:)));
        xlim([TcentTF(1) TcentTF(end)]*10^3)
%         axis([TcentTF(1) TcentTF(end) min(DATA)/2 max(DATA)/2]);
%Frequency Response
        %subplot(2,2,1);
        axes('Position',[0.115 0.584 0.09198 0.338]);
        plot(abs(S_f(1,If1)),freq(If1));
        set(gca,'XDir','reverse');
        ylim([Fc1(1) Fc1(end)])
    end
```

D.3.2 Cross Frequency

```
%%% Create nn element array
%%% Record 1 TF-Atom
%clear all;close all;
cnt=0;
cntr=0;
for jjj=20;%:-10:0;%0:10:130;
    clc
    cntr=cntr+1
    dpcnt=0;
for dplr=4
```

```
 dpcnt=dpcnt+1;
for itr=1
    %% Inputs
    %% Create target position
    c0=343;%m/s sound speed
    X=8;%m
    Y=-1;%m
    Vs=(dplr-1)*200;%Source Velocity (m/s) doppler shift +Y Direction
    fc=500; %center frequency of pulse
    tau=0.01;%%Set bandwidth via envelop decay
    o=0.5;%Noise Std Dev %Noise Level
    d=(c0/fc)/2;%(m) sensor spacing ¬1/2 wavelength @0.5kHz

    Fe=5e3;%%Sampling frequency
    Fmin=100;
    Fmax=2000;
    N=512;%Number of samples
    rr=17;%number of realizations (to increase rank)
    nn=8; %Number of elements
    y=[-nn/2+.5:(nn)/2-0.5]*d;%receiver postion
    x=zeros(1,nn);%receiver postion
    ang=90+180./pi.*atan2((Y-y),(X-x));

    %%Create Gaussian Windowed Sine-Pulse
    Ts=1/Fe;
    time=[0:N-1]*Ts;
    freq=[0:N-1]/N/Ts;
    Tshift=(time(round(end/3))); %Center the pulse in the analysis window
    %%Gaussian-Windowed sine pulse 1
    for ii=1:nn
%           fshift(dpcnt,ii)=jjj*(ii-1);
        fshift(dpcnt,ii)=fc-(1-Vs*cosd(ang(ii))./c0)*fc;%Doppler Calc
```

```
        Sig(ii,:)=(sin(2*pi*(fc+fshift(dpcnt,ii))*(time-Tshift)).*...
            exp(-((time-Tshift)/tau).^2))';
    end
% %%Gaussian-Windowed sine pulse 2
% fc=fc+200;
% Tshift=Tshift+.02;
% Sig=Sig+(sin(2*pi*fc*(time-Tshift)).*exp(-((time-Tshift)/tau).^2))';

    %%Plot pulses
    Sig=Sig./max(max(abs(Sig)));
    FSig=fft(Sig,[],2);
    % figure(10);clf;hold on
    % subplot(2,1,1)
    % plot(time,Sig);
    % subplot(2,1,2)
    % plot(freq(1:end/2),abs((FSig(1:end/2))))

    t=time;%0:1/50e3:.001;

    % s=chirp(t,f0,t(end),f1);
    % s=xcorr(s);
    % % s=s+chirp(t,f0+3000,t(end),f1+3000,'q');
    % s=[zeros(1,150),s,zeros(1,(2^10-length(s)-150))]; %pad chirp
    % ss=length(s);
    % t=0:1/50e3:2^10/50e3-1/50e3; %set time axis (sec)
    % S_f=fft(s);
    % freq=0:fs/length(s):fs-fs/ss;
    %spectrogram(y,256,200,256,50e3); % Display the spectrogram.
    S=Sig;
    S_f=FSig;
    k=2*pi*freq./c0;
    ss=length(S(1,:));
```

```
    for ii=1:nn
     temp=(S_f(ii,:).*exp(-sqrt(-1).*k.*((x(ii)-X).^2+(y(ii)-Y).^2).^0.5));
%           temp=(S_f(ii,:).*exp(-sqrt(-1).*k.*(0.5*ii-1)));
            S(ii,:)=real(ifft(temp));
            S(ii,:)=S(ii,:)./max(abs(S(ii,:)));
        end
        %% Add noise
        for jj=1:rr+1
            %             for ii=1:nn
            tmp=o*randn(nn,ss);
%             if dplr==1 && itr==1 && jj==rr+1
%                 save add_noise.mat tmp
%             end
            if jj==rr+1
                load noise_50.mat;
            end
            S_n(:,:,jj)=S+tmp;%add noise
            %             end
        end


        %% Denoise process
        S_n_f=fft(S_n,[],2);%% FT

%         S_n_f(:,257:end,:)=[];
        n=1; %number of coeff to keep
        temp=[];
        DD=0;
        for jj=1:rr
%             temp=S_n_f(:,:,rr),nn*(128),jj)
            temp=reshape(S_n_f(:,:,jj),nn*(N),1);
%             temp=reshape(S_n_f(:,:,rr),nn*(ss),1);
```

```
        DD=DD+temp*temp';
    end

    S_n=S_n(:,:,rr+1);
    S_n_f=fft(S_n,[],2);
    clear temp
    [U,s,V]=svd(DD./jj);
    temp2=0;
%     for ii=1:ss/2
%        for jj=1:1 %%%Number of Singular Values to use
%         temp2=temp2+(U([1:nn]+nn*(ii-1),jj)*U([1:nn]+nn*(ii-1),jj)');
%        end
       temp=reshape(S_n_f,ss*nn,1);
       temp=U(:,1)*U(:,1)'*temp;
       S_dn_f=reshape(temp,nn,ss);
       clear temp
%     end

    S_dn=real(ifft(S_dn_f,N,2));
    S_dn=S_dn./max(max(S_dn));
    if 0
    for ii=1:nn
        tmp(ii,:)=abs(hilbert(S_n(ii,:,1)));
    end
    figure
    subplot(2,2,1)
    imagesc(t,y,20*log10(tmp));
    xlabel('Time (s)')
    ylabel('Sensor Position (m)')
    caxis([-20 0])
    title('Noisey')
    for ii=1:nn
```

```
    tmp(ii,:)=abs(hilbert(S_dn(ii,:)));
end
subplot(2,2,2)
imagesc(t,y,20*log10(abs(hilbert(tmp))));
xlabel('Time (s)')
ylabel('Sensor Position (m)')
caxis([-20 0])
title('Denoised')
subplot(2,1,2)
plot(t,S_n(1,:)./max(abs(S_n(1,:))),':b',t,S_dn(1,:).'./...
    max(abs(S_dn(1,:))),'r')
title('Time Series Sensor 1')
xlabel('Time (sec)')
legend('Noisy Signal','Denoised Signal')
end


%         %% Time Frequency
    if 1
        for sr=1;%:nn;%sensor number
            CC=S(sr,:).';%orginal
            CC_n=S_n(sr,:).';%noisey signal
            CC_dn=S_dn(sr,:).';%denoised signal
            IcentTF=[1:length(time)];
            freq_int1=[Fmin,Fmax];
            if (mod(length(IcentTF),2)>0);IcentTF(end)=[];end;
            TcentTF=time(IcentTF);
            LENGTH1=length(TcentTF)/2;
            Nc_TF=length(TcentTF);
            freqC_TF=[0:Nc_TF-1]/Nc_TF/Ts;
            Fc1=[0:LENGTH1-1]/length(TcentTF)/Ts;
            If1=find(Fc1≥freq_int1(1) & Fc1≤freq_int1(2) );
```

```
  %WV Analysis Function
g=tftb_window(odd(21),'hanning');%Time smoothing window
h=tftb_window(odd(251),'hanning');%Frequency smoothing window
[Wig,Tc1,F1] =tfrspwv(CC+sqrt(-1)*2*hilbert(CC),[1:length(TcentTF)],...
    LENGTH1,g,h);
[Wig_n,Tc1,F1] =tfrspwv(CC_n+sqrt(-1)*2*hilbert(CC_n),...
    [1:length(TcentTF)],LENGTH1,g,h);
[Wig_dn,Tc1,F1] =tfrspwv(CC_dn+sqrt(-1)*2*hilbert(CC_dn),...
    [1:length(TcentTF)],LENGTH1,g,h);
                    tmp_n(:,sr,:)=abs(Wig_n(If1,:).');
                    tmp_dn(:,sr,:)=abs(Wig_dn(If1,:).');
%                     Fc1=[0:(N/2)-1]/(N/2)/Ts;
%                     If1=find(Fc1≥Fe/2,1);
%                     Fc1=Fc1(1:If1)/2;


                data=20*log10(abs(Wig(If1,:))/max(max(abs(Wig))));
                data_n=20*log10(abs(Wig_n(If1,:))/max(max(abs(Wig_n))));
                data_dn=20*log10(abs(Wig_dn(If1,:))/max(max(abs(Wig_dn))));


                    %% Plotting
                    if 0
                        figure(5)
                        % cm=colormap(hot);
                        % cm1=flipud(cm);
                        kk=1;
            % subplot(1,3,1)
            % pcolor(time(1:2:end),Fc1(If1(1:2:end)),data(1:2:end,1:2:end));
            % axis square
            % % colormap(cm1);
            % shading interp
```

```
            % caxis([-35 0]);%colorbar
            % % xlim([0.0256 .1792])
            % xlabel('Time (Seconds)'); ylabel('Hz');
            % title('Original Signal');

          subplot(1,2,1)
           pcolor(time(1:2:end),Fc1(If1(1:2:end)),data_n(1:2:end,1:2:end));
                        % colormap(cm1);
                        axis square
                        shading interp
                        caxis([-35 0]);%colorbar
                        % xlim([0.0256 .1792])
                        xlabel('Time (Seconds)'); ylabel('Hz');
                        title('Noisy Signal');
                        subplot(1,2,2)
          pcolor(time(1:2:end),Fc1(If1(1:2:end)),data_dn(1:2:end,1:2:end));
                        % colormap(cm1);
                        axis square
                        shading interp
                        caxis([-50 0]);%colorbar
                        % xlim([0.0256 .1792])
                        xlabel('Time (Seconds)'); ylabel('Hz');
                        title('De-Noised Signal');
                    end
                    [tmp,yy]=max(max(abs(Wig)));
                    [tmp,xx]=max(max(abs(Wig.')));
  % SNR_TF_n=10*log10(max(max(Wig_n))./...
   %     mean(std(Wig_n(yy(1)-50:yy(1)+50,xx(1)-50:xx(1)+50))))
 SNR_TF(itr,sr)=10*log10(mean(mean(abs(Wig_n(xx-2:xx+2,yy-30:yy+30)))./...
                        mean(mean(abs(Wig_n(:,1:yy-100)))));
SNR_TF_dn(itr,sr)=10*log10(mean(mean(abs(Wig_dn(xx-2:xx+2,yy-30:yy+30)))./...
                        mean(mean(abs(Wig_dn(:,yy-100)))));
```

```
                end


                %% Plot Array Setup
                if 0
                    figure
                    plot(x,y,'x');hold on
                    plot(X,Y,'.r');
                    xlim([-2,X+2]);
                    ylim([min(y)-1,max(y)+1])
                    xlabel('Down Range (m)');
                    ylabel('Cross Range (m)');
                    text(x(end)-1.5,y(end),'Array')
                    text(X+.2,Y+.5,'Source')
                end
            end
%             doppler1(dplr)=mean(mean(SNR_TF_dn))
            SNR_dif(dplr)=mean(mean((SNR_TF_dn-SNR_TF)))
        end
    end
end
    toc
```

D.3.3 STFD-SVD

```
%%Compute Cross Wigner Ville between Gaussian Windowed Sine pulses

%%% Create nn element array
%%% Record 1 TF-Atom
%clear all;close all;
cntr=0;
for jjj=20;%:-10:0;%0:10:130;
```

```
clc
cntr=cntr+1;
dpcnt=0;
for dplr=1:11
    AA=tic;
    dpcnt=dpcnt+1;
    %% Inputs
    %% Create target position
    c0=343;%m/s sound speed
    X=8;%m
    Y=-1;%m
    Vs=(dplr-1)*200;%Source Velocity (m/s) for doppler +Y Direction
    fc=500; %center frequency of pulse
    tau=0.01;%%Set bandwidth via envelop decay
    o=0.95;%Noise Std Dev %Noise Level
    d=(c0/fc)/2;%(m) sensor spacing ¬1/2 wavelength @0.5kHz

    Fe=5e3;%%Sampling frequency
    Fmin=100;
    Fmax=2000;
    N=512;%Number of samples
    rr=17;%number of realizations (to increase rank)
    nn=8; %Number of elements
    y=[-nn/2+.5:(nn)/2-0.5]*d;%receiver postion
    x=zeros(1,nn);%receiver postion
    ang=90+180./pi.*atan2((Y-y),(X-x));
    Y=min(y);
    %%Create Gaussian Windowed Sine-Pulse
    Ts=1/Fe;
    time=[0:N-1]*Ts;
    freq=[0:N-1]/N/Ts;
    Tshift=(time(round(end/3))); %Center the pulse in the analysis window
```

```
        %%Gaussian-Windowed sine pulse 1
for ii=1:nn
%fshift(dpcnt,ii)=jjj*(ii-1);%fc-(1-Vs*cosd(ang(ii))./c0)*fc;%Doppler Shift Calc1
fshift(dpcnt,ii)=fc-(1-Vs*cosd(ang(ii))./c0)*fc;%Doppler Shift Calc1
Sig(ii,:)=(sin(2*pi*(fc+fshift(dpcnt,ii))*(time-Tshift)).*...
    exp(-((time-Tshift)/tau).^2))';
end


        %%Plot pulses
        Sig=Sig./max(max(abs(Sig)));
        FSig=fft(Sig,[],2);



        t=time;%0:1/50e3:.001;
        S=Sig;
        S_f=FSig;
        k=2*pi*freq./c0;
        ss=length(S(1,:));
for ii=1:nn
    temp=(S_f(ii,:).*exp(-sqrt(-1).*k.*(((x(ii)-X).^2+...
        (y(ii)-Y).^2).^0.5)));
    %            temp=(S_f(ii,:).*exp(-sqrt(-1).*k.*(0.5*ii-1)));
    S(ii,:)=real(ifft(temp));
    S(ii,:)=S(ii,:)./max(abs(S(ii,:)));
end


        %% Add noise
        for jj=1:rr+1
            %             for ii=1:nn
            tmp=o*randn(nn,ss);
            %             if dplr==1 && itr==1 && jj==rr+1
            %                 save add_noise.mat tmp
```

```
    %             end
    if jj==rr+1
        load noise_95.mat;
    end
    S_n(:,:,jj)=S+tmp;%add noise
    %             end
end

%%%%%%%%%%%%Cross Wigner Ville. Time Freq Analysis
INIT=0;
count1=0;
WigALL_partial_sum=0;
Rcat_sum=0;
for nnn=1:rr+1
    for zz=1:nn;
        count1=count1+1;

        DATA=S_n(zz,:,nnn) ;
        IcentTF=[1:length(time)]; %[-Npts/2+1:Npts/2]+Istart;
        freq_int1=[Fmin,Fmax];
        TcentTF=time(IcentTF);
        LENGTH1=length(TcentTF)/2;
        Nc_TF=length(TcentTF);
        freqC_TF=[0:Nc_TF-1]/Nc_TF/Ts;
        CCref=DATA(IcentTF).';%.*hanning(length(IcentTF));
        CCref1=CCref+sqrt(-1)*2*hilbert(CCref);


        count2=0;

        for zz2=1:zz %length(ThetS);
            count2=count2+1;
```

```
                    DATA=S_n(zz2,:,nnn) ;
                    CC=DATA(IcentTF).';%.*hanning(length(IcentTF));
                    CC1=CC+sqrt(-1)*2*hilbert(CC);

                    if INIT==0;
                        INIT=1;
                        Fc1=[0:LENGTH1-1]/length(TcentTF)/Ts;
                        If1=find(Fc1≥freq_int1(1) & Fc1≤freq_int1(2) );
                        Twig=time; %TcentTF+time(Irec(1));%%
                        WigALL=zeros(length(Fc1(If1)),length(Twig),nn,nn);
                        Nf=size(WigALL,1);
                        Nt=size(WigALL,2);
                    end

%WV Analysis Function
g=tftb_window(21,'hanning');%Time smoothing window
h=tftb_window(251,'hanning');%Frequency smoothing window in the time domain
[Wig,Tc1,F1] =tfrspwv([CC1,CCref1],[1:length(TcentTF)],LENGTH1,g,h);
WigALL(:,:,count1,count2)=Wig(If1,:);


                end;
            end



%%%Complete cross-conjugate manually to speed-things up
for zz=1:nn;
    for zz2=zz+1:nn;
        WigALL(:,:,zz,zz2)=conj(WigALL(:,:,zz2,zz));
    end
end
```

```
count1=0;

display('FINISHED Computing Wigner Ville !!!')


INDff=find(Fc1(If1)≥Fmin & Fc1(If1)≤Fmax); %Select frequency window
INDtt=find(Twig>0 & Twig<0.145); %%Select time window
NgapTT=1; %%Smoothing of wigner ville also limit this resolution..
NgapFF=1;
INDff=INDff(1:NgapFF:end);
INDtt=INDtt(1:NgapTT:end);

            %%%Compute Reference Wigner Ville Matrix- for No noise input....
            Rcat=zeros(nn*length(INDff),length(INDtt)*nn);
             Npos=nn;

            %%Compute SVD

            %  %%%Broadband SVD....
%             Rcat=zeros(Npos*length(INDff),length(INDtt)*Npos);

            for zz1=1:Npos
                for zz2=1:Npos
                    Rcat( 1+(zz1-1)*length(INDff):zz1*length(INDff),1+...
                        (zz2-1)*length(INDtt):zz2*length(INDtt) )...
                        =WigALL(INDff,INDtt,zz1,zz2);
                end
            end

             Rcat_sum=Rcat_sum+Rcat;
        end
```

```
          Rcat=Rcat_sum;
%          WigALL_partial2=WigALL_partial_sum./(rr+1);
%          clear WigALL_partial_sum


             [Ub,Sb,Vb]=svds(Rcat,100);%Compute SVD


             pp=1;
             cnte=1;
             while pp==1
                 energy=sum(diag(Sb(1:cnte,1:cnte)))/sum(diag(Sb));
                 if energy ≥0.1
                     pp=0;
                 else
                     cnte=cnte+1;
                 end
             end
cnte=1;

%%%PLOT THE Denoised Wigner Ville after SVD processing and compare to noise


             count=0;
             clear ax
             % for ss=cnte; %Nsvd;
             ss=cnte;
             count=count+1;
             Sbtemp=zeros(size(Sb));
             for qq=1:ss
                 Sbtemp(qq,qq)=Sb(qq,qq);
             end
             Rcat=Ub*Sbtemp*Vb'; %%Reconstruct XWV Matrix
```

```
            WigALL_partial=zeros(length(INDff),length(INDtt),Npos,Npos);
            for zz1=1:Npos
                for zz2=1:Npos
                    WigALL_partial(:,:,zz1,zz2)=Rcat( 1+(zz1-1)*...
                        length(INDff):zz1*length(INDff),1+(zz2-1)*...
                        length(INDtt):zz2*length(INDtt) );
                end
            end
%             WigALL_partial_sum=WigALL_partial_sum+WigALL_partial;
%         end
%         WigALL_partial2=WigALL_partial_sum./(rr+1);
%         clear WigALL_partial_sum

        for jj=1:Npos;
[Wig,Tc1,F1] =tfrspwv(S(jj,:).'+sqrt(-1)*2*hilbert(S(jj,:).'),...
    [1:length(TcentTF)],LENGTH1,g,h);
Cref=abs(real(Wig));
C1=abs(real(WigALL(INDff,INDtt,jj,jj)));
C2=abs(real(WigALL_partial(:,:,jj,jj)));
%             C3=abs(real(WigALL_partial2(:,:,jj,jj)));

    [tmp,yy]=max(max(abs(Cref)));
    [tmp,xx]=max(max(abs(Cref.')));
    SNR_TF(jj)=10*log10(mean(mean(abs(C1(xx-2:xx+2,yy-30:yy+30)))./...
        mean(mean(abs(C1(:,1:yy-100))))));
    SNR_TF_dn(jj)=10*log10(mean(mean(abs(C2(xx-2:xx+2,yy-30:yy+30)))./...
        mean(mean(abs(C2(:,1:yy-100))))));
%  SNR_TF_dn_a(jj)=10*log10(mean(mean(abs(C3(xx-2:xx+2,yy-30:yy+30)))./...
%       mean(mean(abs(C3(:,1:yy-100))))));
        end

    SNR_dif(dpcnt)=(mean(SNR_TF_dn-SNR_TF));
```

```
    SNR_diff(dpcnt)=(max(SNR_TF_dn-SNR_TF));
%     SNR_dif_a(dpcnt)=(mean(SNR_TF_dn_a-SNR_TF));
%     SNR_diff_a(dpcnt)=(max(SNR_TF_dn_a-SNR_TF));
    t_est=toc(AA);
    clc
    display(['Est. Time Left = ', num2str(t_est/60*(11-dpcnt)),' min'])
    end
end
% end
%^^^^^^^^^^^^^^^^^^^^^^^^^^^^^^^^^^^^^^^^^^^^^^^^^^^^^^^^^^^^^^^^^^^^^^^^^^^^
```

REFERENCES

[1] Abeysekera, S., Naidu, P., Leung, Y.-H., and Lew, H., "An underwater target classification scheme based on the acoustic backscatter form function," in *Acoustics, Speech and Signal Processing, 1998. Proceedings of the 1998 IEEE International Conference on*, vol. 4, pp. 2513 –2516 vol.4, may 1998.

[2] Achenbach, J., *Wave Propagation in Elastic Solids*. Elsevier Science Publishers B.V., 1975.

[3] Altes, R. A. and Titlebaum, E. L., "Bat signals as optimally doppler tolerant waveforms," *The Journal of the Acoustical Society of America*, vol. 48, no. 4B, pp. 1014–1020, 1970.

[4] Altes, R. A., "Sonar for generalized target description and its similarity to animal echolocation systems," *The Journal of the Acoustical Society of America*, vol. 59, no. 1, pp. 97–105, 1976.

[5] Anderson, S. D., Sabra, K. G., Zakharia, M. E., and Sessarego, J.-P., "Time-frequency analysis of the bistatic acoustic scattering from a spherical elastic shell," *The Journal of the Acoustical Society of America*, vol. 131, no. 1, pp. 164–173, 2012.

[6] Baggeroer, A. and Cox, H., "Passive sonar limits upon nulling multiple moving ships with large aperture arrays," in *Signals, Systems, and Computers, 1999. Conference Record of the Thirty-Third Asilomar Conference on*, vol. 1, pp. 103 –108 vol.1, oct. 1999.

[7] Baik, K., Dudley, C., and Marston, P. L., "Acoustic quasi-holographic images of scattering by vertical cylinders from one-dimensional bistatic scans," *The Journal of the Acoustical Society of America*, vol. 130, no. 6, pp. 3838–3851, 2011.

[8] Belcher, E., Lynn, D., Dinh, H., and Laughlin, T., "Beamforming and imaging with acoustic lenses in small, high-frequency sonars," in *OCEANS '99 MTS/IEEE. Riding the Crest into the 21st Century*, vol. 3, pp. 1495 –1499 vol.3, 1999.

[9] Belouchrani, A. and Amin, M., "Blind source separation based on time-frequency signal representations," *Signal Processing, IEEE Transactions on*, vol. 46, pp. 2888 –2897, nov 1998.

[10] Belouchrani, A. and Amin, M., "Time-frequency music," *Signal Processing Letters, IEEE*, vol. 6, pp. 109 –110, may 1999.

[11] Blondel, P. and Caiti, A., *Buried Waste in the Seabed: Acoustic Imaging and Bio-toxicity*. Springer, 2007.

[12] Boudreaux-Bartels, G. and Parks, T., "Time-varying filtering and signal estimation using wigner distribution synthesis techniques," *Acoustics, Speech and Signal Processing, IEEE Transactions on*, vol. 34, pp. 442 – 451, jun 1986.

[13] Burdic, W. S., *Underwater acoustic system analysis*. Prentice Hall, 1984.

[14] Chevret, P., Gache, N., and Zimpfer, V., "Time-frequency filters for target classification," *The Journal of the Acoustical Society of America*, vol. 106, no. 4, pp. 1829–1837, 1999.

[15] Clem, T., "Sensor technologies for hunting buried sea mines," in *OCEANS '02 MTS/IEEE*, vol. 1, pp. 452 – 460 vol.1, oct. 2002.

[16] Cohen, L., *Time Frequency Analysis: Theory and Applications*. New Jersey: Prentice Hall PTR, 1995.

[17] Debever, C. and Kuperman, W. A., "Robust matched-field processing using a coherent broadband white noise constraint processor," *The Journal of the Acoustical Society of America*, vol. 122, no. 4, pp. 1979–1986, 2007.

[18] Doolittle, R. D., Überall, H., and Uginčius, P., "Sound scattering by elastic cylinders," *The Journal of the Acoustical Society of America*, vol. 43, no. 1, pp. 1–14, 1968.

[19] Dragonette, L. R., "Evaluation of the relative importance of circumferential or creeping waves in the acoustic scattering from rigid and elastic solid cylinders and from cylindrical shells," *Interim Report*, 1978.

[20] Espana, A., Williams, K., Kargl, S., Zampolli, M., Marston, T., and Marston, P., "Measurements and modeling of the acoustic scattering from an aluminum pipe in the free field and in contact with a sand sediment," in *OCEANS 2010*, pp. 1 –5, sept. 2010.

[21] Feldman, D. and Griffiths, L., "A projection approach for robust adaptive beamforming," *Signal Processing, IEEE Transactions on*, vol. 42, pp. 867 –876, apr 1994.

[22] Felsen, L. B., Ho, J. M., and Lu, I. T., "Three-dimensional green's function for fluid-loaded thin elastic cylindrical shell: Alternative representations and ray acoustic forms," *The Journal of the Acoustical Society of America*, vol. 87, no. 2, pp. 554–569, 1990.

[23] Flandrin, P., Magand, F., and Zakharia, M., "Generalized target description and wavelet decomposition," *IEEE Trans. on Acoust., Speech and Signal Proc.*, vol. ASSP-38, no. 2, pp. 350–352, 1990.

[24] Flandrin, P., Sageloli, J., Sessarego, J., and Zakharia, M., "Application of time-frequency analysis to the characterization of surface waves on elastic targets," *Acoustics Letters*, vol. 10, no. 2, pp. 23–28, 1986.

[25] Flax, L., Dragonette, L. R., and Überall, H., "Theory of elastic resonance excitation by sound scattering," *The Journal of the Acoustical Society of America*, vol. 63, no. 3, pp. 723–731, 1978.

[26] Follett, J. R. L., Williams, K. L., and Marston, P. L., "Boundary effects on backscattering by a solid aluminum cylinder: Experiment and finite element model comparisons (l)," *The Journal of the Acoustical Society of America*, vol. 130, no. 2, pp. 669–672, 2011.

[27] Friedman, A., Mitchell, S., Kooij, T., and Scarbrough, K., "Circular synthetic aperture sonar design," in *Oceans 2005 - Europe*, vol. 2, pp. 1038 – 1045 Vol. 2, june 2005.

[28] Gasperini, W., "Uncle sam's dolphins," *Smithsonian magazine*, September 2003.

[29] Gaunaurd, G. C. and Werby, M. F., "Sound scattering by resonantly excited, fluid-loaded, elastic spherical shells," *The Journal of the Acoustical Society of America*, vol. 90, no. 5, pp. 2536–2550, 1991.

[30] Gerbrands, J. J., "On the relationships between svd, klt and pca," *Pattern Recognition*, vol. 14, no. 16, pp. 375 – 381, 1981.

[31] Goodman, R. R. and Stern, R., "Reflection and transmission of sound by elastic spherical shells," *The Journal of the Acoustical Society of America*, vol. 34, no. 3, pp. 338–344, 1962.

[32] Gough, P. T. and Hawkins, D. W., "Unified framework for modern synthetic aperture imaging algorithms," *International Journal of Imaging Systems and Technology*, vol. 8, pp. 343–358, 1997.

[33] Hamilton, E. L. and Bachman, R. T., "Sound velocity and related properties of marine sediments," *The Journal of the Acoustical Society of America*, vol. 72, no. 6, pp. 1891–1904, 1982.

[34] Hansen, R., Callow, H., Sabo, T., and Synnes, S., "Challenges in seafloor imaging and mapping with synthetic aperture sonar," *Geoscience and Remote Sensing, IEEE Transactions on*, vol. 49, pp. 3677 –3687, oct. 2011.

[35] Hassanpour, H., "Improved svd-based technique for enhancing the time-frequency representation of signals," in *Circuits and Systems, 2007. ISCAS 2007. IEEE International Symposium on*, pp. 1819 –1822, may 2007.

[36] Hayes, M. P. and Gough, P. T., "Broad-band synthetic aperture sonar," *IEEE Journal of Oceanic Engineering*, vol. 17, no. 1, pp. 80–94, 1992.

[37] Hinich, M. J., "Frequency-wavenumber array processing," *The Journal of the Acoustical Society of America*, vol. 69, no. 3, pp. 732–737, 1981.

[38] Ho, J.-M., "Near-field ray acoustic response of submerged elastic spherical shells," *The Journal of the Acoustical Society of America*, vol. 96, no. 1, pp. 525–535, 1994.

[39] Hoya, T., Tanaka, T., Cichocki, A., Murakami, T., Hori, G., and Chambers, J., "Stereophonic noise reduction using a combined sliding subspace projection and adaptive signal enhancement," *Speech and Audio Processing, IEEE Transactions on*, vol. 13, pp. 309 – 320, may 2005.

[40] Huang, H. and Gaunaurd, G. C., "Acoustic scattering of a plane wave by two spherical elastic shells above the coincidence frequency," *The Journal of the Acoustical Society of America*, vol. 101, no. 5, pp. 2659–2668, 1997.

[41] Jensen, F., Kuperman, W., Porter, M., and Schmidt, H., *Computational Ocean Acoustics*. AIP Press, 1994.

[42] Johnson, D. H. and Dudgeon, D. E., *Array signal processing: Concepts and Techniques, Signal processing series*. Prentice Hall, 1993.

[43] Jonsson, M., Pihl, J., and Aklint, M., "Imaging of buried objects by low frequency sas," in *Oceans 2005 - Europe*, vol. 1, pp. 669 – 673 Vol. 1, june 2005.

[44] J.R., S. and R.C., M., "Increased autonomy and cooperation in multi-auv naval mine countermeasures," in *Undersea Defense Technology*, 2004.

[45] Junger, M. C., "Radiation loading of cylindrical and spherical surfaces," *The Journal of the Acoustical Society of America*, vol. 24, no. 3, pp. 288–289, 1952.

[46] Kaduchak, G. and Marston, P. L., "Backscattering of chirped bursts by a thin spherical shell near the coincidence frequency," *The Journal of the Acoustical Society of America*, vol. 93, no. 5, pp. 2700–2706, 1993.

[47] Kalnins, A., "Analysis of shells of revolution subjected to symmetrical and nonsymmetrical loads," *Journal of Applied Mechanics*, vol. 31, no. 3, pp. 467–476, 1964.

[48] Kargl, S. G. and Marston, P. L., "Observations and modeling of the backscattering of short tone bursts from a spherical shell: Lamb wave echoes, glory, and axial reverberations," *The Journal of the Acoustical Society of America*, vol. 85, no. 3, pp. 1014–1028, 1989.

[49] Kinsler, L., Frey, A., Coppens, A., and Sanders, J., *Fundamentals of Acoustics*. Wiley, 2000.

[50] LePage, K. and Schmidt, H., "Bistatic synthetic aperture imaging of proud and buried targets from an auv," *Oceanic Engineering, IEEE Journal of*, vol. 27, pp. 471 – 483, jul 2002.

[51] Li, W., Liu, G. R., and Varadan, V. K., "Estimation of radius and thickness of a thin spherical shell in water using the midfrequency enhancement of a short tone burst response," *The Journal of the Acoustical Society of America*, vol. 118, no. 4, pp. 2147–2153, 2005.

[52] Lucifredi, I. and Schmidt, H., "Subcritical scattering from buried elastic shells," *The Journal of the Acoustical Society of America*, vol. 120, no. 6, pp. 3566–3583, 2006.

[53] Magand, F. and Chevret, P., "Time frequency analysis of energy distribution for circumferential waves on cylindrical elastic shells," *Acta Acustica united with Acustica*, vol. 82, pp. 707–716, October 1996.

[54] Maguer, A., Fox, W. L. J., Schmidt, H., Pouliquen, E., and Bovio, E., "Mechanisms for subcritical penetration into a sandy bottom: Experimental and modeling results," *The Journal of the Acoustical Society of America*, vol. 107, no. 3, pp. 1215–1225, 2000.

[55] Marston, P. L. and Sun, N. H., "Resonance and interference scattering near the coincidence frequency of a thin spherical shell: An approximate ray synthesis," *The Journal of the Acoustical Society of America*, vol. 92, no. 6, pp. 3315–3319, 1992.

[56] Marston, P. L. and Sun, N. H., "Backscattering near the coincidence frequency of a thin cylindrical shell: Surface wave properties from elasticity theory and an approximate ray synthesis," *The Journal of the Acoustical Society of America*, vol. 97, no. 2, pp. 777–783, 1995.

[57] Marston, P. L., "Approximate meridional leaky ray amplitudes for tilted cylinders: End-backscattering enhancements and comparisons with exact theory for infinite solid cylinders," *The Journal of the Acoustical Society of America*, vol. 102, no. 1, pp. 358–369, 1997.

[58] Marston, T., Marston, P., and Williams, K., "Scattering resonances, filtering with reversible sas processing, and applications of quantitative ray theory," in *OCEANS 2010*, pp. 1 –9, sept. 2010.

[59] Michalopoulou, Z.-H. and Porter, M., "Matched-field processing for broad-band source localization," *Oceanic Engineering, IEEE Journal of*, vol. 21, pp. 384 – 392, oct 1996.

[60] Mitchell, S. and Pitt, S., "Sas imaging of proud and buried targets at search frequencies," in *OCEANS '02 MTS/IEEE*, vol. 4, pp. 2279 – 2283 vol.4, 29-31 2002.

[61] Mitchell, S. and Pitt, S., "Bistatic sas imaging studies," in *Proceedings of the Institute of Acoustics, London*, vol. 4, 9 2006.

[62] Morse, S. F. and Marston, P. L., "Backscattering of transients by tilted truncated cylindrical shells: Time-frequency identification of ray contributions from measurements," *The Journal of the Acoustical Society of America*, vol. 111, no. 3, pp. 1289–1294, 2002.

[63] Mu, W., Amin, M., and Zhang, Y., "Bilinear signal synthesis in array processing," *Signal Processing, IEEE Transactions on*, vol. 51, pp. 90 – 100, jan. 2003.

[64] Nelatury, S. and Mobasseri, B., "Synthesis of discrete-time discrete-frequency wigner distribution," *Signal Processing Letters, IEEE*, vol. 10, pp. 221 –224, aug. 2003.

[65] Neubauer, W. G., "Acoustic reflection from surfaces and shapes," *Interim Report*, 1986.

[66] Nielsen, R. O., *Sonar signal processing*. Artech House, 1991.

[67] Piper, J. E., Commander, K. W., Thorsos, E. I., and Williams, K. L., "Detection of buried targets using synthetic aperture sonar," *IEEE Journal of Oceanic Engineering*, vol. 27, no. 3, pp. 495–503, 2002.

[68] Prada, C. and Fink, M., "Separation of interfering acoustic scattered signals using the invariants of the time-reversal operator. application to lamb waves characterization," *The Journal of the Acoustical Society of America*, vol. 104, no. 2, pp. 801–807, 1998.

[69] Reed, I., Mallett, J., and Brennan, L., "Rapid convergence rate in adaptive arrays," *Aerospace and Electronic Systems, IEEE Transactions on*, vol. AES-10, pp. 853 –863, nov. 1974.

[70] Rickard, J., "Signal decorrelation effects due to differential doppler," in *Circuits, Systems and Computers, 1985. Nineteeth Asilomar Conference on*, pp. 570 – 575, nov 1985.

[71] Rios, J. J., "Naval mines in the 21st century: Can nato navies meet the challenge?," Master's thesis, NAVAL POSTGRADUATE SCHOOL, June 2005.

[72] Rossing, T. D., *Springer Handbook of Acoustics*. Springer, 2007.

[73] Sammelmann, G. S., Trivett, D. H., and Hackman, R. H., "The acoustic scattering by a submerged, spherical shell. i: The bifurcation of the dispersion curve for the spherical antisymmetric lamb wave," *The Journal of the Acoustical Society of America*, vol. 85, no. 1, pp. 114–124, 1989.

[74] Santamarina, J. and Fratta, D., *Discrete Signals and Inverse Problems: An Introduction for Engineers and Scientists*. John Wiley and Sons, 2005.

[75] Schmidt, H., Lee, J., Fan, H., and LePage, K., "Multistatic bottom reverberation in shallow water," in *High Frequency Acoustics in Shallow Water, SACLANTCEN Conference Proceedings Series*, vol. CP-45, (La Spezia, Italy), pp. 475–481, 1997.

[76] Schmidt, H. and Lee, J., "Physics of 3-d scattering from rippled seabeds and buried targets in shallow water," *The Journal of the Acoustical Society of America*, vol. 105, pp. 1605–1617, 1999.

[77] Shlens, J., "A tutorial on principle component analysis," *Online: University of California, San Diego*, 2005.

[78] Son, J., Thomas, G., and B.C., F., *Range-Doppler Radar Imaging and Motion Compensation*. Boston: Artech House, 2001.

[79] Song, H., Kuperman, W., Hodgkiss, W., Gerstoft, P., and Kim, J. S., "Null broadening with snapshot-deficient covariance matrices in passive sonar," *Oceanic Engineering, IEEE Journal of*, vol. 28, pp. 250 – 261, april 2003.

[80] Sternlicht, D., Lernonds, D., Dikeman, R., Ericksen, M., and Schock, S., "Detection and classification of buried objects with an adaptive acoustic mine-hunting system," in *OCEANS, 2001. MTS/IEEE Conference and Exhibition*, vol. 1, pp. 212 –219 vol.1, 2001.

[81] Strang, G., "The fundamental theorem of linear algebra," *The American Mathematical Monthly*, vol. 100, no. 9, pp. pp. 848–855, 1993.

[82] Sun, N. H. and Marston, P. L., "Ray synthesis of leaky lamb wave contributions to backscattering from thick cylindrical shells," *The Journal of the Acoustical Society of America*, vol. 91, no. 3, pp. 1398–1402, 1992.

[83] Sutton, J., "Underwater acoustic imaging," *Proceedings of the IEEE*, vol. 67, pp. 554 – 566, april 1979.

[84] Sutton, T., Griffiths, A., Hetet, Y., and Chapman, S., "Experimental validation of autofocus algorithms for high-resolution imaging of the seabed using synthetic aperture sonar," in *IEE Proceedings of Radar Sonar Navigation*, vol. 150, pp. 78–83, 2003.

[85] Talmant, M., Uberall, H., Miller, R. D., Werby, M. F., and Dickey, J. W., "Lamb waves and fluid-borne waves on water-loaded, air-filled thin spherical shells," *The Journal of the Acoustical Society of America*, vol. 86, no. 1, pp. 278–289, 1989.

[86] Tesei, A., Fox, W. L. J., Maguer, A., and Lovik, A., "Target parameter estimation using resonance scattering analysis applied to air-filled, cylindrical shells in water," *The Journal of the Acoustical Society of America*, vol. 108, no. 6, pp. 2891–2900, 2000.

[87] Tesei, A., Maguer, A., Fox, W. L. J., Lim, R., and Schmidt, H., "Measurements and modeling of acoustic scattering from partially and completely buried spherical shells," *The Journal of the Acoustical Society of America*, vol. 112, no. 5, pp. 1817–1830, 2002.

[88] Tesei, A., Guerrini, P., and Zampolli, M., "Tank measurements of scattering from a resin-filled fiberglass spherical shell with internal flaws," *The Journal of the Acoustical Society of America*, vol. 124, no. 2, pp. 827–840, 2008.

[89] Trees, H. L. V., *Detection, Estimation, and Modulation Theory: Optimum Array Processing*. USA: Wiley-Interscience, 2002.

[90] Uberall, H., Gaunaurd, G., and Murphy, J. D., "Acoustic surface wave pulses and the ringing of resonances," *The Journal of the Acoustical Society of America*, vol. 72, no. 3, pp. 1014–1017, 1982.

[91] Veksler, N., Izbicki, J., and Conoir, J., "Isolation of surface wave resonances in scattering by an elastic shell," in *Ultrasonics Symposium, 1994. Proceedings., 1994 IEEE*, vol. 2, pp. 723 –726 vol.2, 31 1994-nov. 3 1994.

[92] Ville, J., "Theorie et applications de la notion de signal analytique (theory and applications of the notion of complex signal)," *Technical Report*, vol. 2A, no. 1, pp. 61–74, 1948.

[93] Vorobyov, S. and Cichocki, A., "Blind noise reduction for multisensory signals using ica and subspace filtering, with application to eeg analysis," *Biological Cybernetics*, vol. 86, pp. 293–303, November 2002.

[94] Weiss, L., "Wavelets and wideband correlation processing," *Signal Processing Magazine, IEEE*, vol. 11, pp. 13 –32, jan 1994.

[95] Weiss, L. and Young, R., "Wideband spatial processing with wavelet transforms," in *Statistical Signal and Array Processing, 1992. Conference Proceedings., IEEE Sixth SP Workshop on*, pp. 235 –238, oct 1992.

[96] Wigner, E., "On the quantum correction for thermodynamic equilibrium," *Physical Review*, vol. 40, pp. 749–759, June 1932.

[97] Williams, K. L., Kargl, S. G., Thorsos, E. I., Burnett, D. S., Lopes, J. L., Zampolli, M., and Marston, P. L., "Acoustic scattering from a solid aluminum cylinder in contact with a sand sediment: Measurements, modeling, and interpretation," *The Journal of the Acoustical Society of America*, vol. 127, no. 6, pp. 3356–3371, 2010.

[98] Xia, X.-G. and Chen, V., "A quantitative snr analysis for the pseudo wigner-ville distribution," *Signal Processing, IEEE Transactions on*, vol. 47, pp. 2891 –2894, oct 1999.

[99] Xie, S., Yang, L., Yang, J.-M., Zhou, G., and Xiang, Y., "Time-frequency approach to underdetermined blind source separation," *Neural Networks and Learning Systems, IEEE Transactions on*, vol. 23, pp. 306 –316, feb. 2012.

[100] Zakharia, M., "Automatic target recognition, the devil is in the details," in *Acoustics 2010 Istanbul Conference*, 2010.

[101] Zakharia, M. and Sessarego, J., "Sonar target classification using a coherent echo processing," in *Acoustics, Speech, and Signal Processing, IEEE International Conference on ICASSP '82.*, vol. 7, pp. 331 – 334, may 1982.

[102] Zakharia, M. E., Flandrin, P., Sessarego, J., and Sagloli, J., "Analyse temps-fréquence appliquée à la caractérisation acoustique de cibles (time-frequency analysis applied to the characterization of an acoustic target)," *J. Acoustique*, vol. 1, pp. 185–188, 1988.

[103] Zakharia, M. E. and Chevret, P., "Neural network approach for inverting velocity dispersion; application to sediment and to sonar target characterization," *Inverse Problems*, vol. 16, no. 6, p. 1693, 2000.

[104] Zakharia, M., Magand, F., Sessarego, J.-P., and Sagloli, J., *Application of time-frequency analysis to the characterization of acoustical scattering (Chapter 7 of Acoustic interaction with submerged elastic structures).* New Jersey: Word Scientific Publications, 2001. 168-204.

[105] Zakharia, M. and Sessarego, J.-P., "Application of time-frequency analysis to non destructive evaluation (n.d.e.)," in *Proceedings of The IEEE Ultrasonics Symposium*, vol. 2, (Lake Buena Vista, Florida), pp. 809–818, 12 1991.

[106] Zhang, L. G., Sun, N. H., and Marston, P. L., "Midfrequency enhancement of the backscattering of tone bursts by thin spherical shells," *The Journal of the Acoustical Society of America*, vol. 91, no. 4, pp. 1862–1874, 1992.

[107] Zhang, P. and Geers, T. L., "Excitation of a fluid-filled, submerged spherical shell by a transient acoustic wave," *The Journal of the Acoustical Society of America*, vol. 93, no. 2, pp. 696–705, 1993.

[108] Zhang, Y. and Amin, M., "Array processing for nonstationary interference suppression in ds/ss communications using subspace projection techniques," *Signal Processing, IEEE Transactions on*, vol. 49, pp. 3005 –3014, dec 2001.